

UC San Diego

UC San Diego Electronic Theses and Dissertations

Title

A New Synthesis Method for Complex Electric Field Patterning using a Multichannel Dense Array System with Applications in Low-Intensity Noninvasive Neuromodulation

Permalink

<https://escholarship.org/uc/item/7kb1783w>

Author

Smith, Matthew Charles

Publication Date

2022

Peer reviewed|Thesis/dissertation

UNIVERSITY OF CALIFORNIA SAN DIEGO

A New Synthesis Method for Complex Electric Field Patterning using a Multichannel Dense Array System with Applications in Low-Intensity Noninvasive Neuromodulation

A Dissertation submitted in partial satisfaction of the requirements
for the degree Doctor of Philosophy

in

Electrical Engineering (Applied Electromagnetics)

by

Matthew Charles Smith

Committee in charge:

Professor Daniel Sievenpiper, Chair
Professor Peter Asbeck
Professor Gert Cauwenberghs
Professor Eric Fullerton
Professor Imanuel Lerman
Professor Zhaowei Liu

2022

Copyright

Matthew Charles Smith, 2022

All rights reserved.

The Dissertation of Matthew Charles Smith is approved, and it is acceptable in quality and form for publication on microfilm and electronically.

University of California San Diego

2022

DEDICATION

To my beloved wife and best friend Tammy Smith.

EPIGRAPH

*Living is worthwhile if one can contribute
in some small way to this endless chain
of progress.*

Paul A. M. Dirac

TABLE OF CONTENTS

DISSERTATION APPROVAL PAGE	iii
DEDICATION	iv
EPIGRAPH.....	v
TABLE OF CONTENTS.....	vi
LIST OF FIGURES	viii
LIST OF TABLES	x
ACKNOWLEDGEMENTS	xi
VITA.....	xiv
ABSTRACT OF THE DISSERTATION	xv
CHAPTER 1 BIOMAGNETIC APPLICATIONS AND PRINCIPLES	1
1.1 INTRODUCTION.....	1
1.2 HISTORICAL PERSPECTIVES.....	7
1.3 PHYSICS AND BIOPHYSICS.....	9
1.4 SCOPE OF THESIS.....	13
CHAPTER 2 SYNTHESIS METHOD PRINCIPLES OF OPERATION	17
2.1 INTRODUCTION	17
2.2 PIXEL CELL	17
2.3 INDUCED CURRENTS VECTOR ANALYSIS	19
2.4 TEMPLATE ARRAY	24
2.5 HEXAGONAL LATTICE AND COORDINATE SYSTEM	28
2.6 MECHANICS OF MOVEMENT OF THE TEMPLATE ARRAY	33
CHAPTER 3 SIMULATIONS AND EXPERIMENTAL RESULTS	42
3.1 TRADITIONAL PATTERNS COMPARED TO THE PIXEL CELL	42
3.2 COMPLEX USER-DEFINED E-FIELD PATTERNS – SIMULATIONS	44
3.3 MEASUREMENTS VS. SIMULATIONS OF COMPLEX PATTERNS	49
3.4 SIMULATIONS BRAIN MODEL	51
CHAPTER 4 RECONFIGURABLE DEPTH OF PENETRATION	53
4.1 INTRODUCTION	53
4.2 PRINCIPLES OF OPERATION	54
4.3 EXPERIMENTAL RESULTS AND SIMULATIONS	57

CHAPTER 5 REDUCED EXTRANEEOUS EXCITATION..... 73

5.1 INTRODUCTION 73

5.2 PRINCIPLES OF OPERATION 76

CHAPTER 6 SYSTEM ARCHITECTURE 83

CHAPTER 7 METHODS FOR MEASUREMENT AND SIMULATIONS..... 88

7.1 E-FIELD MEASUREMENT METHODS 88

7.2 B-FIELD MEASUREMENT METHODS 91

7.3 FINITE ELEMENT MODELING METHODS AND METRICS 93

CHAPTER 8 IMPLEMENTATION CHALLENGES 97

8.1 INTRODUCTION 97

8.2 PROXIMITY EFFECTS | MUTUAL COUPLING 97

CHAPTER 9 SUMMARY AND CONCLUSION 101

BIBLIOGRAPHY 104

LIST OF FIGURES

Figure 1.1:	Magnetic induction applications.....	2
Figure 1.2:	Classical E-field pattern vs. new complex patterns.....	4
Figure:1.3:	Research objectives, technical approach, and accomplishments.....	5
Figure 1.4:	Graphical overview of our research contributions	5
Figure 1.5:	Physics of magnetic stimulation.....	9
Figure 1.6:	The decay of the magnetic field vs. coil diameter.....	11
Figure 1.7:	Temporal aspects of magnetic stimulation.....	13
Figure 2.1:	Definition of <i>pixel cell</i> and concept.....	18
Figure 2.2:	Pixel eddy-current vector analysis.....	22
Figure 2.3:	Movement of a <i>pixel cell</i> using intuition.....	23
Figure 2.4:	Simple pattern formation using intuition.....	24
Figure 2.5:	Definition of the <i>template array</i> and concept.....	25
Figure 2.6:	<i>Template array</i> illustrated concept.....	26
Figure 2.7:	Synthesis of a unilinear pattern using the <i>template array</i>	27
Figure 2.8:	Hexagonal lattice vs. square lattice.....	29
Figure 2.9:	Movement using a hexagonal lattice and cubic coordinates.....	31
Figure 2.10:	Example of cubic and axial coordinates in the hex lattice	32
Figure 2.11:	Counter-clockwise rotation of a <i>double-pixel cell</i>	34
Figure 2.12:	Example - generating coil weight matrices for rotation.....	36
Figure 2.13:	Example – translation of a <i>double-pixel</i>	37
Figure 2.14:	Example – generating a sharp bend.....	39
Figure 2.15:	Flow chart for pattern synthesis with Python.....	41
Figure 3.1:	Traditional patterns with the dense array.....	42
Figure 3.2:	Radial near field scan of pixel vs. traditional figure 8 coil.....	43
Figure 3.3:	Synthesis of a circular pattern.....	45
Figure 3.4:	Synthesis of a zig-zag pattern.....	46
Figure 3.5:	Summary of synthesized patterns.....	48
Figure 3.6:	Experimental results vs. simulations.....	50
Figure 3.7:	Pattern using realistic head model (planar array).....	51
Figure 3.8:	Pattern using realistic head model (conformal array).....	52
Figure 4.1:	Reconfigurable depth of penetration concept.....	53
Figure 4.2:	Comparison coil diameters decay (Biot-Savart).....	55
Figure 4.3:	Concentric phase cancellation of a low planar array.....	56
Figure 4.4:	Simulation - contour plots (x-z cut plane) comparison decay profiles.....	57
Figure 4.5:	Baseline measurements of B-field contour and surface plots.....	58
Figure 4.6:	Decay profiles of B-field in air vs. conductive media.....	59
Figure 4.7:	Contour plots of B-field measurements vs. simulations.....	60
Figure 4.8:	Measurement of depth of penetration (circular coils)	61

Figure 4.9:	Measurement of depth of penetration (hexagonal coils).....	62
Figure 4.10:	Depth of penetration - hexagonal coil vs. circular coil arrays.....	63
Figure 4.11:	Physical comparison (photograph) - hex vs. coils.....	64
Figure 4.12:	Simulation of coupled coil currents – hex vs. circular arrays.....	65
Figure 4.13:	Measurement of B-field - depth of penetration 3 coil-topology.....	66
Figure 4.14:	Measurement of B-field - depth of penetration 4 coil-topology.....	67
Figure 4.14:	Measurement of B-field - depth of penetration 6 coil-topology.....	68
Figure 5.1:	Method of eddy current diffusion for reduced extraneous excitation.....	75
Figure 5.2:	Tapering current weighting (zone 1,2,3,4) $\vec{E}_{max}/2$ suppression.....	76
Figure 5.3:	Zone 1,2,3,4 (43 coils) for reduced extraneous excitation.....	77
Figure 5.4:	Zones 1 - 4 definition and illustration.....	78
Figure 5.5:	Zone 5- zone 6 definition and illustration.....	79
Figure 5.6:	Tapering current weighting (zone 1,2,3,4,5) $\vec{E}_{max}/2$ suppression.....	80
Figure 5.7:	Lower and Upper limits zone size on reduced extraneous excitation.....	81
Figure 5.8:	Number of zones, tapering weights vs. reduced extraneous excitation.....	82
Figure 6.1:	Multichannel dense array system block diagram and photograph.....	84
Figure 6.2:	Dense array and coil fabrication fixture photographs.....	85
Figure 6.3:	Waveform measurements and schematic of subchannel.....	86
Figure 7.1:	E-field and eddy-current measurement in PVP solution with dipole probe...	89
Figure 7.2:	E-field measurement Thermal imager $\Delta^{\circ}T$	90
Figure 7.3:	B-field measurement methodology.....	91
Figure 7.4:	Near-field scanner measurement system for B-field imaging.....	94
Figure 7.5:	Metric for E-field penetration of $ E_{max}/E_{min} $	96
Figure 8.1:	Proposed method for proximity effect mitigation.....	99
Figure 8.2:	Photo of 12-coil array measured and switch schematic.....	99
Figure 9.1:	Summary of user-defined synthesized patterns.....	102

LIST OF TABLES

Table 4.1:	Decay coefficients for B-field.....	70
Table 5.1:	Tapered current weights for reduced extraneous excitation.....	77
Table 5.2:	Reduced extraneous excitation vs. number of zones.....	82
Table 6.1:	Multichannel dense array system specifications.....	85

ACKNOWLEDGEMENTS

This journey would not have been remotely possible without my wife Tammy whose infinite patience and support has kept me going day after day. Clearly, without her by my side I would have never finished.

I offer my most sincere thanks to my advisor, Professor Daniel Sievenpiper, for his mentorship and his remarkable ability to always find new paths in physics and engineering for his research team to explore. Also, many thanks to my committee members, Professor Peter Asbeck, Professor Gert Cauwenberghs, Professor Eric Fullerton, Professor Imanuel Lerman and Professor Zhaowei Liu. Their support, guidance and encouragement over the years were indispensable. Moreover, what is most striking to me is that they are not only gifted research scientists but some of the most talented teachers I have ever encountered in a classroom setting. I would also like to thank Professor Michael Heller, Professor Tina Ng, Professor Yu-hwa Lo, Professor Vitaly Lomakin and Professor Gabriel Rebeiz for their support, guidance, and encouragement.

I sincerely thank my talented colleagues in the applied electromagnetics group, for their inspiration over the years. After working 30+ years in the defense industry, I have found them to be some of the most capable scientists and engineers on the planet. It has been an honor to be a part of this very capable group.

Last of all but not least many thanks to Walt Borra, Sheryl Borra, and my sister Cindy and brother-in law Jim Paauw for their encouragement and support.

Chapter 2 of this dissertation is based on Matthew C. Smith and Daniel F. Sievenpiper, “A New Synthesis Method for Complex Electric Field Patterning using a Multichannel Dense Array System with Applications in Low-Intensity Noninvasive Neuromodulation”,

Bioelectromagnetics, vol. n, no. 2022, pp. (14 pages), *In editorial review*. The dissertation author was the primary investigator and author of this paper.

Chapter 3 of this dissertation is based on Matthew C. Smith and Daniel F. Sievenpiper, “A New Synthesis Method for Complex Electric Field Patterning using a Multichannel Dense Array System with Applications in Low-Intensity Noninvasive Neuromodulation”, *Bioelectromagnetics*, vol. n, no. 2022, pp. (14 pages), *In editorial review*. The dissertation author was the primary investigator and author of this paper.

Chapter 4, of this dissertation is based on Matthew C. Smith, Aobo Li and Daniel. F. Sievenpiper, "A Multifunction Dense Array System with Reconfigurable Depth of Penetration," *IEEE Journal of Electromagnetics, RF and Microwaves in Medicine and Biology*, vol. 5, no. 1, pp. 35-45, March 2021. The dissertation author was the primary researcher and author of this paper.

Chapter 5 of this dissertation is based on Matthew Smith and Daniel Sievenpiper, “A New Synthesis Method and Magnetic Instrument for Complex Electric Field Patterning with Enhanced Localization”, *IEEE Magnetic Letters*, vol. n, no. 2022, pp. (5 pages), *In preparation*. The dissertation author was the primary researcher and author of this material.

Chapter 6 of this dissertation is based on Matthew C. Smith, Aobo Li and Daniel. F. Sievenpiper, "A Multifunction Dense Array System with Reconfigurable Depth of Penetration," *IEEE Journal of Electromagnetics, RF and Microwaves in Medicine and Biology*, vol. 5, no. 1, pp. 35-45, March 2021. The dissertation author was the primary researcher and author of this paper.

Chapter 7 of this dissertation is based on two papers. Sections 7.1 and 7.3 are based on Matthew C. Smith and Daniel F. Sievenpiper, “A New Synthesis Method for Complex Electric

Field Patterning using a Multichannel Dense Array System with Applications in Low-Intensity Noninvasive Neuromodulation”, *Bioelectromagnetics*, vol. n, no. 2022, pp. (14 pages), *In editorial review*. The dissertation author was the primary investigator and author of this paper. Section 7.2 is based on Matthew C. Smith, Aobo Li and Daniel F. Sievenpiper, "A Multifunction Dense Array System with Reconfigurable Depth of Penetration," *IEEE Journal of Electromagnetics, RF and Microwaves in Medicine and Biology*, vol. 5, no. 1, pp. 35-45, March 2021. The dissertation author was the primary researcher and author of this paper.

Chapter 8 of this dissertation is based on Matthew C. Smith and Daniel F. Sievenpiper, “A New Synthesis Method for Complex Electric Field Patterning using a Multichannel Dense Array System with Applications in Low-Intensity Noninvasive Neuromodulation”, *Bioelectromagnetics*, vol. n, no. 2022, pp. (14 pages), *In editorial review*. The dissertation author was the primary investigator and author of this paper.

VITA

1984 Bachelor of Science in Electrical Engineering, University of South Florida

1984 Bachelor of Science in Natural Sciences, University of South Florida

2019 Master of Science in Electrical Engineering (Applied Electromagnetics), University of California San Diego

2022 Doctor of Philosophy in in Electrical Engineering (Applied Electromagnetics), University of California San Diego

PUBLICATIONS

Journals

M. C. Smith, A. Li and D. F. Sievenpiper, "A Multifunction Dense Array System with Reconfigurable Depth of Penetration," *IEEE Journal of Electromagnetics, RF and Microwaves in Medicine and Biology*, vol. 5, no. 1, pp. 35-45, March 2021.

M. C. Smith and D. F. Sievenpiper, "A New Synthesis Method for Complex Electric Field Patterning using a Multichannel Dense Array System with Applications in Low-Intensity Noninvasive Neuromodulation", *Bioelectromagnetics*, vol. n, no. n, 2022, pp. (14 pages), (in editorial review).

M. C. Smith and D. F. Sievenpiper, "The Synthesis of Complex Electric Field Patterns with Enhanced Localization of Fields", *IEEE Magnetic Letters*, vol. n, no. n, 2022, pp. (6 pages), (in preparation).

Conference/Workshop presentation

M. C. Smith and D. F. Sievenpiper, "A Dense Magnetic Coil Array with Curvilinear Multi-loci and Multi-site Patterning for Noninvasive Neuromodulation", *Brain, Body, Mind: Cognitive Neuroengineering for Health and Wellness: A Virtual Symposium and Workshop*, Dec. 15-16, 2021.

ABSTRACT OF THE DISSERTATION

A New Synthesis Method for Complex Electric Field Patterning using a Multichannel Dense Array System with Applications in Low-Intensity Noninvasive Neuromodulation

by

Matthew Charles Smith

Doctor of Philosophy in Electrical Engineering (Applied Electromagnetics)

University of California San Diego, 2022

Professor Daniel F. Sievenpiper, Chair

Multichannel coil array systems offer precise spatiotemporal electronic steering and patterning of electric and magnetic fields without the physical movement of coils or magnets. This capability could potentially benefit a wide range of biomagnetic applications such as low-intensity noninvasive neuromodulation or magnetic drug delivery. In this regard, the objective of this work is to develop a unique synthesis method, that enabled by a multichannel dense array system, generates complex current pattern distributions not previously reported in the literature. Simulations and experimental results verify that highly curved or irregular (e.g., zig

- zag) patterns at singular and multiple sites can be efficiently formed using this method. The synthesis method is composed of three primary components; a *pixel cell* (basic unit of pattern formation), a *template array* (“virtual array”: code that disseminates the coil current weights to the “physical” dense array), and a hexagonal coordinate system. Additionally, we demonstrate that the depth of penetration of the magnetic field can be controlled by varying coil current weights (magnitude and phase, 0 and π) of the smaller coil diameters in the array to achieve the same decay profile performance of a larger diameter coil. Only simulations exist in the literature to date, to the best of our knowledge. We also report the first measurements of hexagonal shaped coils in multi-coil arrays and that they offer increased depth of penetration over circular shaped coil-based arrays. Finally, a method for localizing or reducing extraneous excitation around a user-defined E-field pattern is proposed and simulated. Low Intensity or Low-Field Magnetic Stimulation is identified as a potential application that could benefit from this work in the future and as such is used as an example to frame the research.

CHAPTER 1 BIOMAGNETIC APPLICATIONS AND PRINCIPLES

1.1 INTRODUCTION

Today there is an extensive landscape of applications (Fig. 1.1) that use magnetic induction as the basis for their principle of operation. The advent of spatial and temporal electronic steering of electric and magnetic field patterns using subwavelength multi-coil arrays is gaining momentum as a potential tool for many of these applications. Specifically in this work several disciplines in biomagnetic applications are the focus. Multi-coil arrays have the potential in one system without physical movement of the coil, to electronically steer precise, rapid, induced electric field (E-field) patterns over single or multiple sites (sequentially or simultaneously). They can also efficiently generate magnetic field (B-field) gradients to facilitate the transport of magnetized particles for drug delivery without physical movement of coils or magnets.

A few examples of applications that could potentially benefit from multi-coil arrays and the synthesis of arbitrary E-field patterns include low-field magnetic stimulation (LFMS) [Zmeykina et al, 2020] or low-intensity Magnetic Stimulation (LIMS) [Grehl et al, 2016], high-field transcranial magnetic stimulation (TMS) [Barker et al,1985], magnetic induction tomography [Ma et al, 2017], and drug delivery systems [Hajiaghajani and Abdolali, 2018].

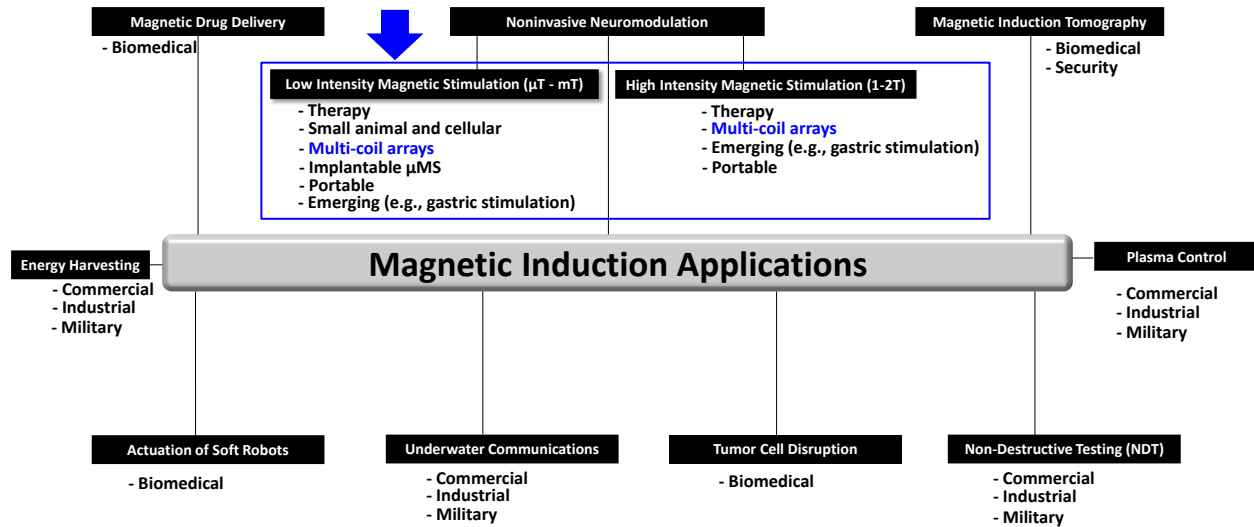


Figure 1.1: LIMS is selected as an initial candidate application to frame our research.

Historically, TMS or high-field TMS has been one of the most actively researched biomagnetic applications in which multi-coil arrays have been implemented. Today a single TMS figure-8 coil is used to enhance the focality [Ueno et al, 1988] of neuronal targets and when deeper penetration is required, a larger diameter coil assembly is used at the expense of focality [Zangen et al, 2015]. These are typically single channel systems with one coil assembly that are manually positioned over a target excitation site with aid of a gantry for stabilization.

Recently the concept of using multi-coil arrays to enhance the spatiotemporal stimulation capabilities of TMS, has influenced several promising approaches for high-field TMS. For example, one approach, demonstrated that the induced E-field pattern can be steered along one dimension in the cortex [Koponen et al, 2018]. Another approach electronically steered the location and orientation of an induced E-field in a 30mm diameter cortical region as enabled by a 5-coil transducer [Nieminen et al, 2022]. Also, a unique 3-axis coil design, reported by [Navarro de Lara et al, 2021], capable of integration in a conformal multi-element array, shows promising results as well.

High-field TMS (peak B-field:1-2T, induced E-fields $\geq 100\text{Vm}^{-1}$), and LIMS (peak B-fields: $\mu\text{T-mT}$ range, induced E-fields $\leq 1\text{Vm}^{-1}$) both use a time-varying B-field, created by a pulsed current, through a coil to induce an E-field in a neuronal site [Grehl et al, 2016]. In general, TMS is more focal and elicits suprathreshold neuronal activity whereas LIMS or LFMS is more diffuse and elicits subthreshold levels that still modify cortical function, brain oscillations and metabolism [Goetz and Deng, 2017]. Today TMS is the exemplar of noninvasive brain stimulation (NIBS) and is used widely in neuroscience research and the treatment of neurological disorders. LIMS, also referred to as LFMS, are emerging as a possible treatment for neurological disorders as well [Dubin et al, 2019; Zmeykina et al, 2020]. Notably LIMS is being used in neuroscience research at the cellular level [Dufor et al, 2019; Grehl et al, 2016], small animal studies [Tang et al, 2016; Tang et al, 2018], and in implantable arrays of coils [Ryu et al, 2020; Minusa et al, 2019].

The primary objective of this work is to propose, using our new synthesis method, what other types of patterns are “possible” and perhaps useful in future biomagnetic applications. We demonstrate with simulations and experimental results that the generation of sharply curved or irregular E-field patterns at singular and multiple sites is possible with this method. As an illustrative example, a traditional figure-8 coil unilinear pattern is simulated and compared to two patterns formed by our synthesis method and 3-layer array, in Figure 1.2. This method is enabled by a multichannel 3-layer array system previously reported by the authors [Smith et al, 2021].

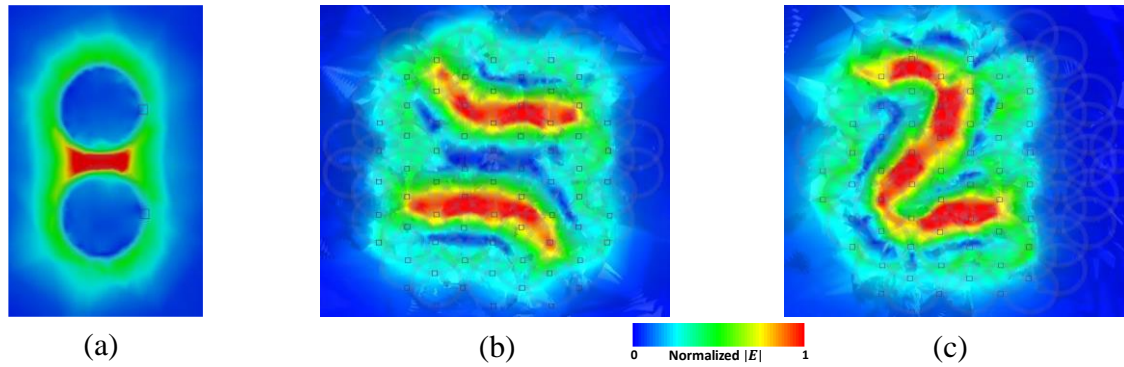


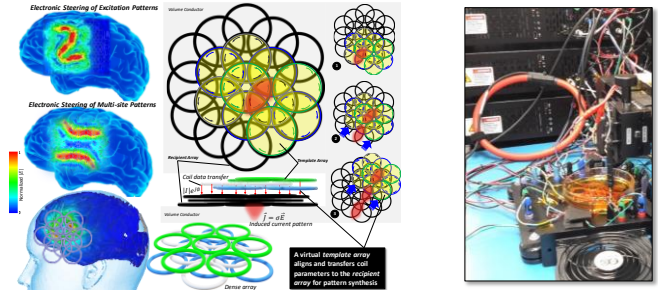
Figure 1.2: Simulation comparing a traditional figure-8 coil E-field pattern to two complex curved patterns generated by our synthesis approach and array. (a) figure-8 coil unilinear pattern, (b) new synthesis method and array: curved multi-site, (c) new synthesis method array: zig - zag.

This paper describes and validates a new synthesis method, via simulations and experimental results, in an ideal homogeneous conductive media [Ianniello et al, 2018] to establish the proof-of-concept. Several simulations are included to show how these patterns are distorted in a brain model [Ansys HFSSR21, finite element simulation software, and Human Body Model V3] with both a planar and conformal version of the 3-layer array. Regardless of the implementation, whether a traditional figure-8 or multi-coil array, the complexities of cortical regions distribute and distort the induced E-field pattern in a non-trivial way [Thielscher et al, 2011; Optiz et al, 2011].

Our new synthesis method and highly scalable electronics design can be used with a range of coil diameters, power levels and topologies including scaling down in size/current for implantable and cellular research applications. Contributions to the literature based on our research, our technical approach and accomplishments are shown in Fig 1.3 and along with a graphical abstract in Fig. 1.4 and summarized as follows.

Objectives

- Develop an efficient synthesis method for generating both complex multi-loci and multi-site E-field patterning
- Develop indices well suited for a three-layer dense array system that maintains all three coil current weights
- Design and fabricate a scalable multichannel dense array system applicable to many different applications
- Verify via simulations and experimental results



Technical Approach

- Pixel cell and Template Array Concepts
- Hexagonal Lattice and Cubic Coordinates
- Scalable Multichannel Electronics System
- Finite element models (FEM) and Measurements

Accomplishments

- A unique synthesis method for complex pattern synthesis
- Synthesized curved and irregular patterns
- Reconfigurable depth of penetration
- Multichannel (13-channel) prototype dense array system
- Reduced extraneous excitation

Multichannel array systems offer precise spatiotemporal electronic steering and patterning of electric and magnetic fields without the physical movement of coils or magnets.

Figure 1.3: Outline of research objectives, technical approach and contributions made to the literature.

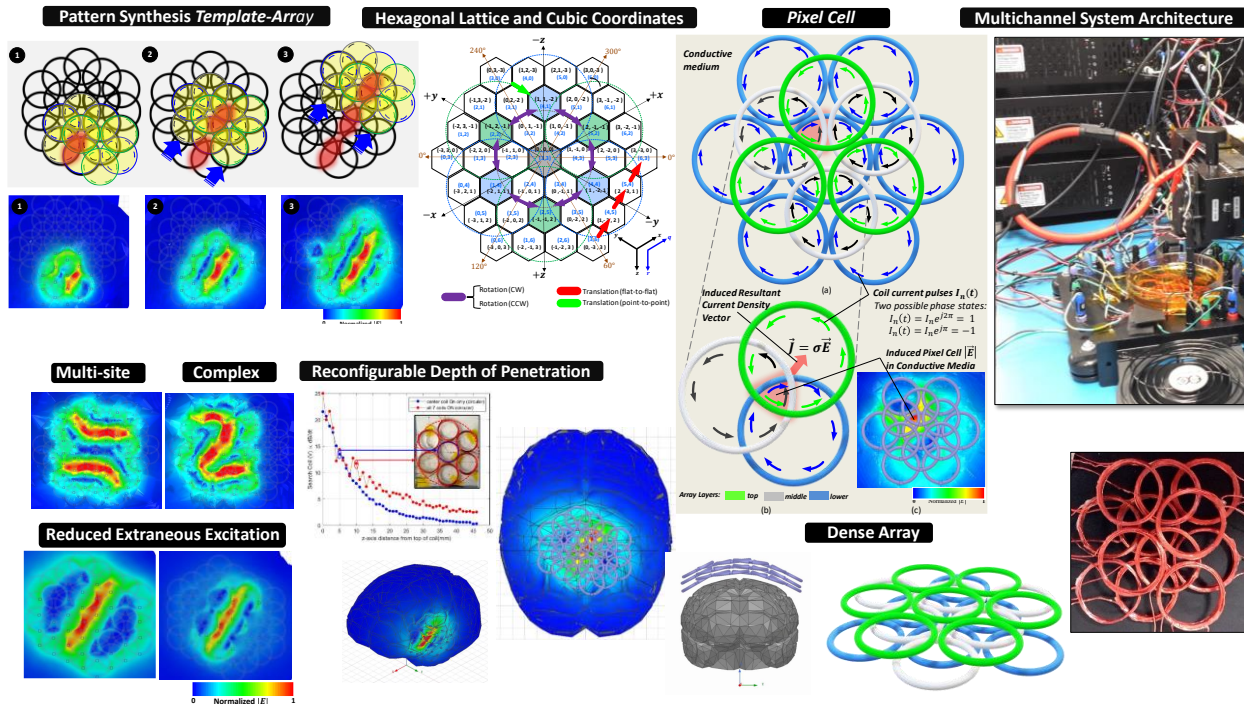


Figure 1.4: Graphical overview of contributions our research has made to the literature.

Despite the many benefits offered by our multichannel 3-layer array system many challenges lay ahead to assess whether it is a tractable implementation for either low-field or high field applications. Although smaller diameter coils, typically used in multi-coil arrays, are more focal there is rapid fall-off of the electromagnetic fields with decreasing coil size. Today it is not possible to manufacture small coils that can survive the significant TMS level currents (kilo-amps), which increase inversely to the square of coil size. The thermal stress due to these currents is destructive and the mechanical strain that pushes the windings apart, due to Lorentz forces, further exacerbates implementation [Wasserman et al, 2008; Mouchawar et al, 1991; Goetz and Deng, 2017]. Nonetheless, smaller diameter coils (<40mm) are being investigated in a wide range of applications in neuromodulation at reduced energy levels. For example, they are being optimized for small animal studies [Selvaraj et al, 2018], Low Field Magnetic Stimulation [Rohan et al, 2014; Wang et al, 2018] and the study of in-vitro cellular level mechanisms using small amplitude agile fields [Grehl et al, 2016]. Therefore, they should be included in a parametric examination of a range of coil diameters, shapes and topologies which is essential to a more comprehensive assessment of benefits and limitations. Also, future advances in material science, superconducting technology, power efficient waveforms and as-yet undiscovered enablers will yield additional technology gap fillers to the implementation challenges.

Although not the focus of this paper, we identify two key examples of these challenges: coil-to-coil mutual coupling effects and increased power consumption due to the increased number of energized coils. We briefly assess the reduction of mutual coupling effects, by experimentally assessing a technique, proposed in a previous study [Han et al, 2004]. Reducing power consumption, is not discussed herein however we are investigating several techniques to reduce it such as power efficient waveforms [Asbeck et al, 2021; Peterchev et al;2008], and optimized coil

current amplitude tapering. Even though our multichannel electronics design is scalable to $I_{\text{peak}} > 1000\text{A}$ (high field TMS levels) it is not deemed a relevant application at this point in development based on the challenges of the 3-layer array. These challenges are not as pronounced at the lower current application of LIMS ($I_{\text{peak}} = 10$ to 30A , peak B-fields: μT - mT range) allowing this fundamental research to initially focus on the synthesis method offered herein while the implementation of the dense array develops. Therefore, LIMS is identified as a more relevant candidate application at this point in the fundamental research reported herein. We then conduct simulations and experiments at individual coil weights of $I_{\text{peak}} = \pm 10\text{A}$ which is in the range of LIMS protocols.

Our objective is not to supplant existing TMS approaches, but to investigate emerging technology, synthesis methods and approaches incrementally in our flexible testbed that has scalability to perform relevant research now at low intensity magnetic stimulation and in the near future approaching relevant high field magnetic stimulation power levels.

1.2 HISTORICAL PERSPECTIVES

Dating back to the ancient Greeks and Egyptians the first use of noninvasive neuromodulation or Electroanaesthesia was used as a remedy for pain reduction. For example, the ancient Greek doctor Largus in 46 A.D. used small electric fish of the species *torpedo nobiliana* to reduce the pain associated with headaches and gout [Kellaway, 1946]. Stimulation of the exposed human cerebral cortex with electrical currents was first reported in 1874 whereby the currents elicited movements of the opposite side of the body [Bartholow, 1874]. Melancholic madness (aka depression) was successfully treated by Aldini [Aldini, 1805] using a series of treatments with the current generated by a voltaic pile invented by Volta in 1799 [Volta, 1799].

Michael Faraday's seminal electromagnetic induction experiment in 1831 [Faraday, 1831] gave rise to the first explorations into magnetic stimulation and the neuronal effects were described in 1896 by d'Arsonval [d'Arsonval, 1896]. He reported phosphenes (flickering lights in the visual field) when placing his head between two coils driven from an alternating 110-volt supply at 30 amperes. Subsequently it is now known that this was due to the direct stimulation of the retina. In 1982 Polson produced a magnetic stimulator capable of peripheral stimulation and recorded the first muscle evoked potential [Polson, 1982]. The technique of transcranial magnetic stimulation (TMS) was established in 1985 when Barker [Barker et al, 1985] achieved magnetic stimulation of the human motor cortex. The development of the concept of multi-coil arrays for (TMS) was first introduced by Ruohonen in 1998 [Ruohonen and Ilmoniemi, 1998] with the goal of enhancing the capabilities of the current art of TMS.

Today a broad range of neuromodulation techniques and devices have evolved based on this research. They can be broken down in four basic categories: subthreshold, suprathreshold, convulsive and surgical emplacement. These categories involve electrical, magnetic, focused ultrasound and temporally interfering signals as the primary means of effecting neuronal activity.

The two categories that directly tie most closely to our research lie within the realm of subthreshold and possibly suprathreshold neuronal stimulation, via magnetic stimulation as enabled our multichannel array system. The key contribution being the introduction, description and validation of our new synthesis method that generates complex and multi-site induced E-field patterns.

1.3 PHYSICS AND BIOPHYSICS

Nonsurgical neuromodulation techniques, such as Transcranial Magnetic Stimulation [Barker et al, 1985], use the magnetic flux density generated by the time-varying current through a coil per Biot-Savart's law [Cheng, 1993] and Faraday's law of induction [Faraday, 1832] as illustrated in Fig. 1.5 (a). In the case of the cortex the optimal trajectory of the E-field is orthogonal to the sulcus for maximum stimulation of a neuronal target (Jansen et al.,2015) as shown in Fig 1.5(b). Fig. 1.5(c) delineates and defines the two types of stimulation (low field or high field) involving either subthreshold or suprathreshold neuronal effects.

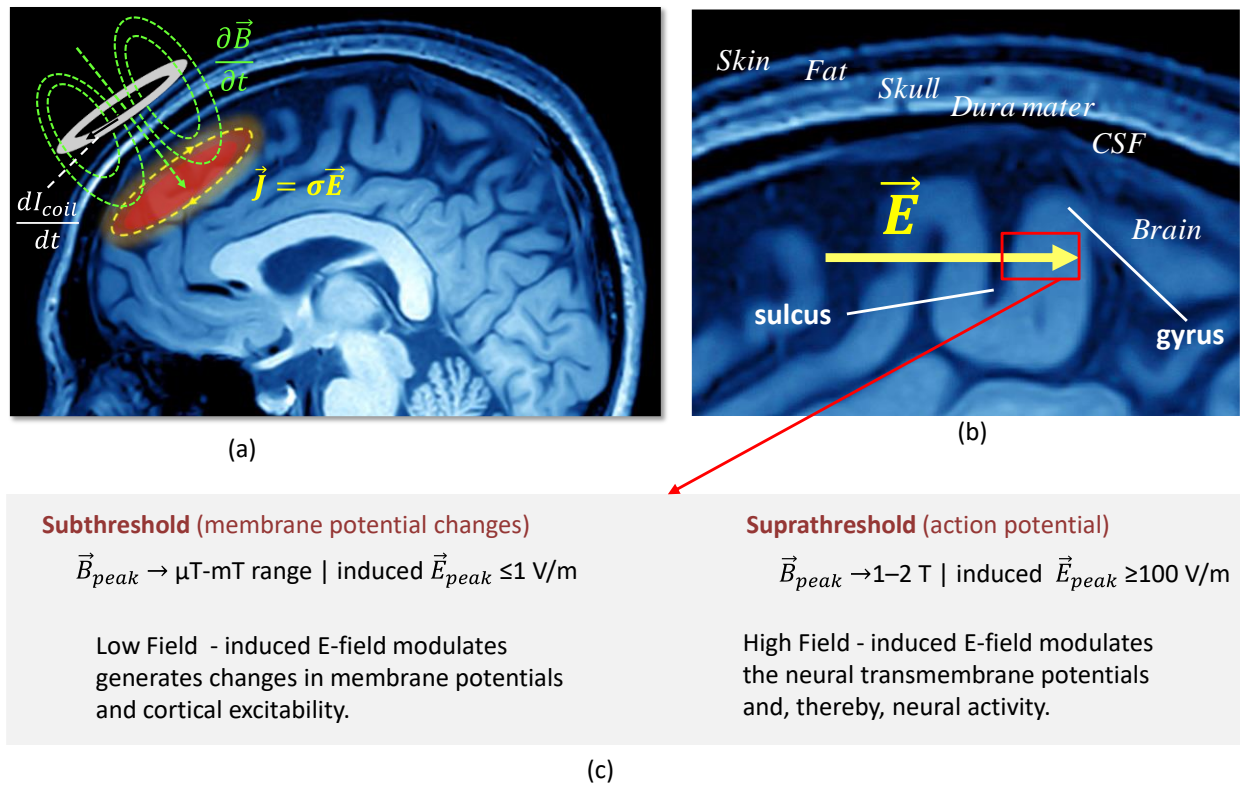


Figure 1.5: The general physics and biophysics of transcranial magnetic stimulation. (a) A time varying current through a coil gives rise to a time varying magnetic field orthogonal to the axis of the coil resulting in the induction of an electric field and eddy currents parallel to the plane of a coil in a conductive media such as the cortex. (b) biophysics - the optimal trajectory of the E-field is orthogonal to the sulcus for maximum stimulation of a neuronal target (c) parameters and neuronal effects of low and high field magnetic stimulation.

There are two components to the total induced E-field, created by the coil, a divergence-free component, and a curl-free component [Heller and Van Hulsteyn, 1992; Salinas et al, 2007]

$$\vec{E}_T = \vec{E}_1 + \vec{E}_2 = -\frac{\partial \vec{A}}{\partial t} - \nabla V \quad (1)$$

where the B-field (\vec{B}) is expressed as the magnetic vector potential (\vec{A}) given $\vec{B} = \nabla \times \vec{A}$ and V is the potential. The primary E-field is directly induced by the time varying magnetic field in the coil, and the secondary E-field, is due to the charges created by tissue-tissue interactions [Salinas et al, 2007].

Many variables effect current densities in tissue: conductivity, permittivity, and stimulus waveforms. However, the design of the coil is perhaps the most significant in how it shapes field patterns, focality, decay profiles and associated intensity levels. The close relationship between the coil current, I_n , the total induced E-field the current \vec{J} in the conductive media can be expressed for an ideal homogenous conductive media as

$$\vec{J}(r) = \sigma \vec{E}_1(r) = \frac{\partial}{\partial t} \frac{\sigma \mu}{4\pi} \int \frac{I_n(r') dl'}{|r-r'|} \quad (2)$$

where r' is the observation location, μ is the magnetic permeability of the media, σ is the conductivity of the media and l' is an individual segment of the conductive media.

The function of a stimulation coil whether singular, multiple or in array topologies, is to spatially distribute the magnetic field and in turn spatially distribute the induced electric field and the current flow in the brain. Therefore, the amplitude of the induced electric field depends on magnetic field amplitude, how fast it changes over time and its direction [Grehl, 2016; Esselle, 1992].

An important spatial aspect of magnetic stimulation involves the fundamental limitation of the induced E-field is that one cannot achieve a 3D focus in depth. In other words, one can't achieve a strong E-field deep in cortex and with weak E-fields in the structures above it. Thus, focality of the induced E-field is defined as the 2D spread of E_{max} which is described in later sections.

The stimulation coil stores energy from the time-varying magnetic field when the pulsed current (I_{peak}) runs through it according to the Biot-Savart law [Cheng, 1993] in the expression

$$\vec{B}_z = \frac{\mu_0 N I R^2}{4\pi(R^2+z^2)^{3/2}} \int_0^{2\pi} d\Phi = \frac{\mu_0 N I R^2}{2(R^2+z^2)^{3/2}} \quad (3)$$

In general, B-fields attenuate with the inverse square of the distance from a “point of current” or current segment. Larger coil diameter results in deeper penetration and more gradual decay than the smaller diameter coil as shown in Fig. 1.6 using Eqn. (3).

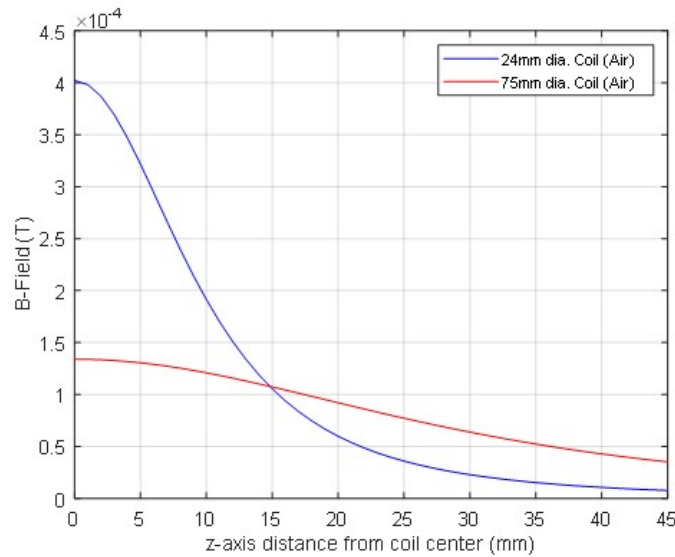


Figure 1.6: The decay of the magnetic field from coil center. Small coils have large magnitudes but decay rapidly whereby large coils decay slowly with but with low magnitudes.

The temporal aspects of neuromodulation are predicated on a rapid B-field rise time to a maximum of 100 μ s followed by a slow decay up to 1ms. The rate of change (dB/dt) of the B-field, rather than simply the magnitude of the field, has the more important role to play in the efficiency of the coil design. However, it is the E-field that plays the greatest role as the rate of change determines the intensity of the induced field as is evident in Fig. 1.7. For example, a strong magnetic field with a slow rate of change will induce a low intensity electric field. Conversely, a weak magnetic field with a fast rate of change will induce a strong electric field. Thus, the key metric is the E-field in Fig. 1.7 as it shows that the greater part of the stimulus occurs within the first 100 μ s. The rate of change values can be used to estimate the induced electric field strength but is more useful in the context of engineering and coil design, because the coil design properties may limit the rate of change.

Brain neurons show improved response to stimulation waveforms using square waves over that of sinusoidal waveforms. It is postulated that the neuronal membrane acts as a capacitor and as it connects in series with the extracellular and intracellular resistance serving much like an RC circuit [Deng et al, 2013].

The primary waveform used in this study involves a monophasic waveform—damped cosine. However, the system is flexible in that it can also generate biphasic waveforms. In this case, most of the current returns to the capacitor in the 2nd phase of a complete cycle.

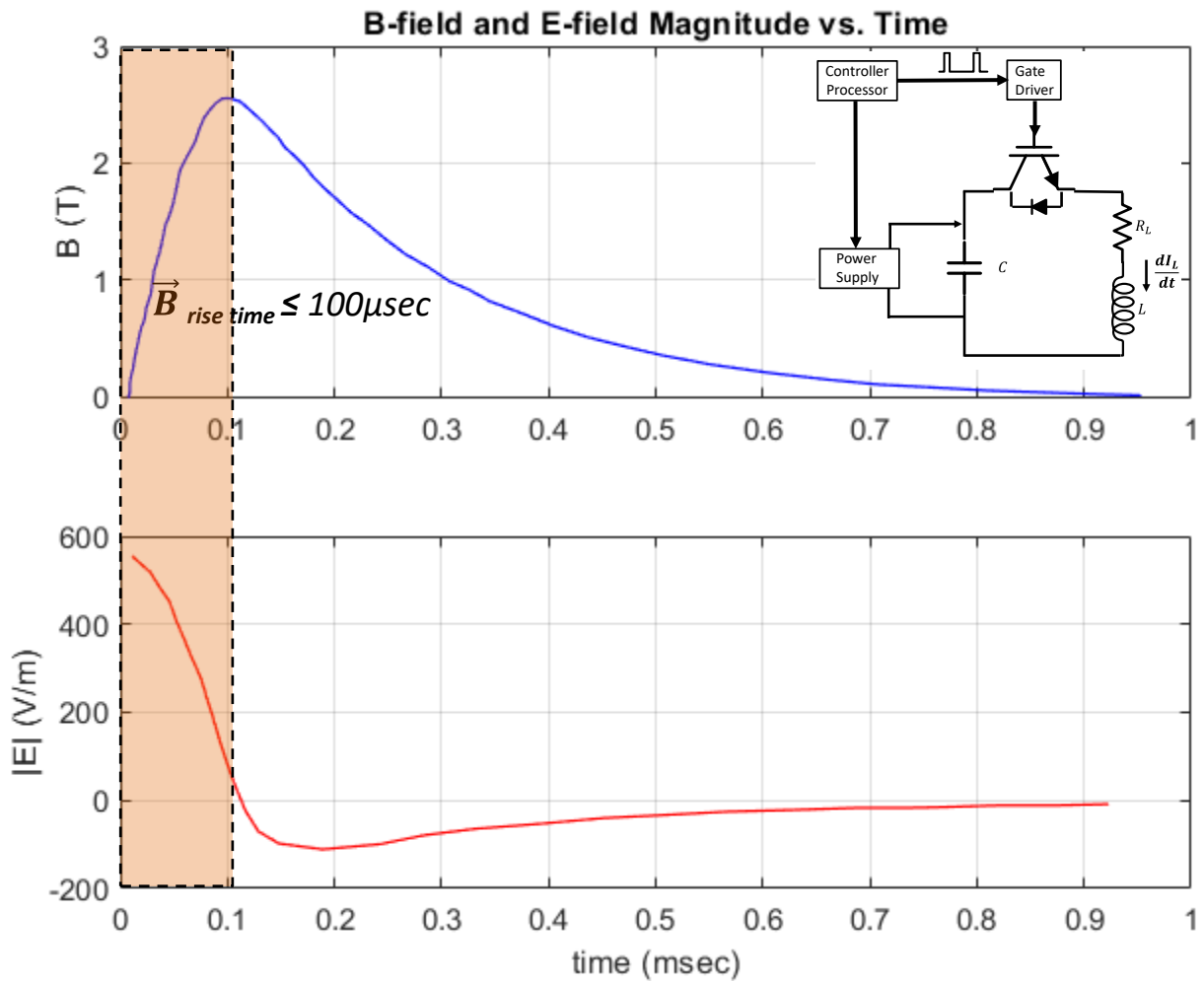


Figure 1.7: Temporal aspects of the B-field and E-field in magnetic stimulation rate of change ($\frac{dB}{dt}$) most important parameter for E_{max} .

1.4 SCOPE OF THESIS

The primary objective of this work is to propose, using our new synthesis method, what other types of patterns are “possible” and perhaps useful in future biomagnetic applications. We demonstrate with simulations and experimental results that the generation of sharply curved or irregular patterns at singular and multiple sites is possible with this method. For an illustration, a

traditional figure-8 coil pattern is compared to two patterns formed by the synthesis method using our 3-layer array, in Fig.1. This method is enabled by a multichannel 3-layer array system previously reported by the authors [Smith et al, 2021].

Chapter 2 is a detailed discussion on the synthesis method and its three primary components; a *pixel cell* (basic unit of pattern formation), a *template array* (“virtual array” - code that disseminates the coil current weights to the “physical” dense array), and a hexagonal coordinate system.

Chapter 3 verifies the synthesis method through simulations and experimental results that highly curved or irregular (e.g., zig - zag) patterns at singular and multiple sites can be efficiently formed using our proposed method. These are the first synthesized highly curved and irregular E-field patterns (singular and multi-site) reported in the literature to the best of our knowledge. This method was enabled by a multichannel 3-layer array system previously reported by the authors [Smith et al, 2021].

Chapter 4 provides a detailed treatment on the simulations and measurements on the ability to provides a reconfigurable depth of penetration using both circular and hexagonal shaped coils using the lower planar array in our multi-coil array. The depth of penetration of the magnetic field can be reconfigured by varying current magnitude and phase of the smaller coil diameters in the array to achieve the same decay profile performance of a larger diameter coil. Only simulations exist in the literature to date, to the best of our knowledge, we report the first measurements of hexagonal shaped coils in multi-coil arrays have increased depth of penetration over circular shaped coil-based arrays. Similar multi-coil arrays have been simulated in the literature using circular coils [Yang et al, 2010; Wei et al, 2017; Ho et al, 2009]. However, to the best of our knowledge, we are the first to measure the synthesized depth of penetration using a multi-coil

dense array system. Moreover, this is the first study involving the measurement of depth of penetration for hexagonal coils in dense arrays.

Chapter 5 proposes a new technique for reducing extraneous excitation or improved localization of a pattern is proposed with supporting discussion and simulations. When eddy currents are generated in a conductive solution (e.g., cortical tissue), they must form continuous paths, i.e., they generate return currents, as required by Kirchhoff's laws and the continuity equation. Any stimulated region thus causes additional stimulation in the surrounding tissues. The advantage of the proposed approach is that it provides complete control over the current profile on the entire surface of the brain, allowing us to manipulate the spatial extent of the return currents. By spreading them out over a large area we can reduce their density until it is far below the stimulation threshold.

Chapter 6 provides a description of the prototype multichannel system architecture that was designed and fabricated to support the research conducted in this study. This includes power electronics, packaging, coils and the dense array topologies used.

Chapter 7 details the near-field techniques by which the E-fields and B-fields were measured for this research. These techniques are validated by comparing them to traditional and well-known E-field contour patterns in the literature. Also, finite element modelling methodology is described both in ideal homogeneous conductive solution and a realistic brain model are described. A general figure of merit is defined on how the E-field is modulated at depth in the conductive solution.

Chapter 8 reports the experimental results for the mitigating of proximity effects, one of the major challenges in the implementation of multi-coil dense arrays.

Chapter 9 provides a conclusion and summary of the body of research conducted in this research. Here over major contributions are highlighted as contributions to the literature. Next steps in this research and adjacent applications are also discussed.

CHAPTER 2 SYNTHESIS METHOD | PRINCIPLES OF OPERATION

2.1 INTRODUCTION

The general principles for our synthesis method using the *pixel cell* as fundamental unit of construction are described herein. At the onset of development, the main objective was to find a coordinate system that could index the coil current weights for all three array layers in one grid and coordinate system. The system also needed to support mathematically efficient movement (rotation and translation) across a given grid to facilitate ease of programming in NumPy [Harris et al, 2020], the math library within Python. A hexagonal coordinate system with a hexagonal grid with a mapping to cubic coordinates were selected and found to best support these objectives. Also, axial coordinates and indices, closely related to cubic coordinates, were used to store coil current weights ($I_n e^{j2\pi} = 1, I_n e^{j\pi} = -1, \text{ or } 0$) and perform mathematical operations to transfer the data. These general techniques were adapted from image processing [Vojtěch et al, 2016].

2.2 PIXEL CELL

The shape formed by the intersecting coils of three layers is, geometrically a Reuleaux triangle [Weisstein, 2022], coined the *pixel cell* in Fig. 2.1. It is defined as the fundamental building element for the synthesis of excitation patterns by the dense array. This triangular region induces eddy currents in three directions with return currents spread over the conductive media underneath the array. Currents are deemed more tractable when one considers the fact that a time-varying current in a coil creates a magnetic field normal to the coil, which in turn induces an E-field and current density vector in a specific direction in the neuronal target area.

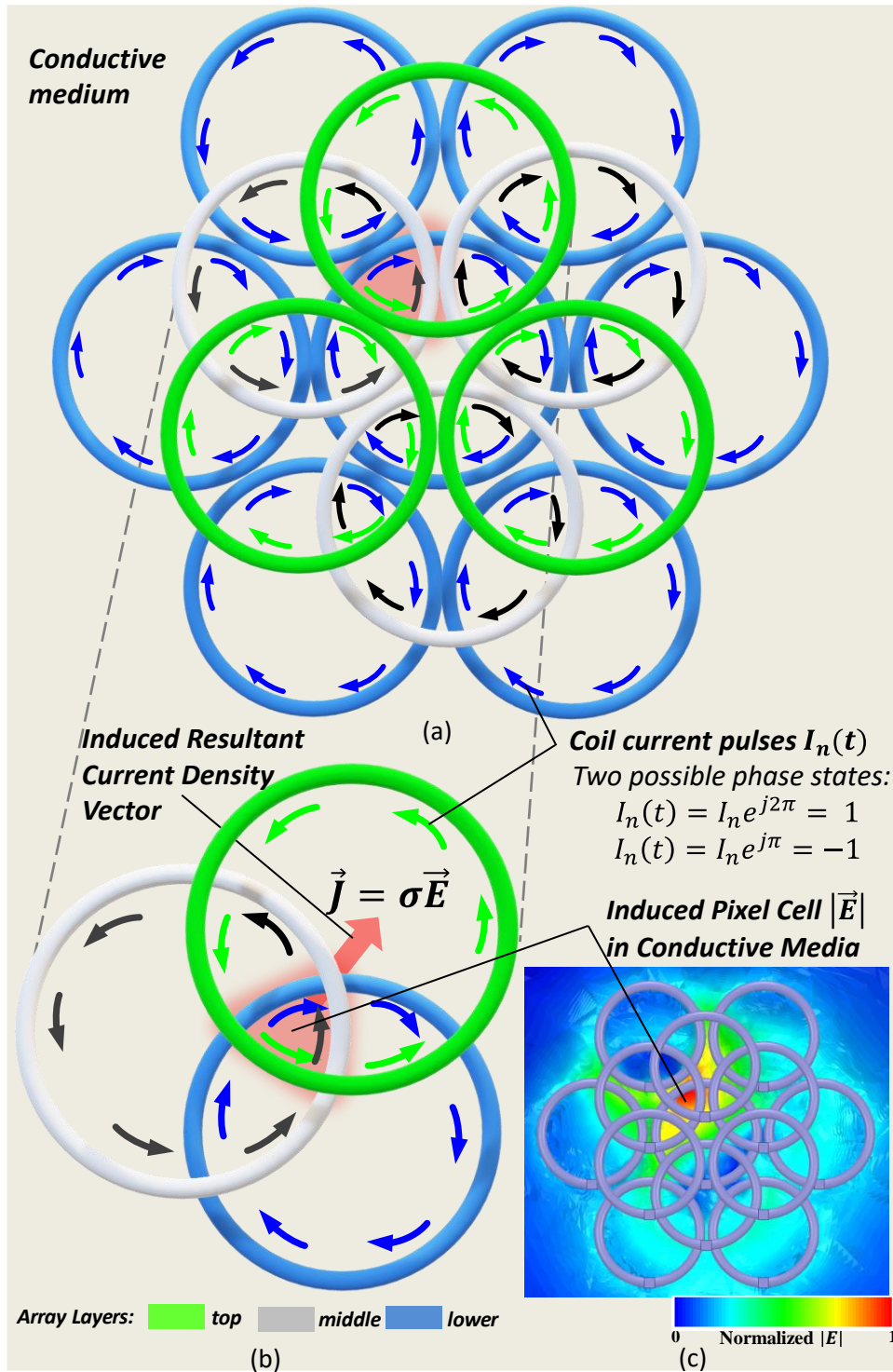


Figure 2.1: A *pixel cell* is induced in a conductive medium (note: excitation site in red). (a) 13-coil three-layer array with requisite coil current weights (magnitude and phase, 0 or π), (b) three overlapping coils form a *pixel cell* mapped to specific drive coil giving rise to a resultant current vector in the *pixel cell* and, (c) simulation of induced E-field magnitude of a single *pixel cell* excitation.

The coil weights in each of the three intersecting coils in Fig 2.1 (b) giving rise to a *pixel cell* that induces \vec{E}_{max} as simulated Fig. 2.1 (c). There are two components to the total induced E-field, created by the coil, a divergence-free component, and a curl-free component [Heller and Van Hulsteyn, 1992; Salinas et al, 2007]

$$\vec{E}_T = \vec{E}_1 + \vec{E}_2 = -\frac{\partial \vec{A}}{\partial t} - \nabla V \quad (1)$$

where the B-field (\vec{B}) is expressed as the magnetic vector potential (\vec{A}) given $\vec{B} = \nabla \times \vec{A}$ and V is the potential. The close relationship between the coil current, I_n , the total induced E-field the current \vec{J} in the conductive media can be expressed for an ideal homogenous conductive media as

$$\vec{J}(r) = \sigma \vec{E}_1(r) = \frac{\partial}{\partial t} \frac{\sigma \mu}{4\pi} \int \frac{I_n(r') dl'}{|r-r'|} \quad (2)$$

where r' is the observation location, μ is the magnetic permeability of the media, σ is the conductivity of the media and l' is an individual segment of the conductive media.

2.3 INDUCED CURRENTS | VECTOR ANALYSIS

The following analysis describes how the close relationship between synthesized coil currents $I_n(t)$ and induced current density \vec{J} , in a conductive medium, are exploited to create arbitrary patterns. Three intersecting coils in the three-layer array form a discrete triangular intersection region, the *pixel cell*, offering a fundamental unit of construction. Six equilateral triangles cover the area of a coil in Fig. 2.2 and are assigned to each pixel cell. This facilitates basic current density vector analysis whereby the line segments of the triangle provide the relative

vector weighting in each direction that combine to give the resultant vector and current direction for a given pixel. A 30° tilt of the triangle to the standard reference axis is performed for convenience for each of the pixel variant examples in Fig. 2.2. The general expression for the relationship between the time-varying current in each of the three layers of coils, the induced E-field and current density vectors in the conductive medium at an excitation pixel is

$$\vec{J}_{t_{qr}} = j_{t_{qr}}\hat{x} + j_{t_{qr}}\hat{y} = \sigma\vec{E}_{t_{qr}} \quad (3)$$

where $\vec{J}_{t_{qr}}$ is the resultant induced current density vector, $j_{t_{qr}}\hat{x}$ and $j_{t_{qr}}\hat{y}$ are the vector components, t_{qr} is the specific pixel, σ is the conductivity (S/m) of a tissue equivalent solution, and \vec{E} is the induced E-field. The x and y axis induced current vector components are then expressed as

$$j_{t_{qr}}\hat{x} = \left(\pm \left(\frac{dI_{top}}{dt} \right) \delta_x \pm \left(\frac{dI_{mid}}{dt} \right) \delta_x \pm \left(\frac{dI_{lower}}{dt} \right) \delta_x \right) \hat{x} \quad (4)$$

$$j_{t_{qr}}\hat{y} = \left(\pm \left(\frac{dI_{top}}{dt} \right) \delta_y \pm \left(\frac{dI_{mid}}{dt} \right) \delta_y \pm \left(\frac{dI_{lower}}{dt} \right) \delta_y \right) \hat{y} \quad (5)$$

where dI_{qr}/dt is the time-varying current in the coil in a specific array layer (i.e., top, mid, and lower) and δ represents the component vector weight projections predicated on the line segments of the triangle. In this section the peak drive coil current magnitudes normalized for simplification. Several variants of the pixel cell are characterized in Fig. 2.2 They are the single excitation pixel, the two-pixel excitation unit and a single null pixel. A single excitation pixel in a 13-coil array is illustrated in Fig. 2.2(a) along with its simulated E-field in Fig. 2.2(b). An enlarged view of this array's central area, in Fig. 2.2(c), reveals the requisite coil weights that induce the current density

vectors for the pixel t_{qr} . Using Eqn. (3), (4) and (5) yields the magnitude and direction of total induced current density vector, $\vec{J}_{t_{qr}} = \hat{x} + \sqrt{3} \hat{y}$ illustrated in Fig. 2.2(d).

A two-pixel excitation unit in a 13-coil array is illustrated in Fig. 2.2(e) along with its simulated E-field in Fig. 2.2(f). An enlarged view of this array's central coil, in Fig. 2.2(g), reveals the requisite coil currents and phase vectors that induced the current density vectors for the pixels t_{qr} . Using Eqn. (3), (4) and (5) yields the magnitude and direction of total induced current density vector, $\vec{J}_{t_{qr}} = -2\sqrt{3} \hat{y}$ illustrated in Fig. 2.2(h).

A single null pixel in a 13-coil array is depicted in Fig. 2.2(i) along with its simulated E-field in Fig. 2.2(j). An enlarged view of this array's central coil, in Fig. 2.2(k), reveals the requisite coil currents and phase vectors that induce the current density vectors to cancel or null the pixel t_{qr} . Using Eqn. (3), (4) and (5) yield the magnitude and direction of total induced current density vector, $\vec{J}_{t_{qr}} = 0$ illustrated in Fig. 2.2(l).

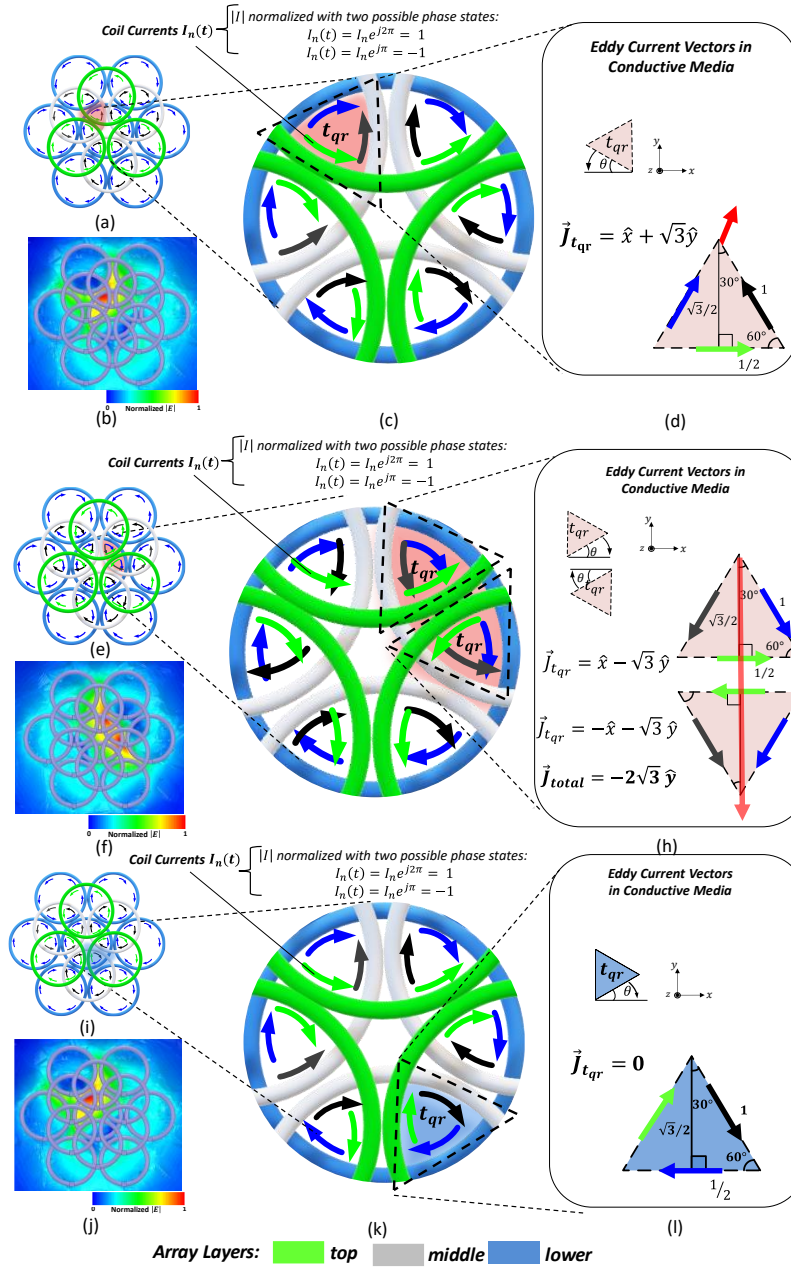


Figure 2.2: Three variants of a pixel cell are characterized in a 13-coil array (note: excitation site is depicted in red and null in dark blue). (a) coil layers and current phase excite a single pixel in a 13-coil array, (b) FEM of E-field of the pixel, (c) enlarged view - center coil and induced current density vectors for the pixel t_{qr} , (d) magnitude and direction of total induced current density vector, $\vec{J}_{t_{qr}} = \hat{x} + \sqrt{3} \hat{y}$, (e) coil layers and current phase to excite a single double-pixel in a 13-coil array, (f) FEM of E-field of the double-pixel, (g) enlarged center coil and induced current density vectors for the summing of the two pixel t_{qr} , (h) the magnitude and direction of total induced current density vector, $\vec{J}_{t_{qr}} = -2\sqrt{3} \hat{y}$, (i) coil layers and current phase to create a single null pixel in a 13-coil array, (j) FEM of E-field of the null pixel, (k) enlarged view of center coil induced current density vectors for the pixel t_{qr} , (l) the magnitude and direction of total induced current density vector, $\vec{J}_{t_{qr}} = 0$.

At this point in the development of the synthesis method it was clear that an a-priori knowledge of the pixel excitation criteria could allow one to intuitively form arbitrary patterns based primarily on pixel cells. A singular pixel or it's variant (a null or double-pixel), based on these simple vector relations of eddy currents, can be placed intuitively anywhere on a 3-layer lattice of coils as is shown in Fig. 2.3 and Fig. 2.4. The next step was to devise an efficient method of synthesis that indexed all three current coil weights (one weight per layer) in the 3-layer array that allowed for efficient formation of patterns based on pixel cell.

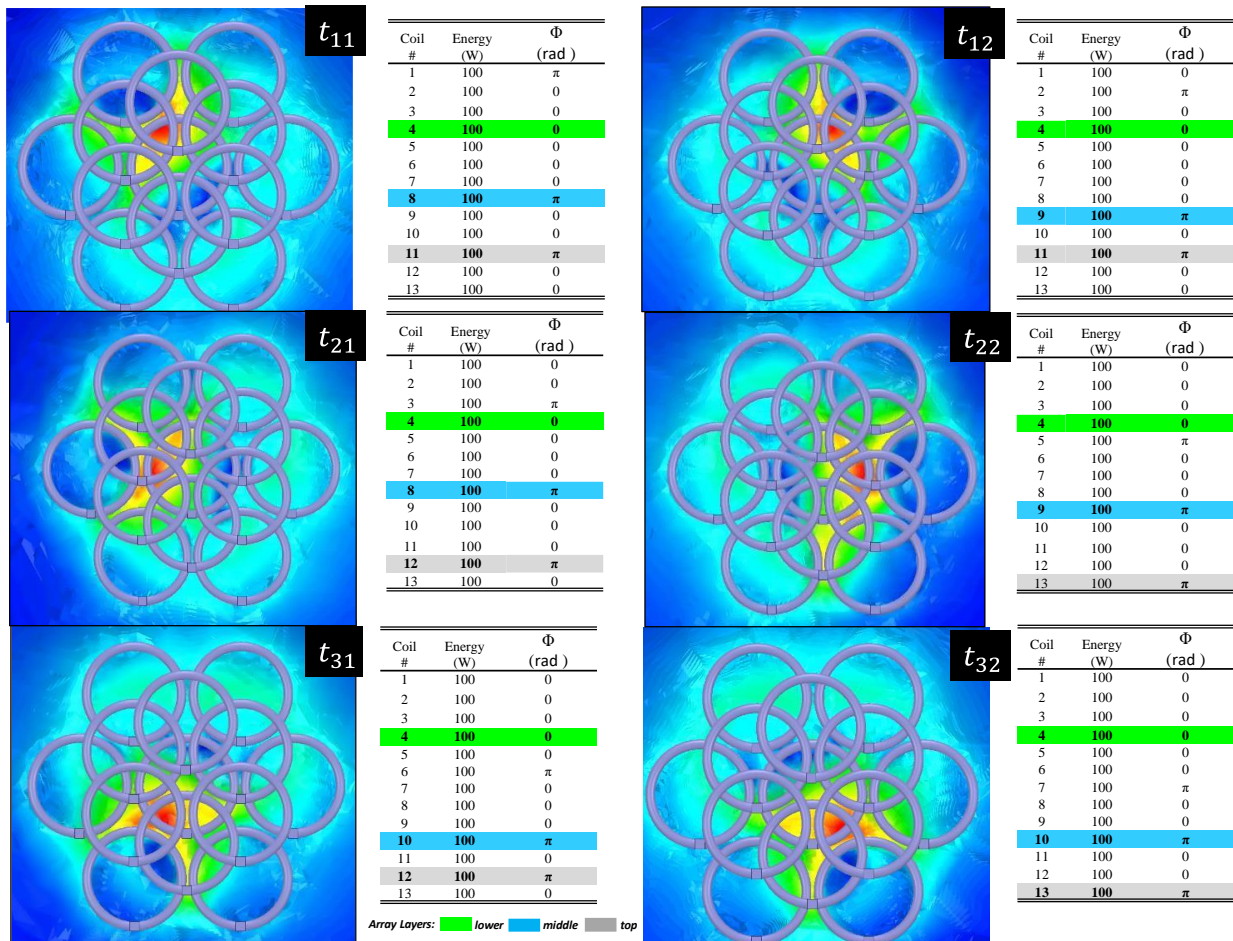


Figure 2.3: The manipulation of a single pixel cell in a clockwise path is easily created using the general rules of forming a pixel.

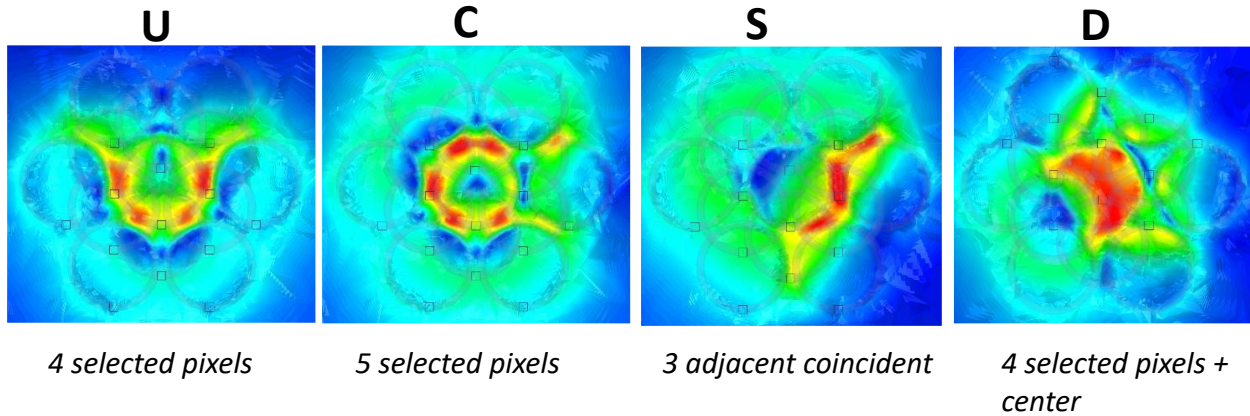


Figure 2.4: A notional display of “UCSD” yields simple intuition-based patterns.

2.4 TEMPLATE ARRAY

The *template array* exists in software (i.e., hash table) and moves/transfers coil current weights using hexagonal coordinates to the “physical array” (aka *resident array*) that forms the pattern. Three variations or *zones* shown in Fig. 2.5, when pre-loaded with a set of coil weights, create a desired *pixel unit* (e.g., double - pixel) in which the *template array* aligns and transfers this data to the *recipient array* for pattern synthesis. These steps repeat n number of steps until pattern completion. These pre-loaded coil current weights ($I_n e^{j2\pi} = 1, I_n e^{j\pi} = -1$ or $0, I_n$ is normalized) reside in a hash table and are loaded into the *template array* using the pixel configuration that is selected for pattern formation. The double-pixel, in Fig. 2.5 and 2.6, is uniquely suited for synthesis as the surrounding return currents, in all three layers of the array, are spread out and cancel as they move away from the excitation area. As such, this variant is used throughout this paper as the primary unit of construction.

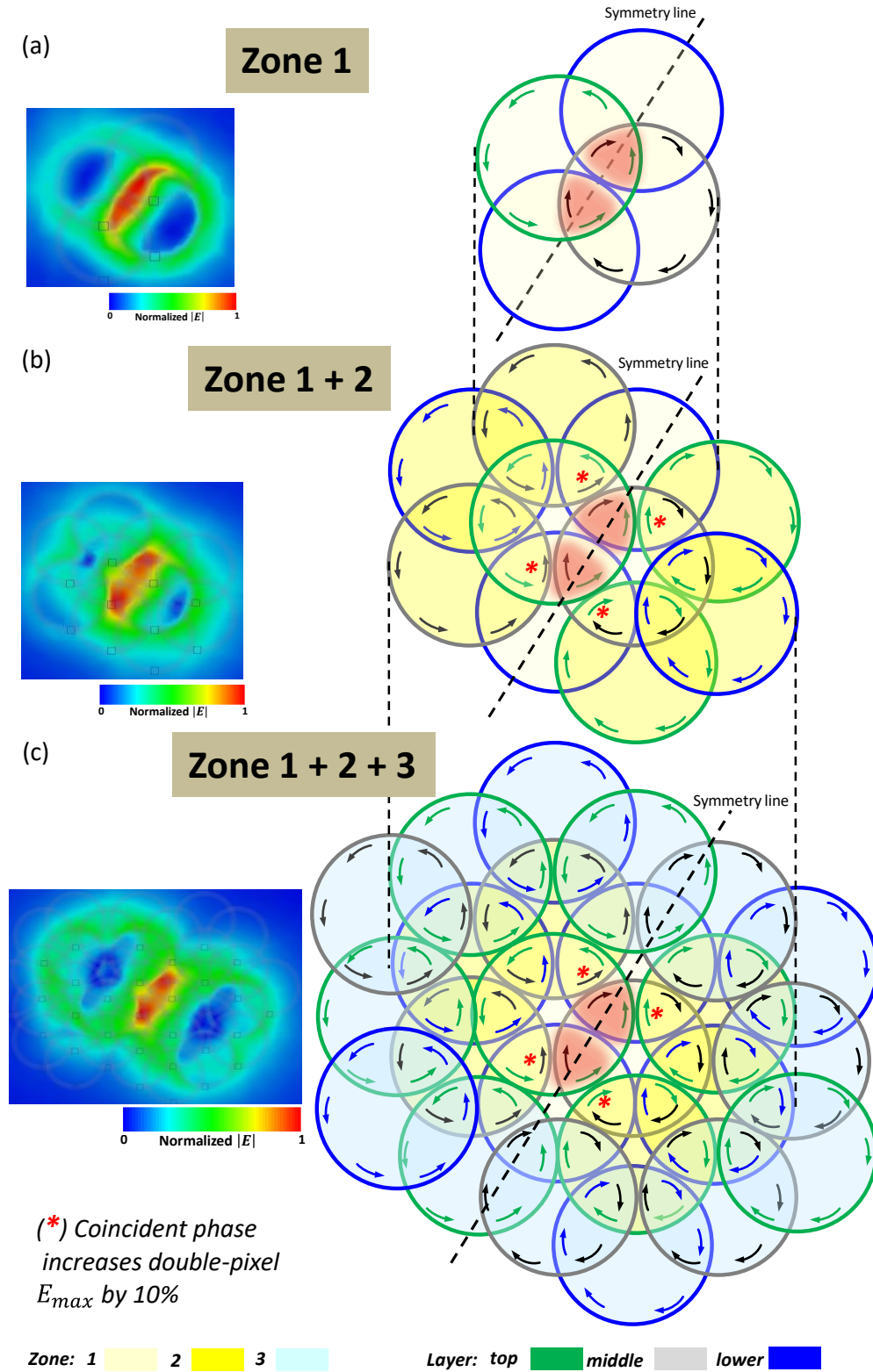


Figure 2.5: The *template array*, with three variants or zones, is pre-loaded, from a hash table in the code, with coil current weights creating a double-pixel unit of construction for pattern formation. (a) *zone 1* (4 coils), (b) *zones 1 + 2* (10 coils) and (c) *zones 1 + 2 + 3* (32 coils).

As the *zones* are added there is also an increase in the magnitude of the induced E-field (~10%) in the pixel due to the coincident current phases of the neighboring coils shown in Fig. 2.5(b) and (c). Also, the increase in coils, as each *zone* is added, allows for additional paths to spread return currents farther out and away from the induced E-field.

The next step in pattern synthesis is now described in Fig. 2.6 whereby user-defined coil current weights in the *template array* are transferred to the underlying *recipient array* for the construction of a desired pattern or multiple patterns. The general concept is illustrated in Fig. 2.7(a)-(b) whereby the *template array* steps, repeats, and transfers the identical coil current weights in the three designated positions. This is followed by the superposition of each pixel current density array pattern from each step, seen in Fig. 2.7(b), giving rise to the unilinear pattern and the supporting simulations shown in Fig. 2.7(c).

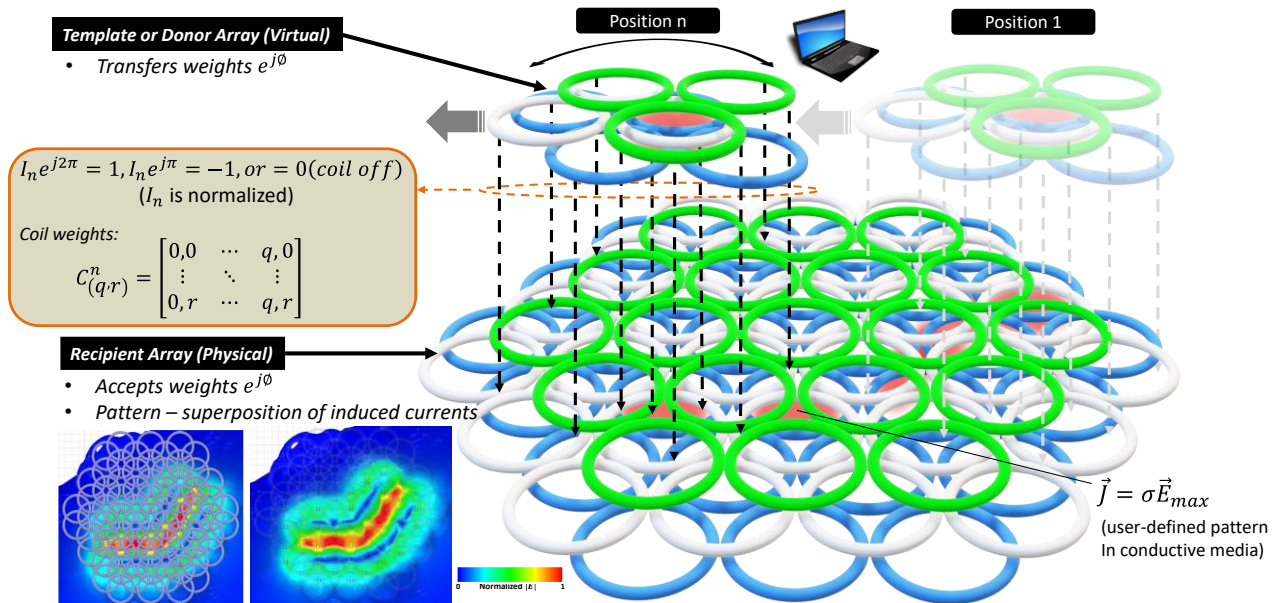


Fig. 2.6. *Template array* is a “virtual entity” that aligns with *recipient array* and transfers the drive coil current weights to *recipient array* to form a user-defined pattern in the conductive media.

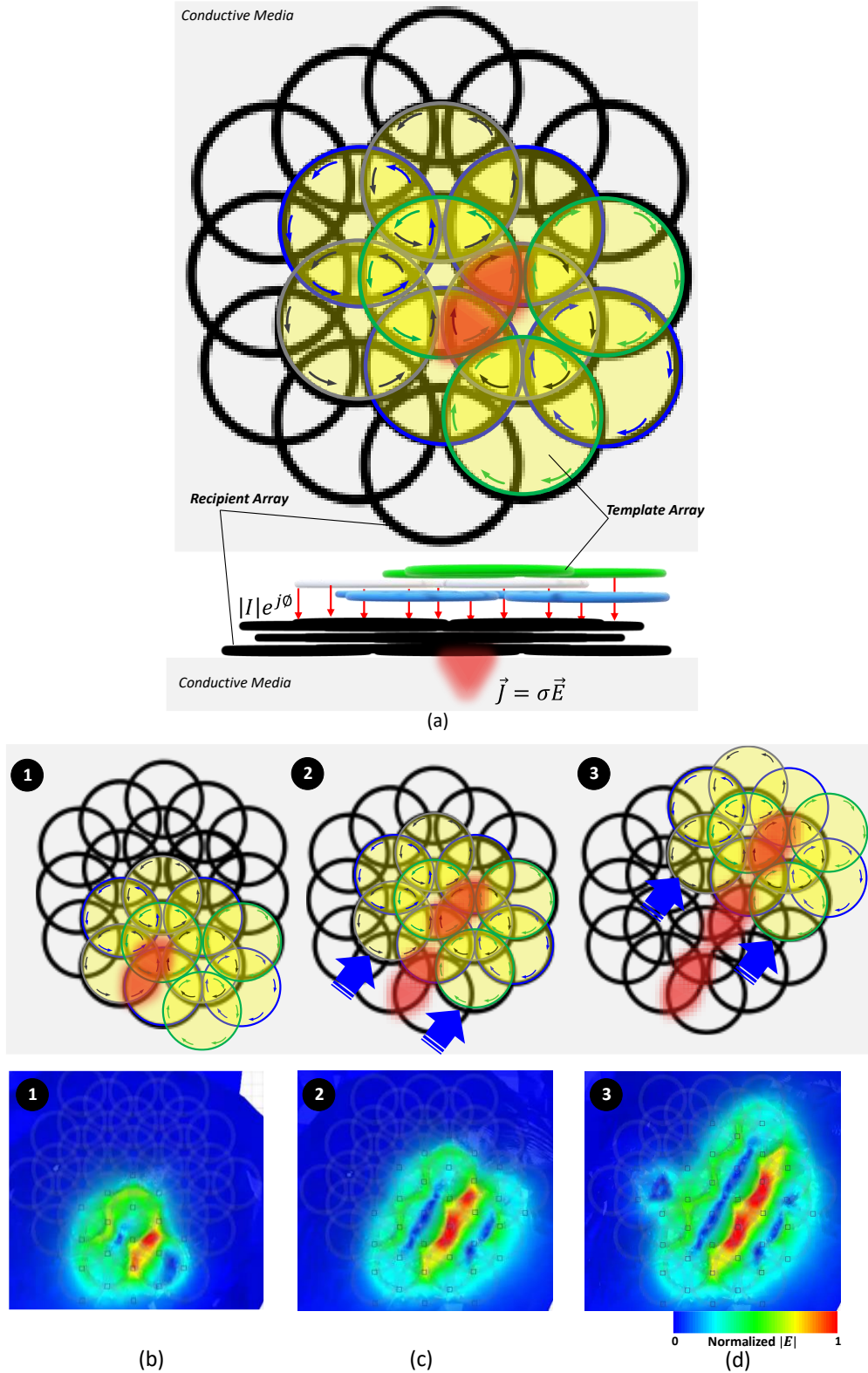


Fig. 2.7. Synthesis of a pattern with the *template array* using a double-pixel cell as the unit of pattern construction (note: excitation site in red). (a) pre-translation; a *template array* aligns with *recipient array* and transfers the user-defined current magnitudes and phases, (b) post-translation; a series of steps 1 – 3 are repeated to form a user-defined pattern, (c) FEM of the post-translation a series of steps 1 – 3.

In each step, the template array is aligned and mapped to the hex grid using the identical cubic coordinates as the recipient array as illustrated in Fig. 2.7(b). In other words, the template array's sole function is to act as a pixel "stamp" that imprints the pattern to the recipient array as shown in Fig. 2.7(b). For a desired pattern then a step and repeat process, shown in Fig. 2.7(c), ensues accordingly until pattern completion. Notably, this concept was initially developed using a light table with a transparency of the template array moving over the stationary recipient array. Thus, the computer code is not obligatory but increases speed of pattern generation.

2.5 HEXAGONAL LATTICE AND COORDINATE SYSTEM

The synthesis component that facilitates the rotation and translation of *template arrays*, comprised of coil current weights, that form *pixel cells* is the cubic coordinate system. Cubic coordinates on a hexagonal grid allow for easy rotation and translation of pixel cells over that of square grids mapped to cartesian coordinate systems. This is due in part to the fact that they have only six equidistant neighbors as opposed to eight unequal distances in a square grid as illustrated in Fig. 2.8. As such, a simple system of coordinate transformation negates the need for trigonometric functions as seen in square and triangular grids. Also, axial coordinates, a close relation to cubic coordinates, allows for easy storage of coil weights ($I_n e^{j2\pi} = 1, I_n e^{j\pi} = -1$ or $0(\text{coil off})$). After movement is completed, then cubic coordinates are converted to axial coordinates in both arrays for data storage and source indexing for the coils in HFSS and verification.

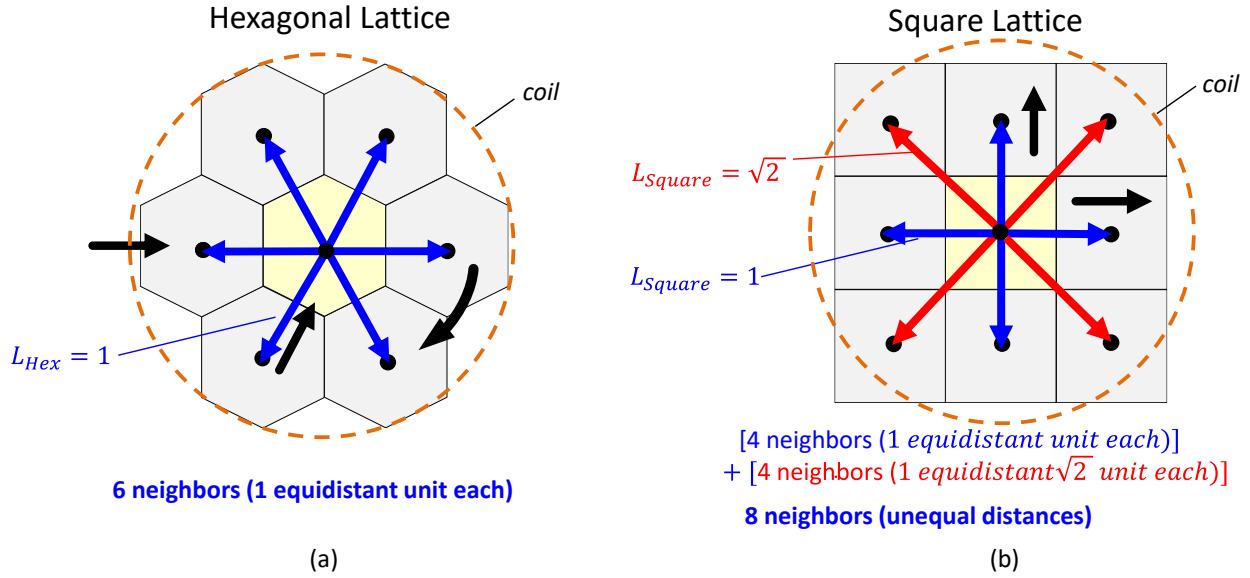


Fig. 2.8. Comparison of hexagonal lattice to a square lattice. (a) hexagonal lattice and (b) square lattice.

Several basic movements are described in Fig. 2.9 using cubic coordinates when mapped to a hexagonal grid. The center point of every coil in the dense array is referenced to the center hexagon (note: hexagons are color coded to match the colors of the coils in Fig. 2.1, Fig. 2.2 and 2.5) and the associated cubic coordinate. The general constraint for cubic coordinates is

$$x + y + z = 0 \quad (6)$$

Corresponding axial coordinates (blue font in Fig. 2.9) are defined as

$$q = x, \quad r = z, \quad y = -x - z \quad (7)$$

A clockwise (CW) rotation around the grid, in Fig. 2.8, is achieved by a simple transformation of cubic coordinates every 60° using

$$(x, y, z) \rightarrow -(z, x, y) \quad (8)$$

A counterclockwise (CCW) rotation, in Fig. 2.9, around a specific ring is achieved by a simple transformation of cubic coordinates every 60° using

$$(x, y, z) \rightarrow -(y, z, x) \quad (9)$$

Translation from hex flat-to-flat, seen in Fig. 2.9 (red arrows), for a given direction changing one of the 3 cube coordinates by +1 and changing another one by -1 (the sum must remain 0). For example, moving away 240° on the hex grid between the +y and -z, will result in adding 1 to y and subtracting 1 from z.

$$0^\circ \Rightarrow (x, y, z) \rightarrow (x + 1, y - 1, k) \quad (10)$$

$$60^\circ \Rightarrow (x, y, z) \rightarrow (k, y - 1, z + 1) \quad (11)$$

$$120^\circ \Rightarrow (x, y, z) \rightarrow (x - 1, k, z + 1) \quad (12)$$

$$180^\circ \Rightarrow (x, y, z) \rightarrow (x - 1, y + 1, k) \quad (13)$$

$$240^\circ \Rightarrow (x, y, z) \rightarrow (k, y + 1, z - 1) \quad (14)$$

$$300^\circ \Rightarrow (x, y, z) \rightarrow (x + 1, k, z - 1) \quad (15)$$

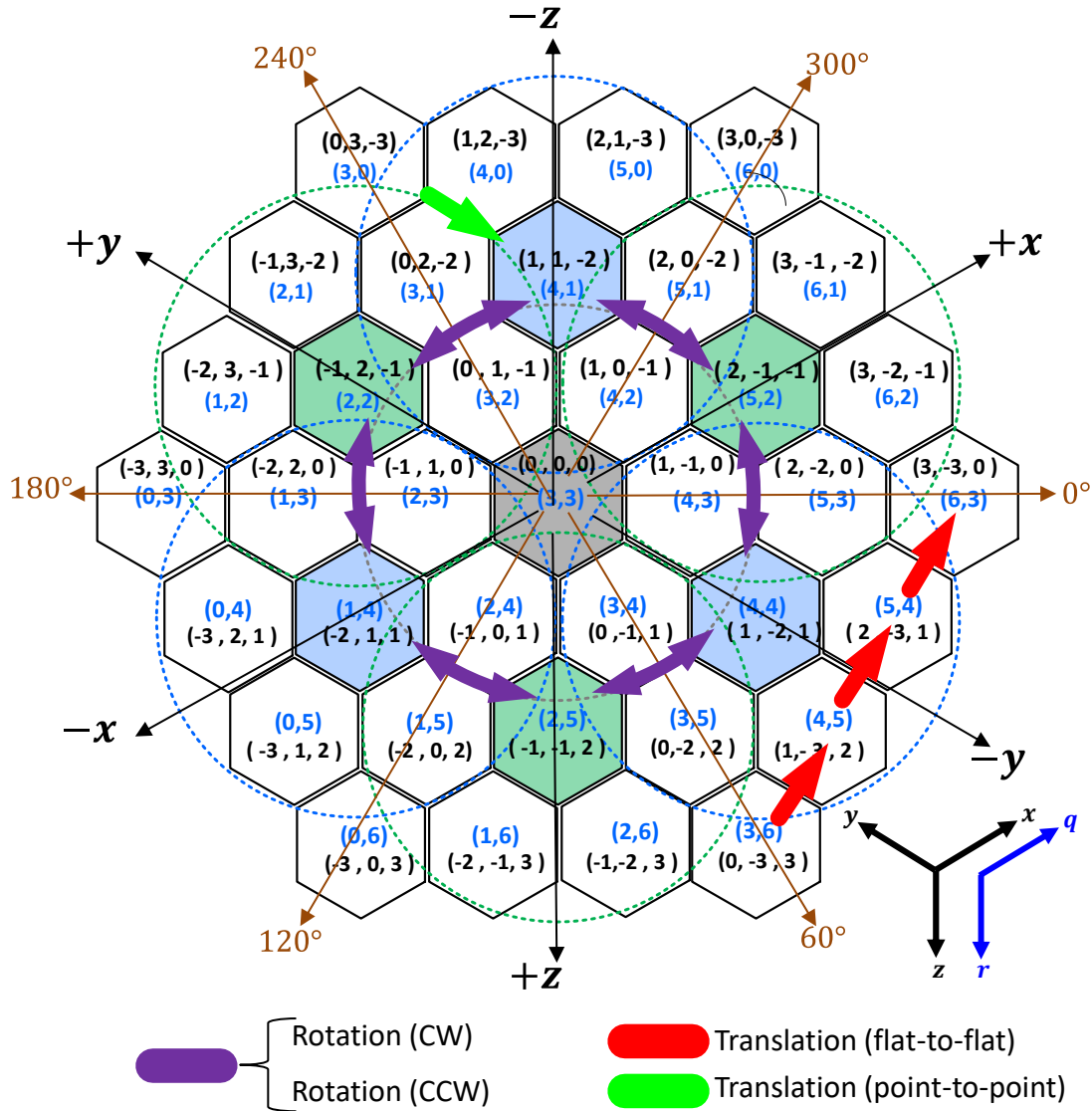


Figure 2.9: Movement using cubic coordinates (note: in black font) on a hexagonal grid and axial coordinates (note: in blue font) are used for data storage (note: the axial coordinates are re-referenced for array storage).

Translation diagonally, in Fig. 2.9 (green arrow) from hex vertex-to-vertex involves changing one of the three cubic coordinates by ± 2 and the other two by ∓ 1 with the sum remaining 0 per Eqn. (6).

An example of a storage array using axial coordinates (note: re-referenced) for the hex grid in Fig. 2.10 and Eqn. (16) shows that the nulls are used to fill in the unused sections of the pre-rotation and post-rotation values in the array due to the hexagonal shape (flat top orientation).

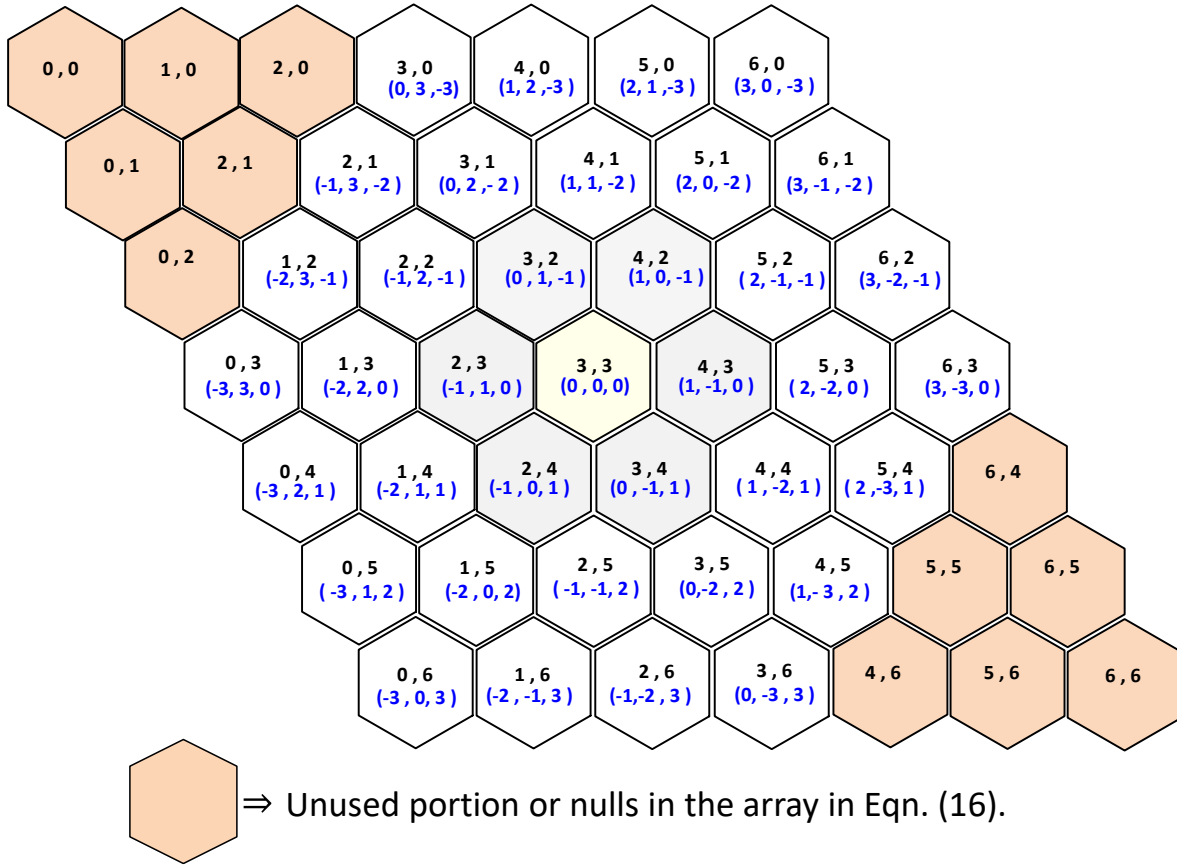


Figure 2.10: Example of axial coordinates/indices (re-referenced to left column) and corresponding cubic coordinates mapped to a hexagonal grid (note: unused portions are in tan shading and are designated nulls in the array in Eqn. (16)).

$$C_{(q,r)}^n = \begin{pmatrix} 0,0 & 1,0 & 2,0 & 3,0 & 4,0 & 5,0 & 6,0 \\ 0,1 & 1,1 & 2,1 & 3,1 & 4,1 & 5,1 & 6,1 \\ 0,2 & 1,2 & 2,2 & 3,2 & 4,2 & 5,2 & 6,2 \\ 0,3 & 1,3 & 2,3 & 3,3 & 4,3 & 5,3 & 6,3 \\ 0,4 & 1,4 & 2,4 & 3,4 & 4,4 & 5,4 & 6,4 \\ 0,5 & 1,5 & 2,5 & 3,5 & 4,5 & 5,5 & 6,5 \\ 0,6 & 1,6 & 2,6 & 3,6 & 4,6 & 5,6 & 6,6 \end{pmatrix} = \begin{pmatrix} null & null & null & 3,0 & 4,0 & 5,0 & 6,0 \\ null & null & 2,1 & 3,1 & 4,1 & 5,1 & 6,1 \\ null & 1,2 & 2,2 & 3,2 & 4,2 & 5,2 & 6,2 \\ 0,3 & 1,3 & 2,3 & 3,3 & 4,3 & 5,3 & 6,3 \\ 0,4 & 1,4 & 2,4 & 3,4 & 4,4 & 5,4 & 6,4 \\ 0,5 & 1,5 & 2,5 & 3,5 & 4,5 & null & 6,5 \\ 0,6 & 1,6 & 2,6 & 3,6 & null & null & 6,6 \end{pmatrix} \quad (16)$$

2.6 MECHANICS OF MOVEMENT OF THE TEMPLATE ARRAY

The fundamentals of rotation and translation of a *template array*, comprised of coil weights, for pattern formation are illustrated in three examples. We start with the *template array*, in its smallest form consisting of four coils forming *zone 1*. When the *template array* rotates it transfers pre-loaded coil current weights by moving from coil hex-center to coil hex-center as shown in Fig. 2.11(a) – (b) where the center hexagon of each coil is highlighted by the corresponding color of the coil. An example of a simple counterclockwise rotation (CCW) of a double pixel, along the 2nd ring, using the *zone 1 template array* is shown in Fig. 2.11 illustrates the concept.

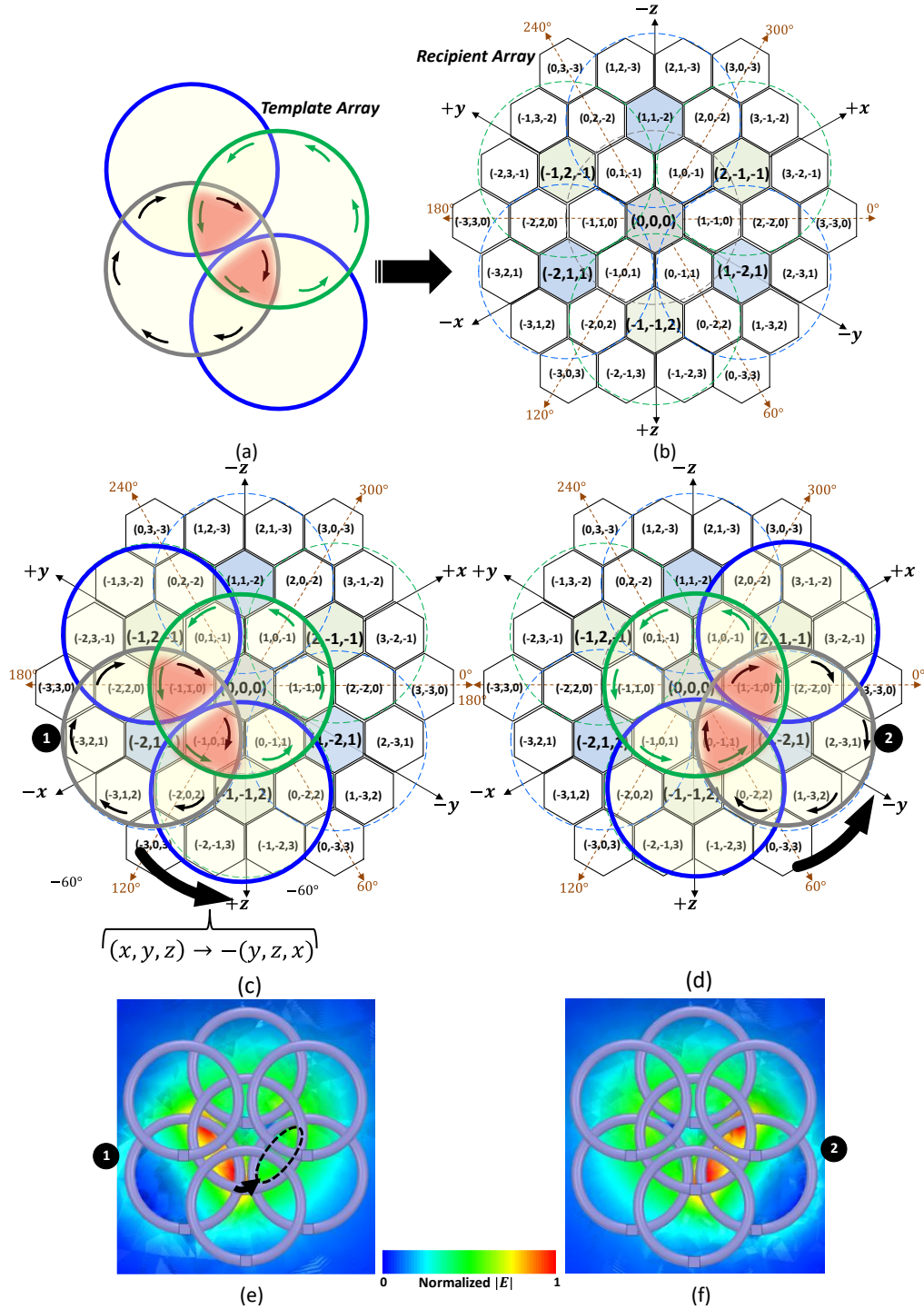


Figure 2.11: Rotation (CCW) of the pixel (2nd-ring) using the *zone 1* template array. (a) *template array* moves, aligns and transfers pre-loaded user-defined coil weights ($I_n e^{j2\pi} = 1, I_n e^{j\pi} = -1$ or 0), (b) *template array* moves and aligns with a three-ring *recipient array*, (c) position 1 alignment is established, and coil weights are transferred, (d) two 60° rotations (two hex positions) occur from position 1 to 2 followed by coil weight transfer, two hex jumps by shifting coordinates and multiplying by -1, (e) E-field simulation of Position 1 and, (f) E-field simulation of Position 2.

Initially the *template array*, pre-loaded with coil weights, moves and aligns with the *recipient array* to position 1 in Fig. 2.11(c) and the coil current weights are transferred. Then moving CCW two slots over which is equivalent to two 60° rotations (two hex slots) to position 2 in Fig. 2.11(d) followed again by the transfer of coil weights. This involves two hex jumps over and multiplying by -1 per Eqn. (9). E-field simulations in Fig. 2.11(e) – (f) show the movement of the double-pixel from position 1 to position 2.

A detailed example is given to show how the sparse arrays are generated at each step when rotating a double-pixel clockwise (CW) in Fig. 2.12. The sparse arrays are populated with the weights (+1, -1, or 0) during each step along the 2nd ring of the *template array* and *recipient array*. A supporting flow chart of this method is described in Fig. 2.15.

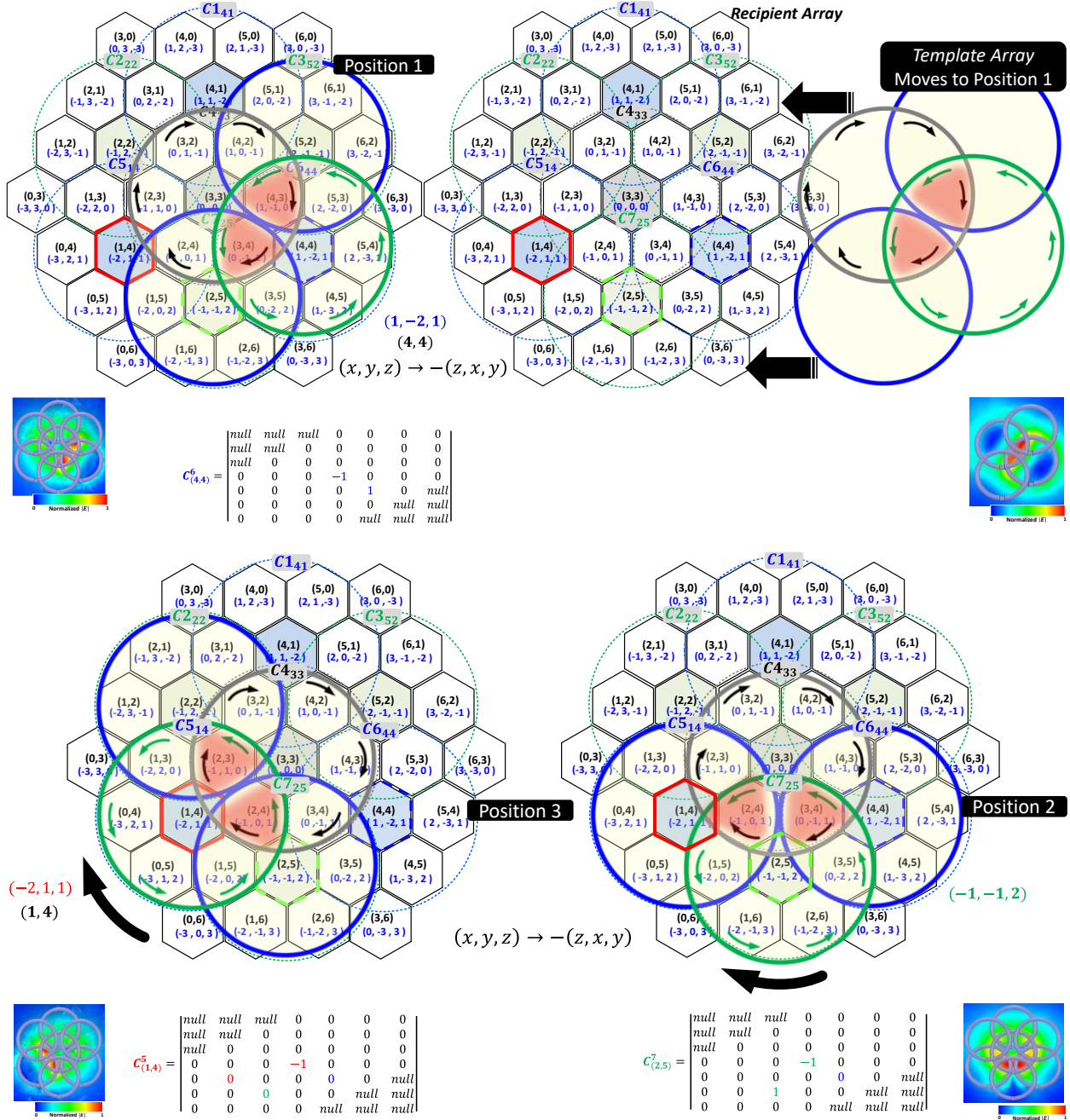


Figure 2.12: Example – generating a coil current weight matrix for CW rotation; *double-pixel* moves from positions 1 to 2 to 3 using a *zone 1* template array. The *template array* (populated) and *recipient array* (null), both in axial indexed arrays, are added together at each position to facilitate the transfer of current weights ($I_n e^{j2\pi} = 1, I_n e^{j\pi} = -1$ or 0).

An example of a simple translation of a double pixel moving one hex slot along 0° using a *zone 1 template array* is described in Fig. 2.13(a). In the same fashion, the *template array* with pre-loaded coil current weights, moves, aligns, and transfers data to the *recipient array* from position 1 to position 2.

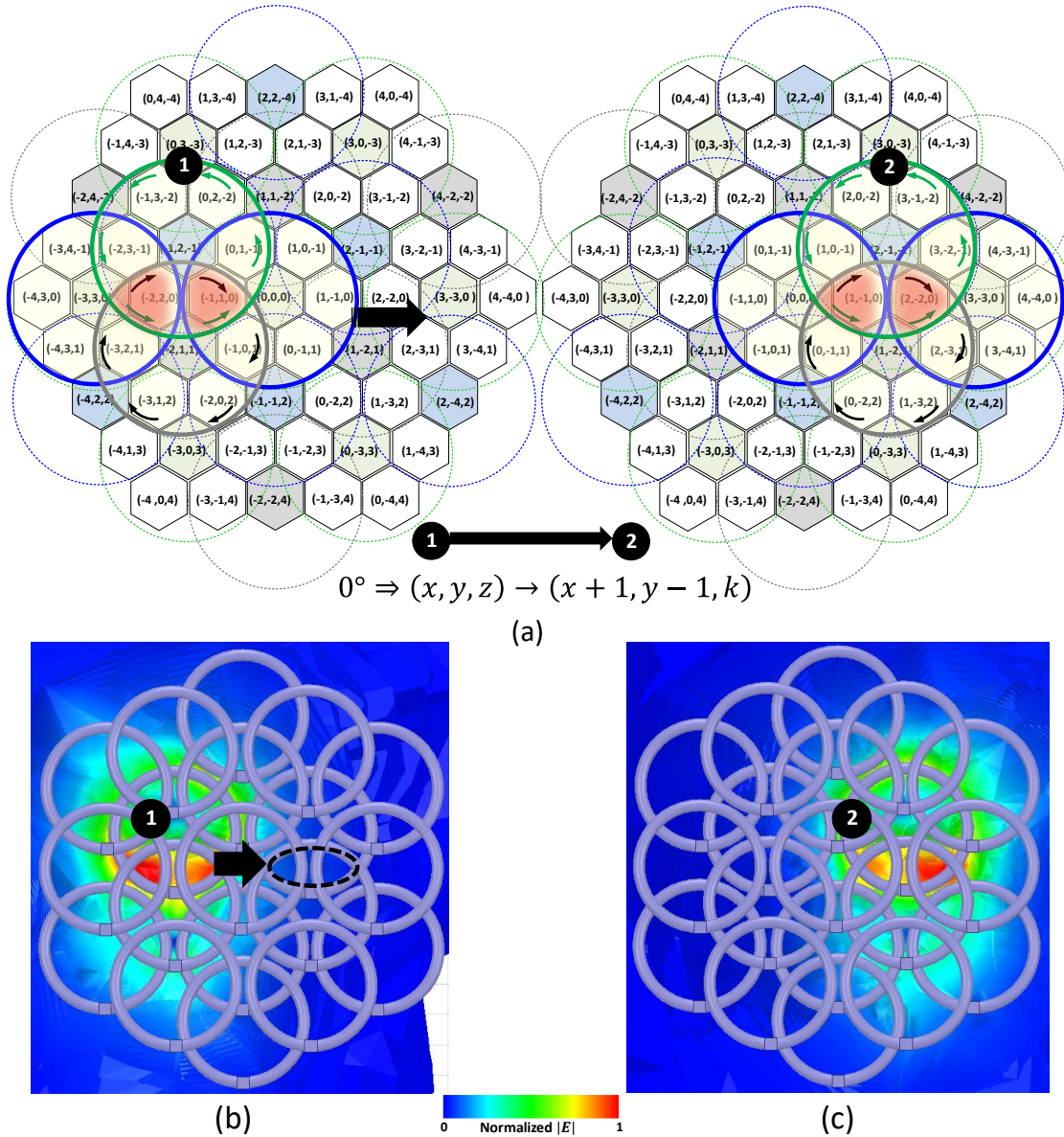


Figure 2.13: Example -Translation using the *zone 1 template array* across a 19 coil four-ring *recipient array*. (a) *template array* moves three-slots hex flat-to-flat at 0° from position 1 to position 2, (b) E-field simulation of position 1 pre-translation pixel and, (c) E-field simulation of position 2 post-translation pixel (note: $k=constant$).

To reiterate, the reference points are in each coil center and are mapped to the center cubic coordinate. The centers of each coil are highlighted by the corresponding color of the coil. In this case the translational movement of 0° is defined by Eqn. (10). E-field simulations in Fig. 2.13 (b) – (c) show the movement of the double-pixel from position 1 to position 2.

A pattern that forms a sharp bend is demonstrated using a larger *template array* (*zone 1 + 2* with 10 coils) shown in Fig. 2.14. A rotation (CW) of 60° along the hex centers of the 2nd, 3rd and 4th rings with the *template array* over an 8-ring *recipient array* is shown in Fig. 2.14(a). The rotational (CW) step of 60° shift of coordinates using Eqn. (8). In Fig. 2.14 (a) the *template array* rotates 60° from position 1 to position 2, with supporting simulations shown in Fig. 2.14 (b) - (c) on the movement of the excitation double-pixel. The simulation in Fig. 2.14 (d) shows the superposition of currents in the two sets of *template array* coil weights which reveal the emergence of a curved pattern seen in Fig. 2.14 (d).

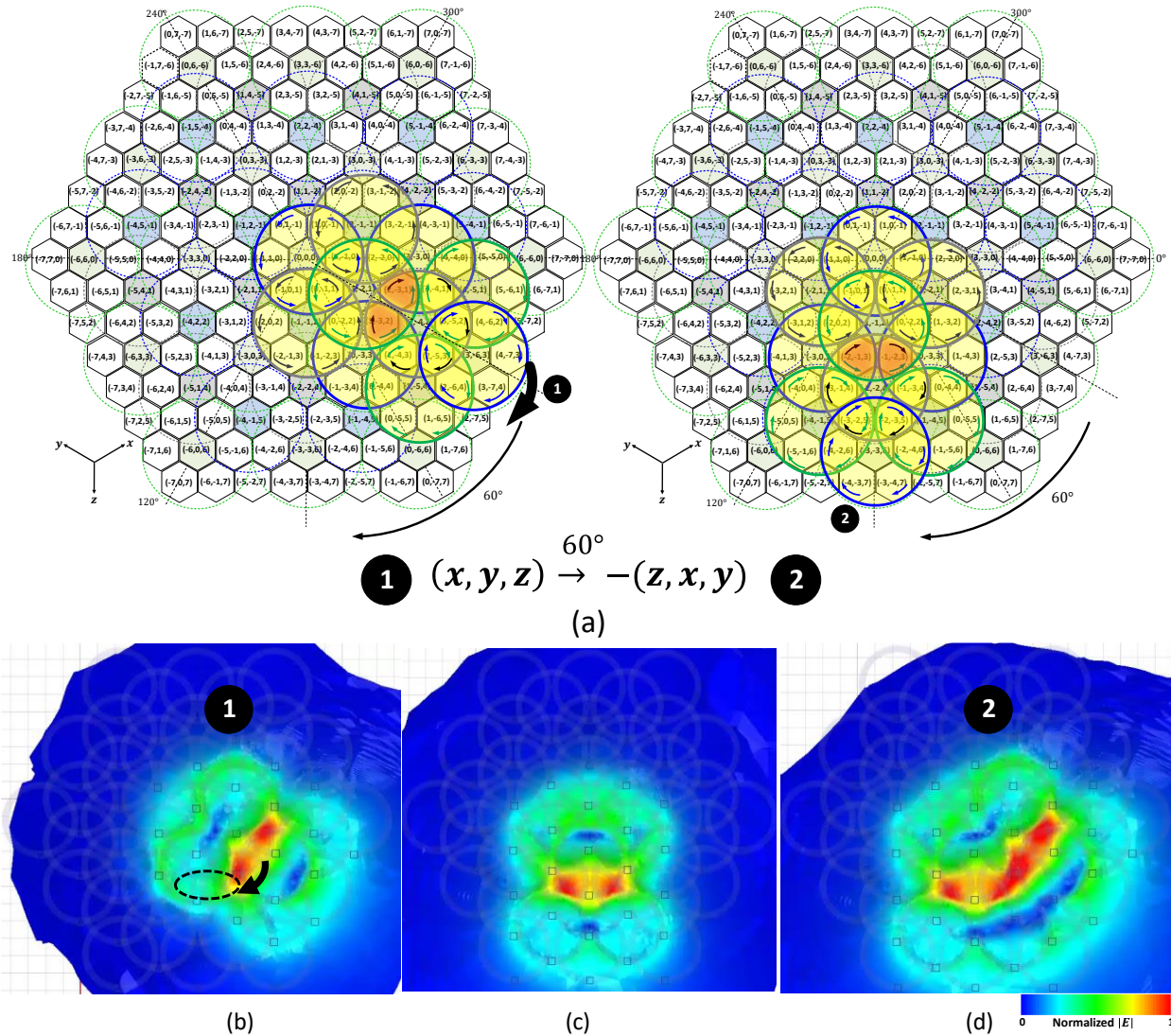


Figure 2.14: Forming a sharp bend - rotation (CW) of 60° 2nd, 3rd, and 4th rings with the *template array* (*zone 1* and *zone 2* consisting of 10 coils) over an 8-ring *recipient array*. (a) *template array* rotates 60° from position 1 to position 2; rotation (CW) of 60° via the shift of cubic coordinates and multiplying by -1, (b) simulation of position 1 of excitation pixel (excitation area in red), (c) simulation of position 2 of excitation pixel, (d) simulation shows the superposition of currents via addition of two arrays yielding a curved pattern.

Code using Python was written to move and transfer coil current weights around the grid via the virtual *template array* while indexing all three coil current weights in each of the 3-layers. Again, the method is intuitive and can be performed, without code, by using a transparency of the *template array* and simply moving it step by step over the *recipient array* to accomplish the same task. A top-level flowchart, in Fig. 2.15, outlines each major step in the code. The virtual *template*

array is populated with coil current weights from the system controller hash table and is referenced to the center hexagon of the designated reference coil ($C_{(q,r)}^n$) that is directly associated with generating excitation pixel (n is the coil number). It is aligned center to center with the *recipient array* below it and with the same cubic coordinates and axial coordinates as the *recipient array*. In the position 1, the *template array* has an array populated with coil weights, as defined in Eqn. (16), while the *recipient array* coil weights are initialized to zero. The normalized coil weights ($I_n e^{j2\pi} = 1, I_n e^{j\pi} = -1$ or 0) are transferred to the *recipient array* below which has also converted to axial coordinates with the same array indices to accept the transfer of data. This array is ported in to HFSS via post processing to ensure the pixel is excited and in the desired position. Once moved (e.g., rotated) they are converted to axial coordinates that contain the coil current weights and stored in the *recipient array*. This simple procedure was first verified using a light table with transparencies and then assessed in HFSS. This laid the foundation for the generation of Python (NumPy) code to generate the various functions for coordinate conversion, movement, data storage and excitation source profiles that could be directly ported into HFSS. The *template array* providing each coil current weight to the *recipient array* in HFSS allows for a review and check of the excitation before proceeding. Since this is a post simulation process function, only one analysis is required in HFSS. Therefore, each appended data set can be uploaded into the source excitation profile in HFSS providing a timely update of E-field and current density vector contours as the pattern is created. The system controller has all the pattern data stored in memory (in hash tables) thus after the *template array* movement is completed and coil current weights are stored the patterns can be applied instantaneously either sequentially or simultaneously as required.

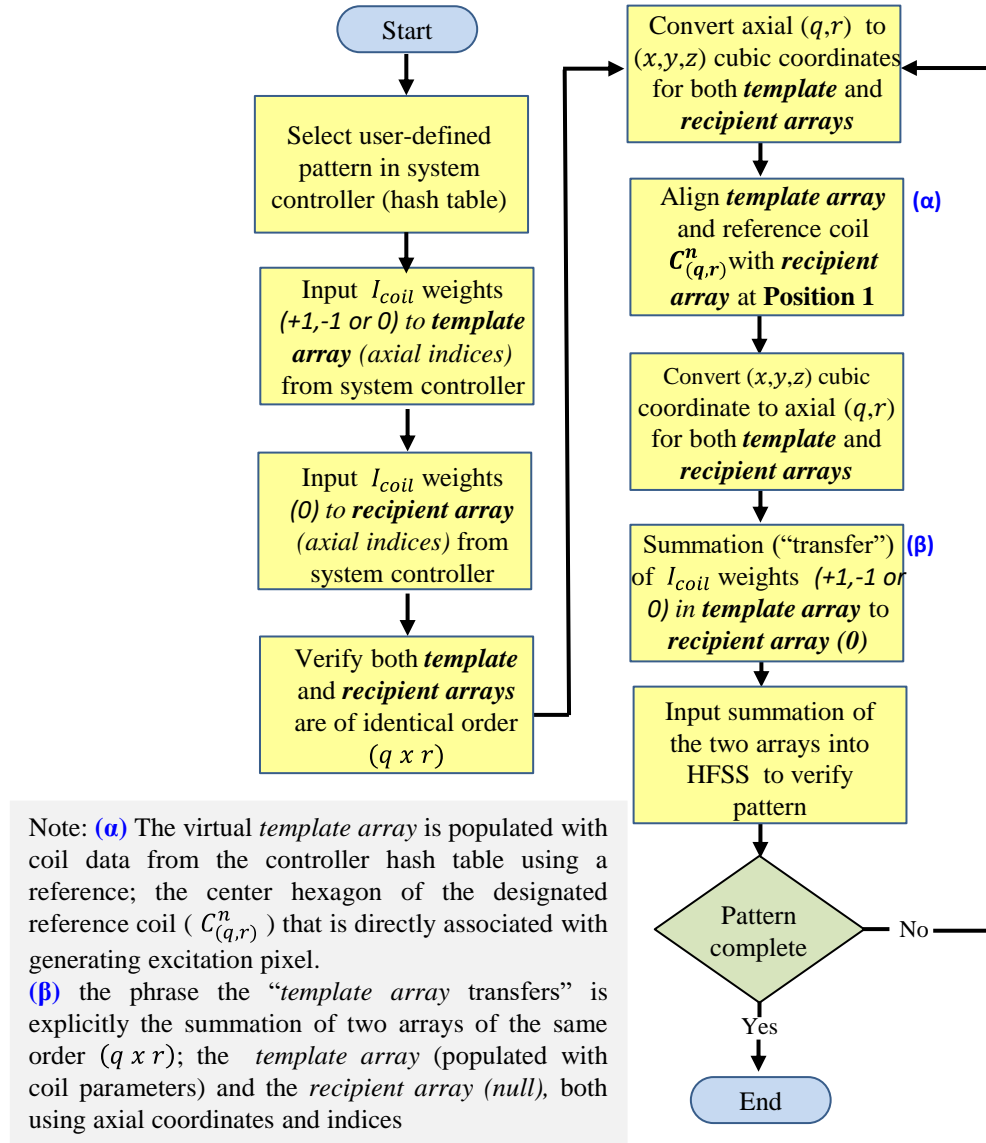


Figure 2.15: Top level pattern synthesis flow chart using Python.

This chapter is based on Matthew C. Smith and Daniel F. Sievenpiper, “A New Synthesis Method for Complex Electric Field Patterning using a Multichannel Dense Array System with Applications in Low-Intensity Noninvasive Neuromodulation”, *Bioelectromagnetics*, vol. n, no. 2022, pp. (14 pages), *In editorial review*. The dissertation author was the primary investigator and author of this paper.

CHAPTER 3 SIMULATIONS AND EXPERIMENTAL RESULTS

3.1 TRADITIONAL PATTERNS COMPARED TO THE PIXEL CELL

The multifunction capabilities of our array are first demonstrated, and the measurement technique is validated in Fig. 3.1 by simulating and measuring the patterns of the traditional systems for both circular and figure-8 coil topologies to the *pixel cell*. The induced E-field measurements and simulations of the traditional patterns shown in Fig. 3.1 (a)-(c) and Fig. 3.1 (e)-(f) are in good agreement with the patterns seen in the literature [Deng et al, 2013]. This also baselines and validates our measurement and simulation approach.

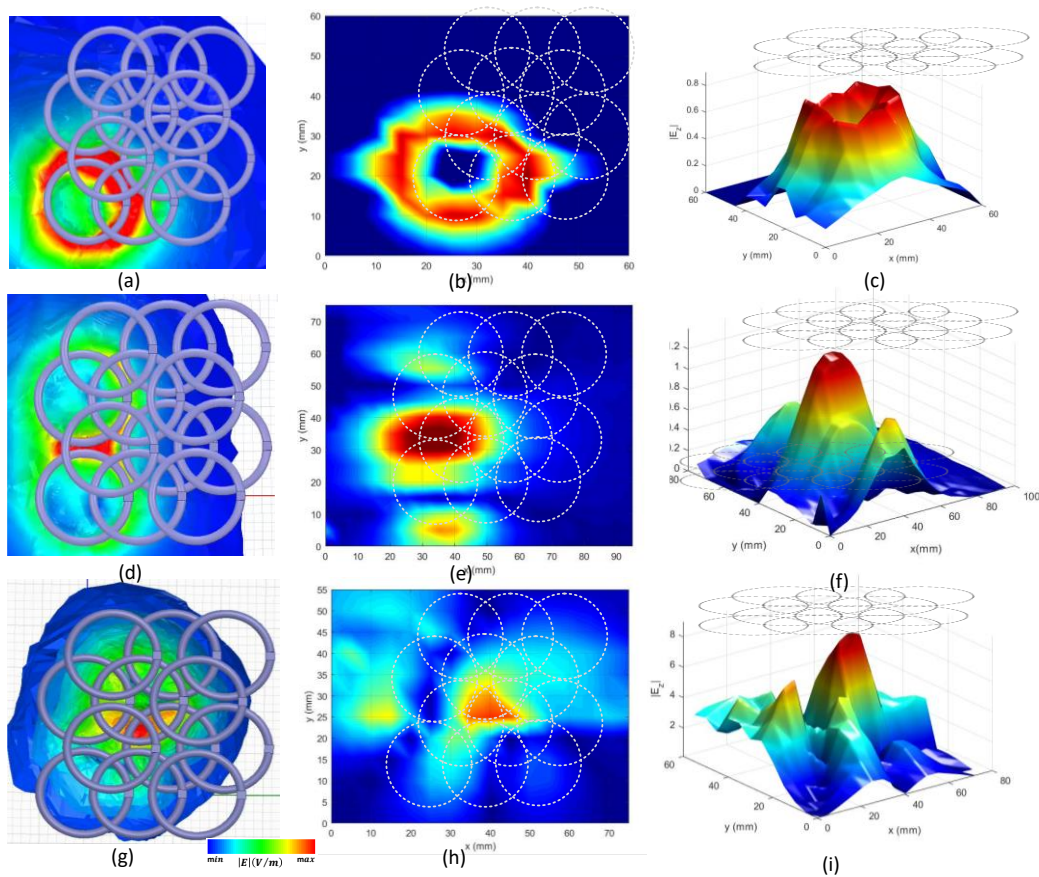


Figure 3.1: Validation of HFSS simulation at 350kHz vs. measurements by comparison using traditional E-field patterns in the literature. (a) simulation of single circular coil, (b) – (c) measurement of circular field pattern, (d) simulation of figure-8, (e) – (f) measurement of figure-8 E-field pattern, (g) simulation of a single pixel E-field pattern, (g)-(h) simulation of a single pixel.

A radial E-field scan measurement of a selected pixel, in a 12-coil array, is compared with two different figure-8 topologies under the identical conditions in Fig. 3.2. Notably the E-field focal areas are very similar. The measured E-field spread on the radial x-axis, of all three excitation patterns in Fig. 3.2 at the $|E_{max}|/2$ were approximately equal at 20mm.

One excitation lobe of the pixel is slightly elevated on the left side and lower on the right side since the entire array is energized in this specific case. As will be shown later in Section 8.2, adjusting charging voltages on each relevant coil, can be employed for optimization of various patterns.

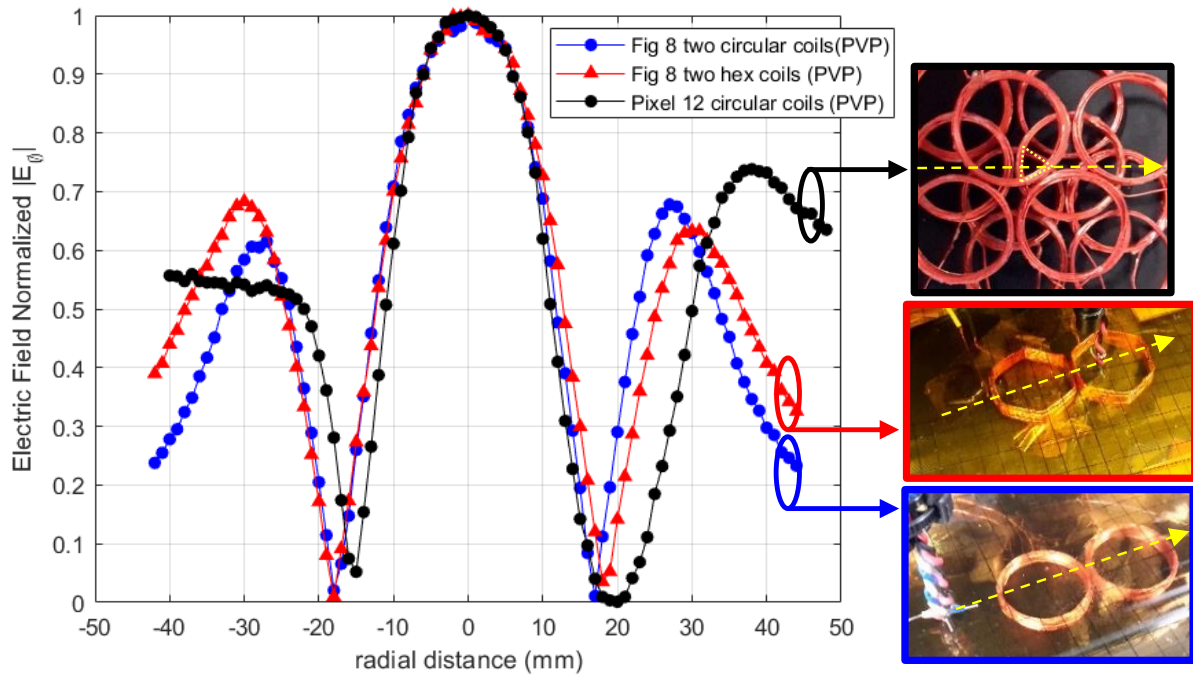


Figure 3.2: Radial near field scan of the E-field comparing three different coil topologies; a figure-8 with circular coils, a figure-8 with hexagonal coils and a single pixel in a 12-coil array (note: yellow line shows trajectory of near field probe).

3.2 COMPLEX USER-DEFINED E-FIELD PATTERNS - SIMULATIONS

The methods, previously discussed, by which the *template array* travels over the *recipient array* were first verified using a light table with transparencies and then assessed in HFSS. This laid the foundation for the generation of Python (NumPy) code [Harris et al, 2021] to generate the various functions for coordinate conversion, movement, data storage and excitation source profiles that could be directly ported into HFSS21R1. The *template array* providing each coil's current weights to the *recipient array* in HFSS allows for a review and check of the excitation before proceeding. Since this is a post simulation process function, only one analysis is required in HFSS. Therefore, each appended data set can be uploaded into the source excitation profile in HFSS providing a timely update of E-field and current density vector contours as the pattern is created. The system controller has all the pattern data stored in memory (in hash tables) thus after the *template array* movement is completed and coil current weights are stored the patterns can be applied instantaneously for sequentially or simultaneous excitation.

A series of simulations and experimental results are now discussed with the goal of validating the procedure described earlier. We begin by synthesizing a circular pattern in Fig. 3.3. using a *template array* (*zone 1 + 2*) transferring data to a 19-coil *recipient array*. This circular pattern offers the capability of electronically changing the effective diameter of a coil and subsequent excitation pattern which could potentially offer rapid switching of spatiotemporal reconfigurable depths of penetration. Notably, the capability of electronically changing the diameter of a circular pattern in Fig. 3.3 shows that the reconfigurable diameter of a circular pattern when increased can increase the depth of penetration. Thus, offering a unique variable that allows the user to rapidly reconfigure depth of penetration for spatiotemporal optimization and perhaps alternate the modality with others at different sites and depths with fast switching. This modality

would be very hard to implement in today’s single function systems. The author’s report on this topic in a previous paper [Smith et al, 2021].

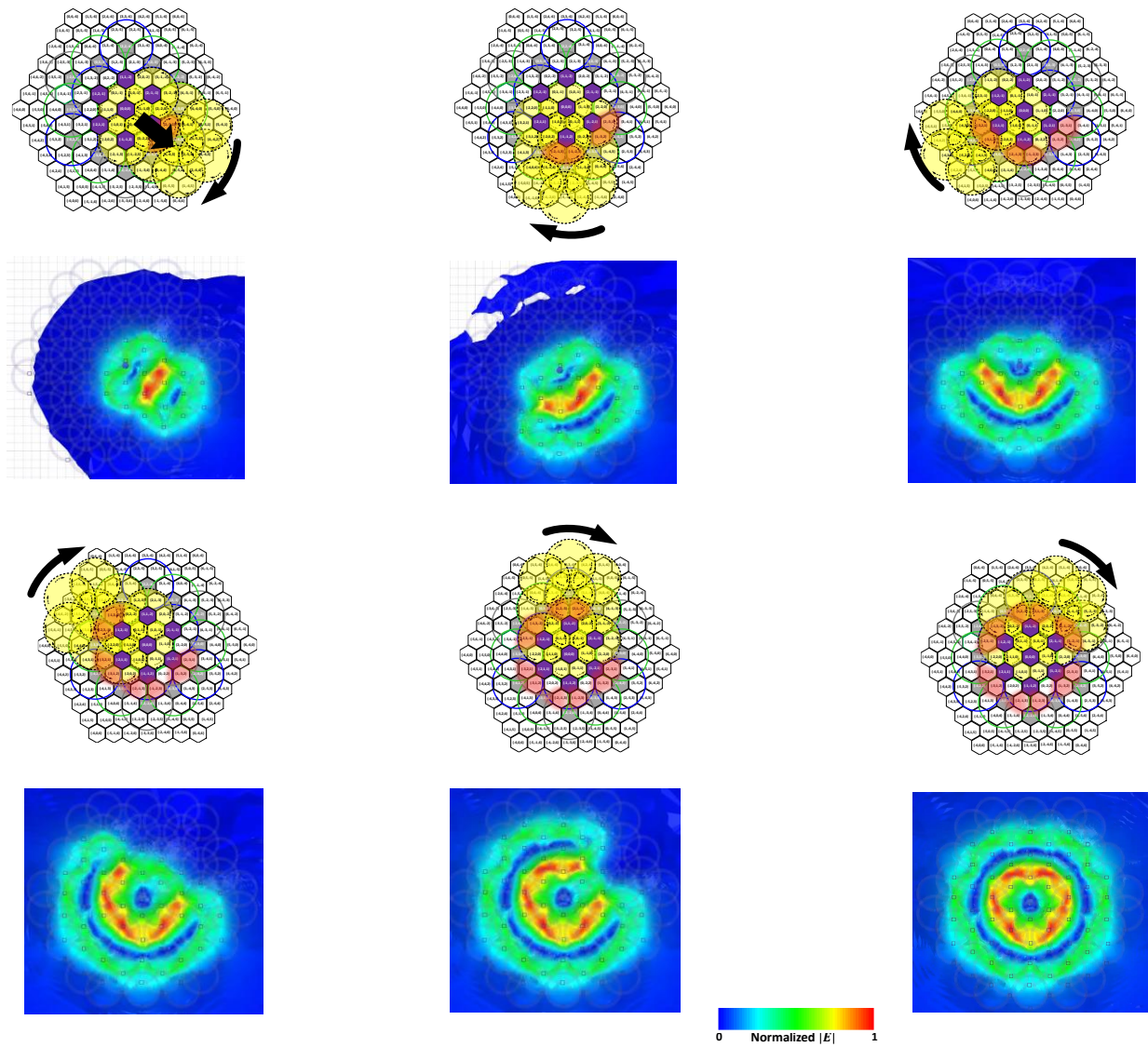


Figure 3.3: Synthesis of a circular pattern - Movement of a double - pixel (one translation step and multiple rotations) to form a reconfigurable circular pattern. (a) illustration of the sequence of pixels generated, rotated, and transferred by the *template array* to the *recipient array* to construct a circular pattern, (b) simulation of the sequence.

Another interesting capability, demonstrated in Fig. 3.4, is the formation of complex user-defined patterns (e.g., zig - zag). This potentially could be of great utility. For example, when

coupled with neuro-navigation it could provide geometrically optimal angles of excitation trajectory (e.g., orthogonal to a sulcus) in the brain as it pertains to the unique characteristics of each patient [Jansen et al, 2015].

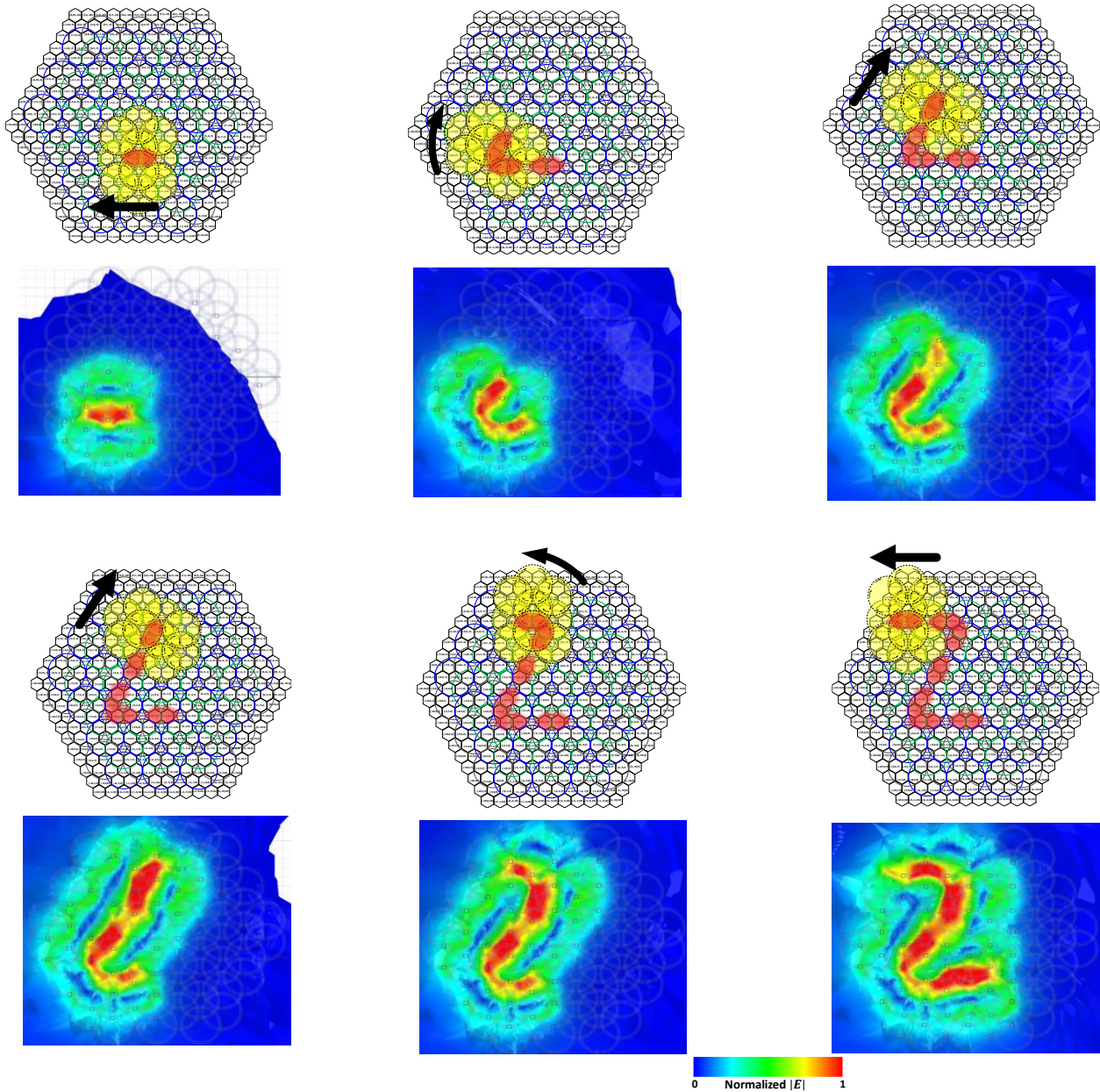


Figure 3.4: Synthesis of a zig-zag pattern - movement of a double-pixel (one translation step and multiple rotations) to form a zig-zag pattern. (a) illustration of the sequence of pixels generated, rotated, and transferred by the *template array* to the *recipient array* and, (b) simulation of the sequence.

A summary of patterns using our synthesis method pattern, in Fig. 3.5, demonstrates the broad categories of user-defined patterns that can be synthesized using the techniques described in this paper. The multi-locus and multi-site patterns in Fig. 3.5(a) have the potential to assist the researcher in brain connectivity studies which to date have been hampered by slow manual or robotic movement of one or two heavy stimulator coils [Reti, 2015].

Fig. 3.5(b) shows the arbitrary nature of a zig-zag pattern indicating that many different geometrically optimal angles of trajectory of excitation across a sulcus boundary at the appropriate angle are possible [Janssen et al, 2015]. The circular pattern shows that the reconfigurable diameter of a circular pattern, examined in our previous work [Smith et al, 2021], can be increased for increased depth of penetration in cortical tissue or modulated rapidly to alternate depths or sites. Sharp bends of the pattern, Fig. 3.5 (d) can be accommodated to adjust to the complex trajectories across a specific boundary of sulci in the brain unique to each patient. Unilinear patterns with the ability to form at any angle of trajectory are shown in Fig. 3.5 (e) - (f). In all these cases, the induced E-fields and current vectors of the patterns can be rapidly modified, reshaped and redirected with any number of spatiotemporal variations.

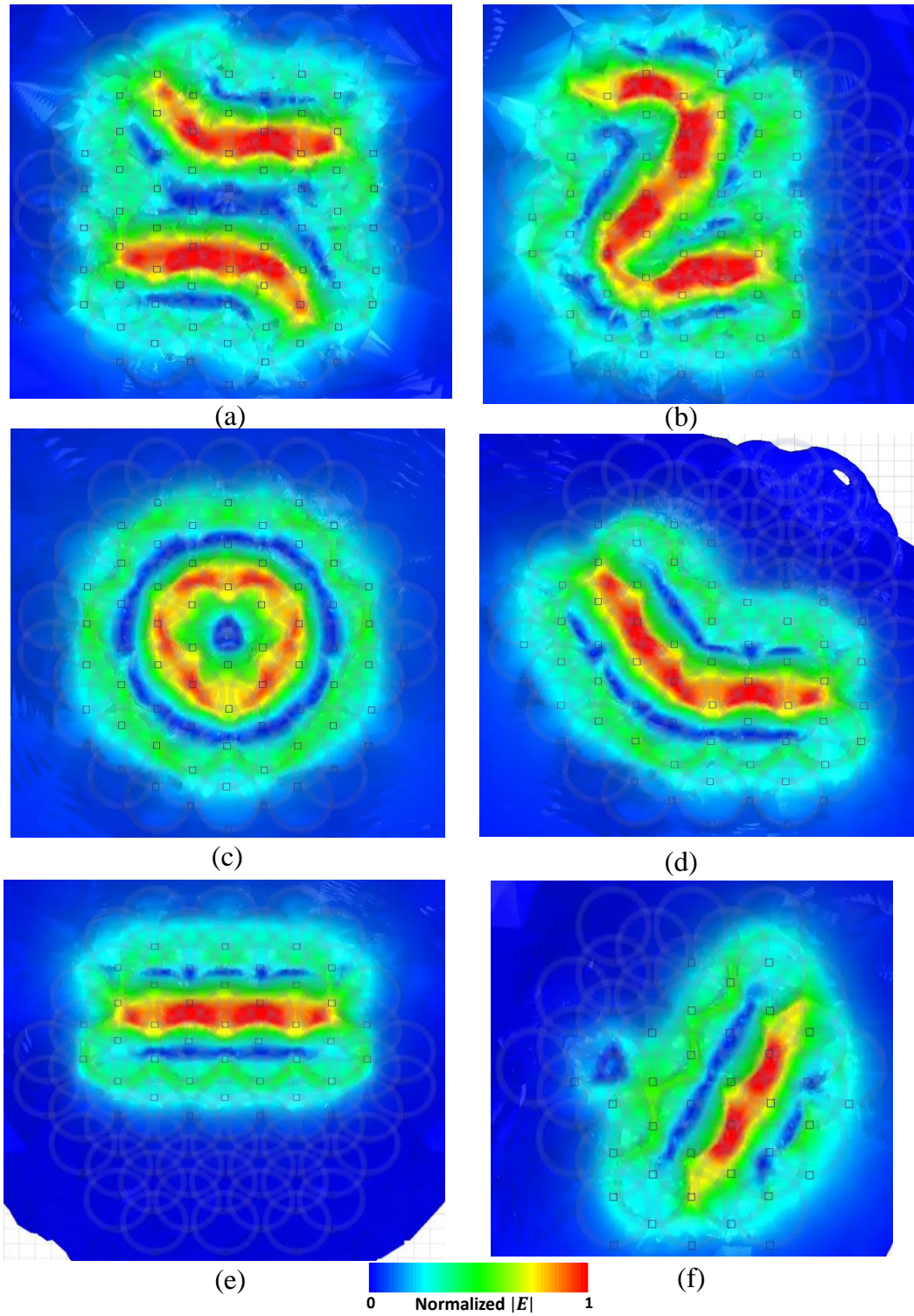


Figure 3.5: Summary of user-defined synthesized patterns. (a) multi-site/multi-loci, (b) zig – zag pattern, (c) circular for reconfigurable depth of penetration, (d) 45° bend, (e) horizontal unilinear and (f) diagonal unilinear.

3.3 MEASUREMENTS VS. SIMULATIONS OF COMPLEX PATTERNS

A series of measurements vs. simulations for five different rudimentary patterns are presented and discussed in Fig. 3.6. The goal being to validate the procedure experimentally. Measured vs. simulated show fair agreement in demonstrating the general shape of the synthesized contours in Fig. 3.6. We begin by measuring a single double-pixel pattern in Fig. 3.6 (a) using a *zone 1 template array* followed by an “omega” shaped pattern in Fig. 3.6 (b) using three double-pixels. A multi-site pattern follows with each excitation consisting of a double – pixel in a 13-coil array. Using two-pixels per pattern and a *zone 1+2 template array* a unilinear and a curved pattern formed by two pixels in Fig. 3.6 (d) and 3.6 (e).

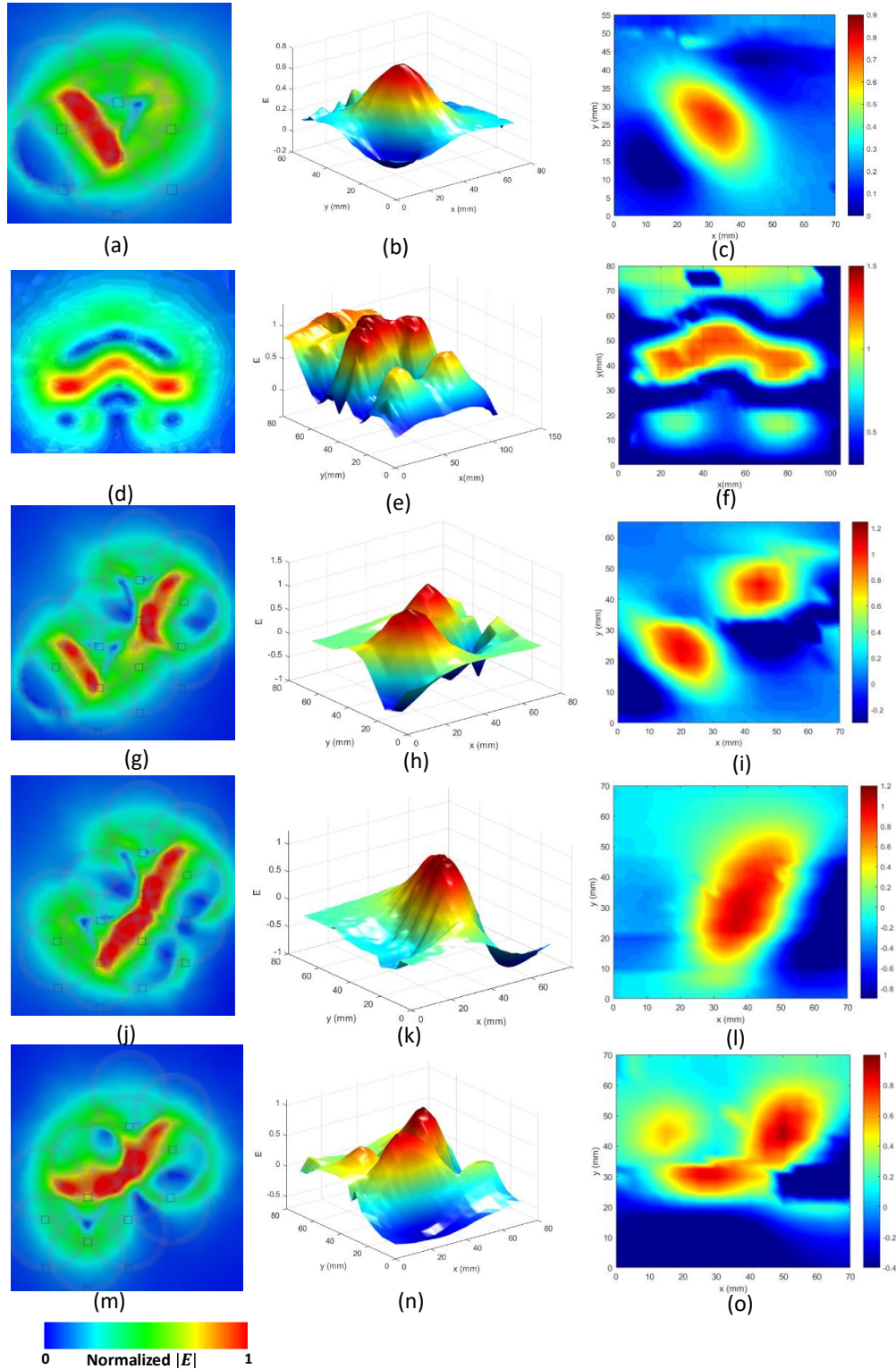


Figure 3.6: Simulations (left side) vs. measurements (center and right side) of arbitrary E-field patterns. (a)-(c) single double-pixel in 7-coil array, (d)-(f) "omega" pattern in a 13-coil array using three single double pixels (g)-(i) two multi-site in a 13-coil array (two double-pixels), (j)-(l) unilinear pattern diagonal pattern in a 13-coil array and (m)-(o) curved pattern; superposition of two double-pixels in a 13-coil array.

3.4 SIMULATIONS | BRAIN MODEL

Different tissue types and the varying fiber orientation in the brain tissue results in an inhomogeneous and anisotropic conductivity distribution and distorts the induced E-field in a non-trivial way [Thielscher et al, 2011; Optiz et al, 2011]. This is demonstrated in the simulation in Fig. 3.7 in which an identical unilinear E-field pattern is compared in an ideal homogenous solution vs. a brain model using a planar 3-layer array [Ansys HFSSR21, finite element simulation software, and Human Body Model V3].

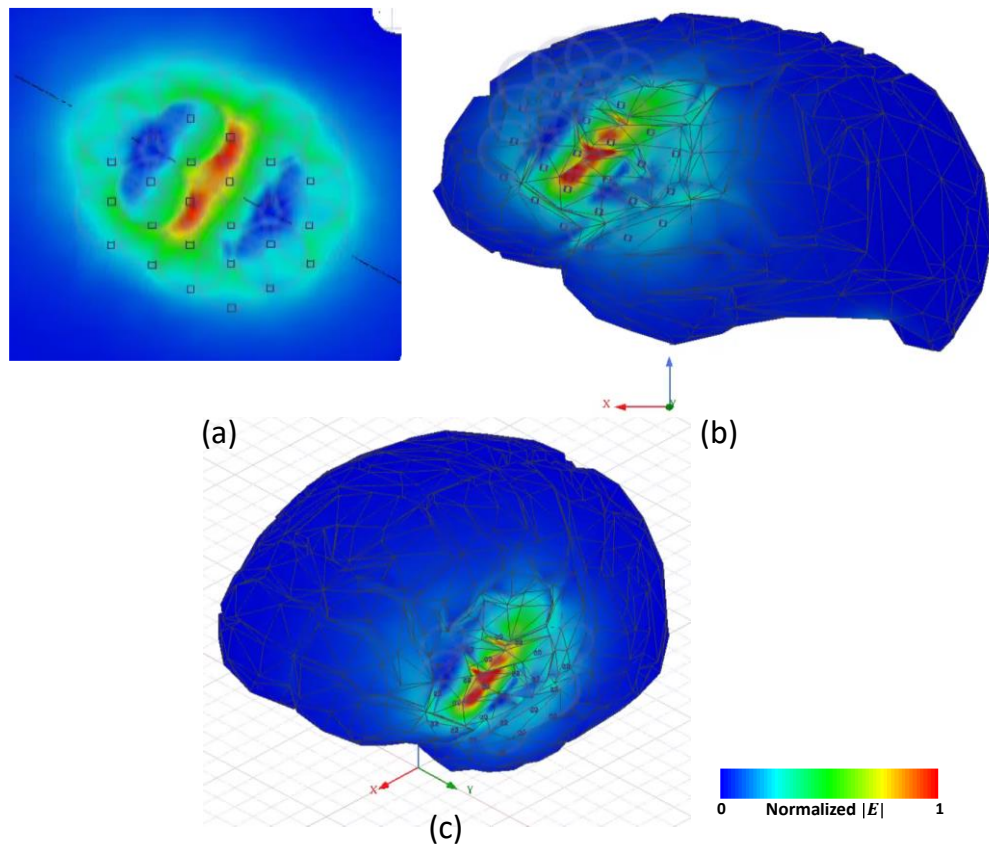


Figure 3.7: Comparison of an induced unilinear E-field pattern in homogenous conductive solution vs. brain model. (a) homogeneous conductive solution (b) same pattern using the HFSS human head model V3 (c) isometric view of the same of (b).

Although this work consists only of planar 3-layer arrays an illustration in Fig. 3.8 shows similar levels of distortion of the unilinear E-field pattern when using a conformal 3-layer array with larger diameter (40mm) coils. It is too early to postulate without further investigation, but this suggests that conformal arrays may not be the optimal solution over that of planar arrays.

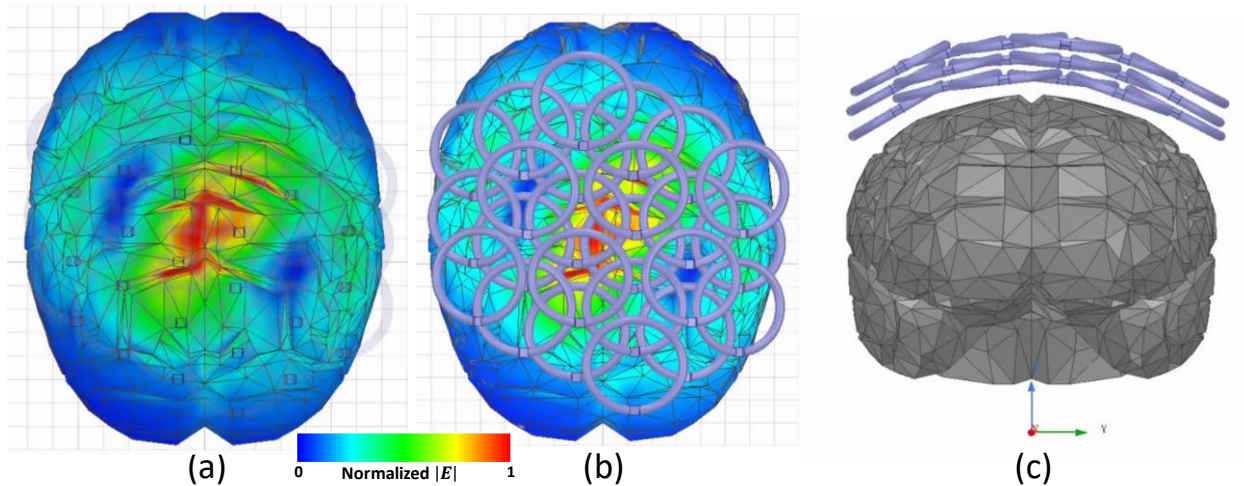


Figure 3.8: Unilinear pattern generated by a conformal array using a realistic brain model

This chapter is based on Matthew C. Smith and Daniel F. Sievenpiper, “A New Synthesis Method for Complex Electric Field Patterning using a Multichannel Dense Array System with Applications in Low-Intensity Noninvasive Neuromodulation”, *Bioelectromagnetics*, vol. n, no. 2022, pp. (14 pages), *In editorial review*. The dissertation author was the primary investigator and author of this paper.

CHAPTER 4 RECONFIGURABLE DEPTH OF PENETRATION

4.1 INTRODUCTION

The depth of penetration of the magnetic field can be reconfigured by varying current magnitude and phase of the smaller coil diameters in the array to achieve the same decay profile performance of a larger diameter coil as illustrated in the concept graphic in Fig. 4.1. Only simulations exist in the literature to date, to the best of our knowledge, we report the first measurements of hexagonal shaped coils in multi-coil arrays have increased depth of penetration over circular shaped coil-based arrays. This chapter focuses on the measurements and simulations on controllable depth of penetration with circular and hexagonal shape coils in various multi-coil array topologies. Similar multi-coil arrays have been simulated in the literature using circular coils [Yang et al, 2010; Wei et al, 2017; Ho et al, 2009]. However, to the best of our knowledge, we are the first to measure the synthesized depth of penetration using a multi-coil dense array system. Moreover, this is the first study involving the measurement of depth of penetration for hexagonal coils in dense arrays.

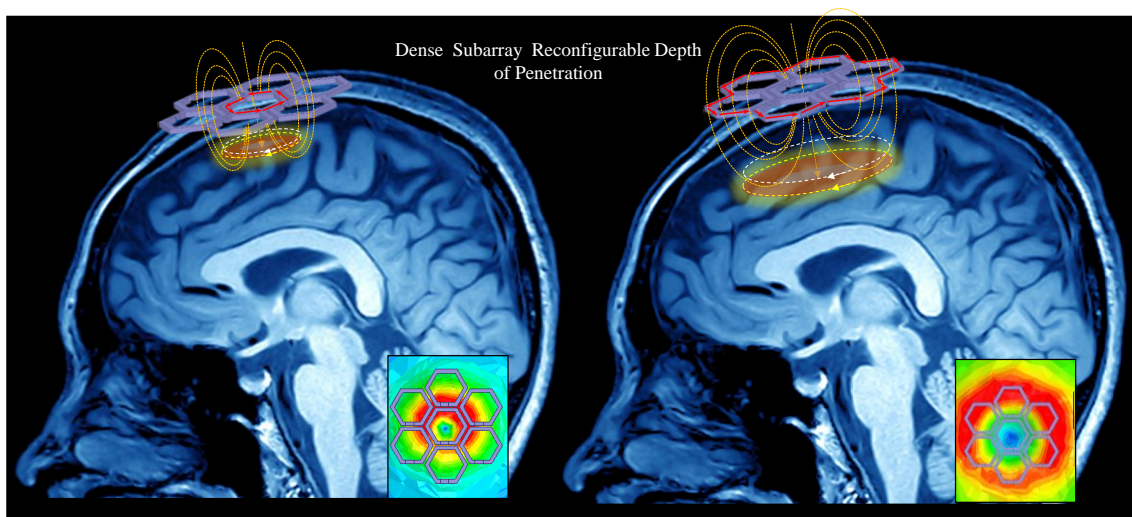


Figure 4.1: General concept of reconfigurable depth of penetration illustrated using FEM and notional brain image flow patterns on the center coils in seven-coil planar arrays (hexagonal coils).

4.2 PRINCIPLES OF OPERATION

The function of a stimulation coil whether singular, multiple or in array topologies, is to spatially distribute the magnetic field and in turn spatially distribute the induced electric field and the current flow in the brain. Therefore, the amplitude of the induced electric field depends on magnetic field amplitude, how fast it changes over time and its direction [Grehl et al,2016; Esselle et al, 1992].

The stimulation coil stores energy from the time-varying magnetic field when the pulsed current (I_{peak}) runs through it according to the Biot-Savart law [Cheng, 1993] in the expression

$$d\vec{B} = \frac{\mu_o I d\vec{L} \times \vec{r}}{4\pi R^2} = \frac{\mu_o I d\vec{L} \sin(\theta)}{4\pi R^2} \quad (1)$$

Symmetry is used around a circular current loop at a distance z from the center to the targeted neurons simplifies from an angle at 90° , which results in a viable approximation for the B-field or magnetic flux density \vec{B} at a distance z from the center of the coil expressed as

$$\vec{B}_z = \frac{\mu_o 2\pi N I R^2}{4\pi(z^2 + R^2)^{3/2}} \hat{z} \quad (2)$$

This expression for the depth of penetration is evaluated between two different diameter coils in Fig. 4.2. The larger coil (75 mm) results in deeper penetration and more gradual decay than the smaller diameter coil (24 mm).

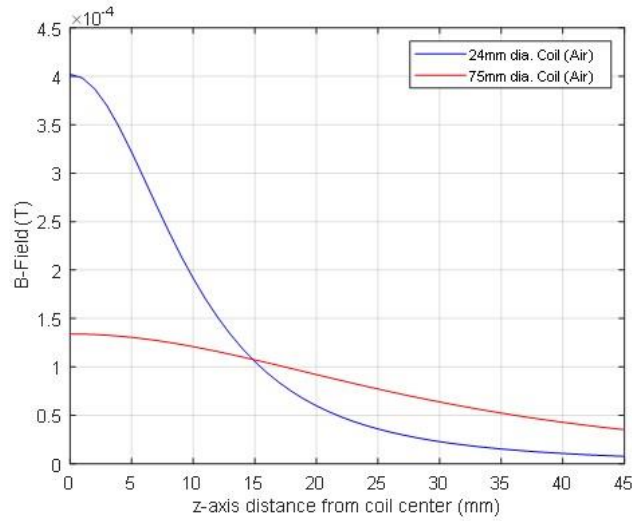


Figure 4.2: Comparison of a small vs. large diameter coil for current carrying coils (e.g., $I = 8A$, # turns = 16 for 24 mm and 9 turns for 75 mm).

A seven-coil subarray residing on the bottom layer of our multi-coil array was used to demonstrate the controllable penetration depth function of the array. This is accomplished by exciting a set of coils that behave as a single larger coil, which results in increased penetration depth. This is illustrated in Fig. 4.3 (a) and (b) with our planar seven coil arrays constructed from circular and hexagonal coils. When the individual coils in the array are energized with equal magnitude currents and phases the result is the concentric cancellation of current on the inner perimeters of the array. Finite element models (FEM) [Ansys HFSS 21R1] confirm that the opposing current phases cancel in Fig. 4.3 (c) and (d).

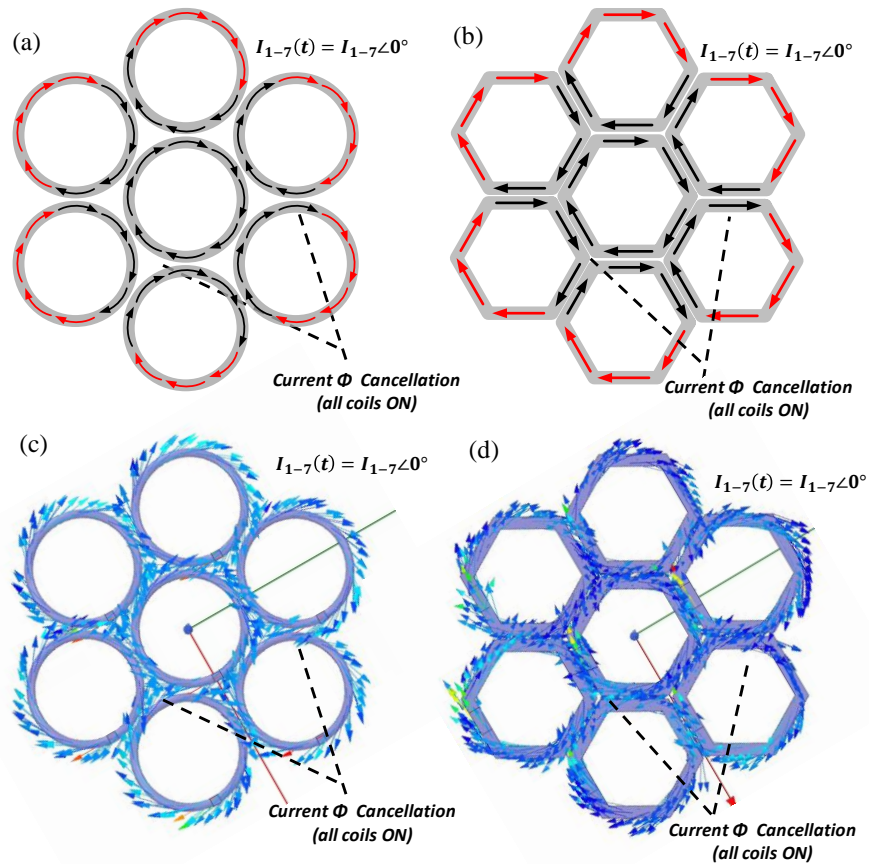


Figure 4.3: Concentric current phase cancellation flow patterns on the center coils in seven-coil planar arrays. (a) illustration - circular coils, (b) illustration - hexagonal coils, (c) FEM - circular coils and (d) FEM - hexagonal coils.

A comparison of decay profiles for the seven-coil array is shown under two conditions; when center coil is the only coil energized, in Fig. 4.4(a), and when all the coils are being energized, Fig. 4.4(b), resulting in increased penetration depth like that of a larger diameter coil but at the expense of degraded focality.

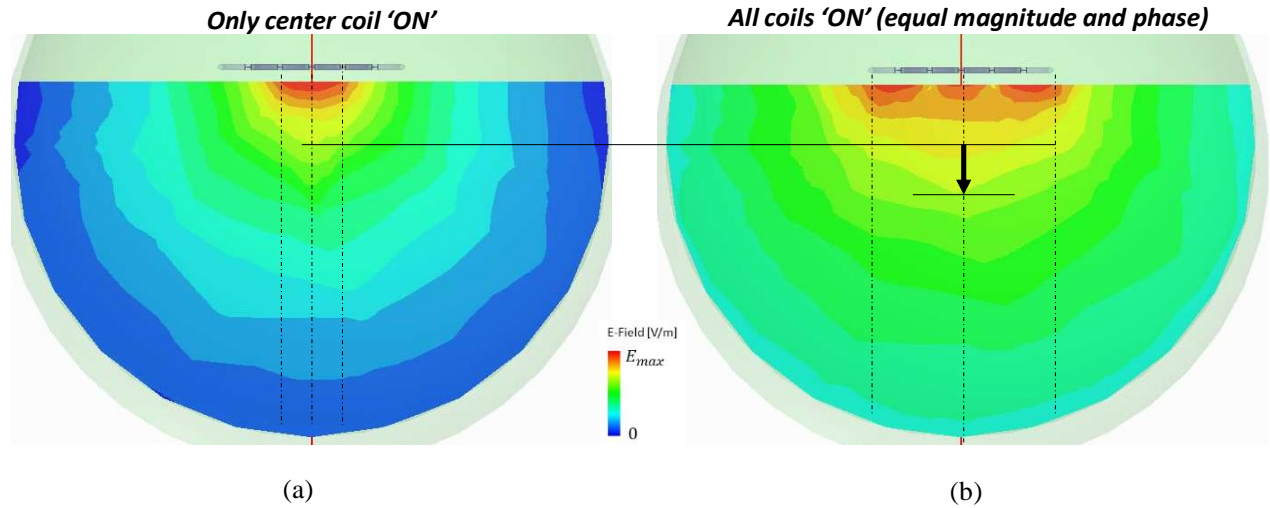


Figure 4.4: Simulation E-field decay profile in x-z plane of a seven-coil planar array composed of smaller coils synthesizing the decay profile of larger diameter coil. (a) center coil ‘ON’ only, (b) all coils ‘ON’ depth of penetration improves in x-z plane with degraded focality.

4.3 EXPERIMENTAL RESULTS AND SIMULATIONS

The widely used circular and figure-8 coil topologies were used as a baseline. The B-field measurements shown in Fig. 4.5(c)-(f) are in good agreement with the FEM simulations in Fig. 4.5(a)-(b) and the patterns seen in the literature [Reti, 2015; Deng et al, 2013]. Thus, validating our measurement approach.

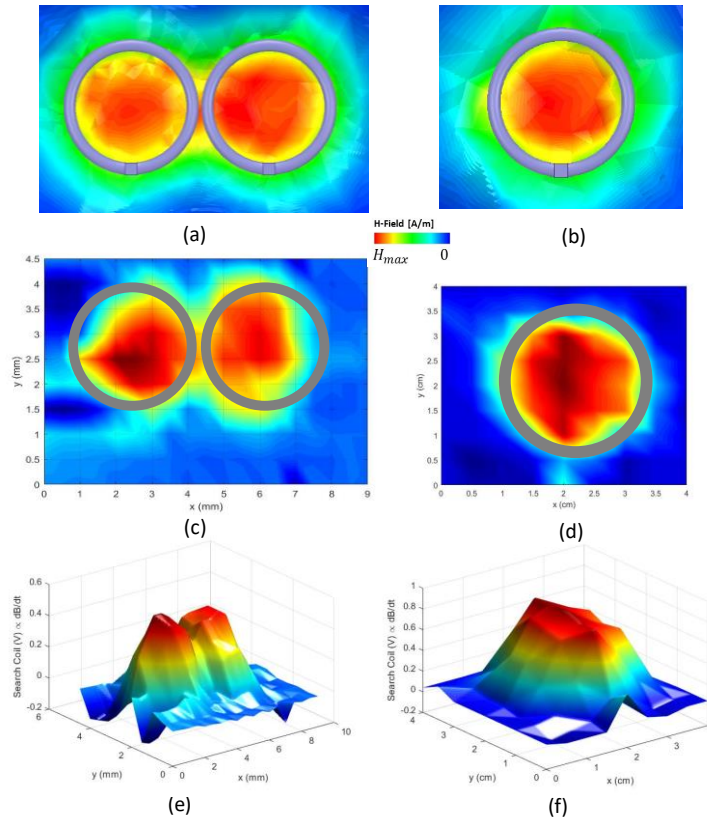


Figure 4.5: Baseline B-field measurements validated with FEM. (a) FEM figure-8 with opposing current phase, (b) FEM circular, (c), measured figure-8 with opposing current phase, (d) measured circular, (e) measured figure-8 identical current phase, (f) measured circular.

The amplitude of the induced electric field depends on magnetic field amplitude, how fast it changes over time and its direction (axial components). In terms of spatial distribution, the magnetic field that is generated by the current in the stimulation coil is almost independent from the specific head anatomy, whereas the induced electric fields in the biological media are not [Grehl et al, 2016; Esselle et al, 1992]. Considering this fact, our focus in this paper examines the characteristics of the B-field and its attenuation with various coil topologies.

The B-field decays as a function of distance and time but is not significantly attenuated by tissue-equivalent solutions. As such, the B-field allows a closer performance look at the coils in a controlled manner. This was verified by conducting a series of baseline measurements in air and

1% saline (16mS/cm) which was deemed satisfactory for our B-field measurements. As expected, Fig. 4.6 shows that air is a good approximation of a physiological conducting solution specifically for magnetic fields. Therefore, in terms of spatial distribution, the magnetic field is almost independent from the specific head anatomy [Wasserman et al, 2008; Deng et al, 2013]. When E-fields are measured a tissue-equivalent solution of salt and polyvinylpyrrolidone solution or salt and propanediol can be used [Ianniello et al, 2018].

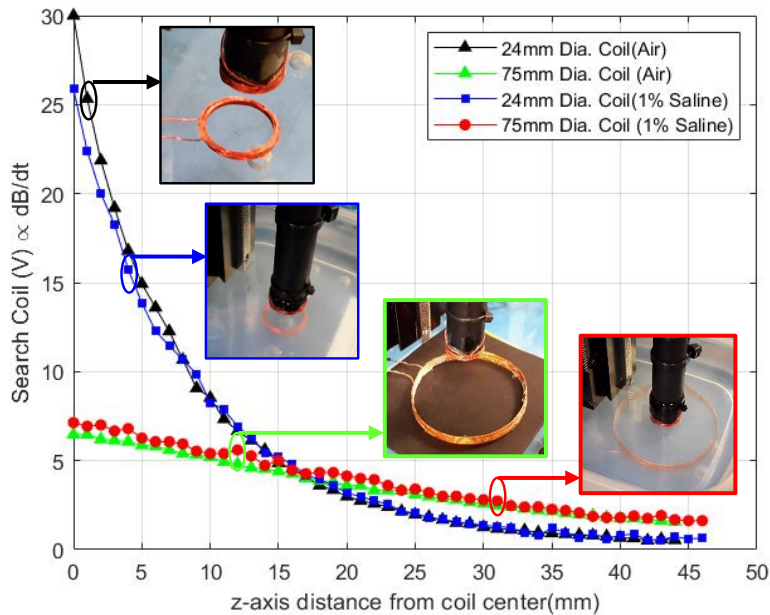


Figure 4.6: Comparison of B-field decay profiles in air and 1% saline for 24mm diameter vs. 75mm diameter coils; validating that air is a good approximation for physiological conducting solutions (1% saline).

With our multi-layer array approach, we can achieve controllable penetration depth by exciting a set of coils that behave as a single larger coil. Without control over return currents, this would normally result in a loop of current surrounding an inner loop of counter-propagating current, (like a torus) with no improvement in penetration depth.

Baseline B-field measurements with the near-field scanner of the planar seven coil array is shown in Fig. 4.7. All coils have equal current magnitudes and phases. FEM simulations are in good agreement with the measurement.

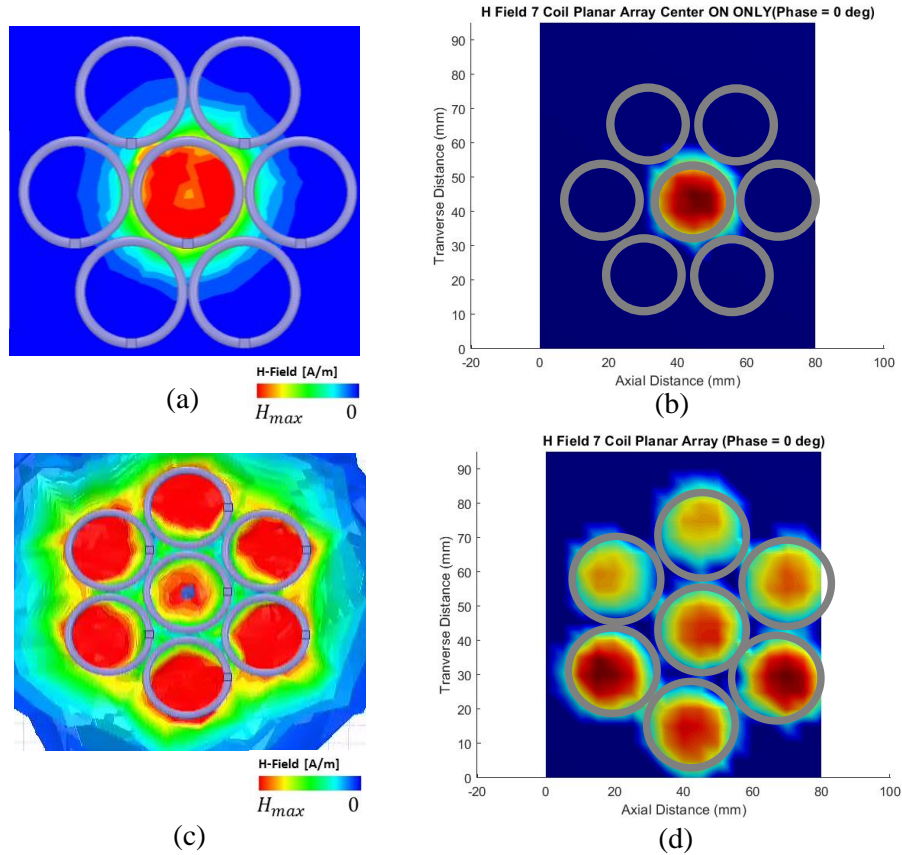


Figure 4.7: Contour plots - Seven-coil planar array B-field measurements and FEM. (a) FEM - center coil ON only, (b) measured - center coil ON only, (c) FEM - all coils ON, (d) measured - all coils ON.

The plots in Fig. 4.8 (circular coils) and Fig. 4.9 (hexagonal coils) validate the synthesized increase in equivalent diameter and the resulting increase in depth of penetration for seven-coil planar arrays when all seven coils are excited with equal current magnitude and phase. For the basis of equal comparison for each seven-coil array case, every individual coil (circular or hex) was energized and monitored to have identical voltages and currents (24V and 8A) throughout each measurement session.

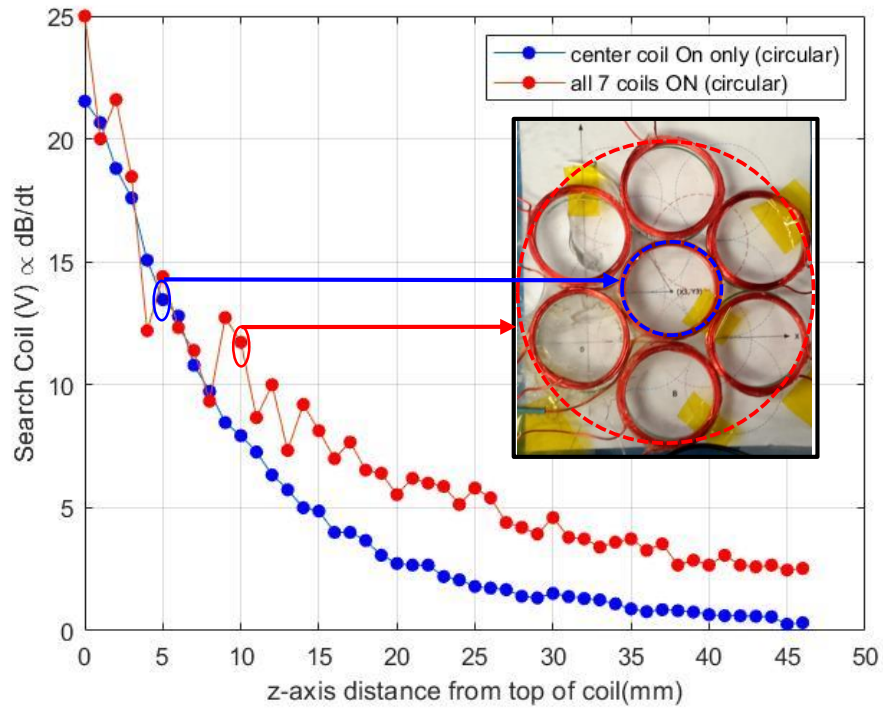


Figure 4.8: Seven-coil planar array realized using circular coils demonstrates controllable penetration depth by exciting a set of coils that behave as a single larger coil.

In both cases, when the search coil travels from 0 to 5.0 mm, above the center coil (z-axis), the magnetic field of that coil dominates but at > 5.0 mm the effect of the larger diameter synthesized effect starts to dominate, and the array shows the increased effective diameter and decay profile of a larger coil (75mm).

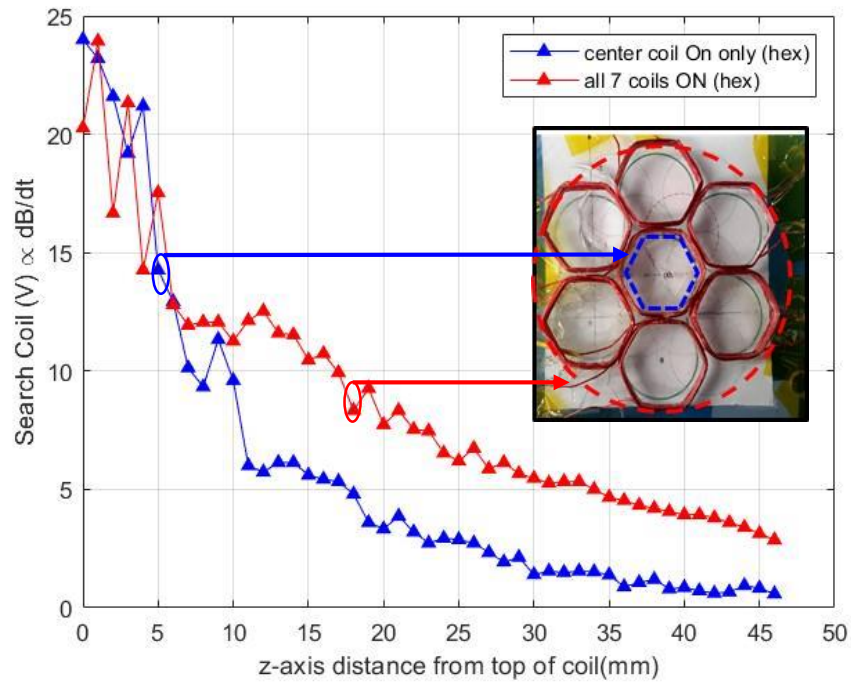


Figure 4.9: Seven-coil planar array realized using hexagonal coils demonstrates controllable penetration depth by exciting a set of coils that behave as a single larger coil.

Notably, when overlaying and comparing the two previous plots in Fig. 4.10 the seven-coil array composed of hexagonal coils data demonstrates an improvement in depth of penetration over the seven-coil array composed of circular coils.

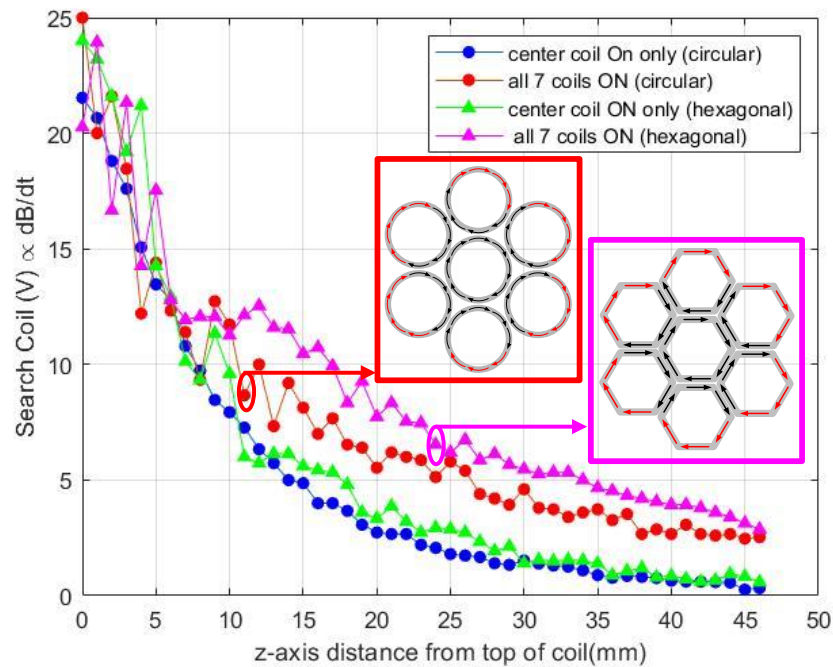


Figure 4.10: B-field decay profiles demonstrate improved depth of penetration for hexagonal coils over that of circular coils of the same equivalent diameter in the seven-coil planar topology.

For the case of the seven-coil array, it is postulated that the largest contributor to the increase in depth of penetration of hexagonal over circular coil-based arrays is due to enhanced cancellation of opposing current phases on the inner boundaries of the coils in the array. A comparative photograph of the two types of coils, in Fig. 4.11, reveals that enhanced cancellation is due to the geometry of hexagonal coils which possess longer distances of interfacial proximity along the flats of the hexagon shape. This is in direct contrast to the shorter interfacial proximity distance characteristic of a circular coil. Also, because of the hexagonal geometry there are smaller interfacial gaps at intersection locus points of the coils. In other words, the closer packing density between hexagonal coils enhances the phase cancellation.

In this specific use case, with all coils energized the benefit of closer proximities provided by hexagonal coils is increased coupling cancellation. To reiterate, proximity effects such as mutual coupling [Han et al, 2004], and distorted current waveforms, caused by unwanted coil to coil interaction, is mitigated by our ability to power down, ground non-energized coils and control individual coil current levels. The ability to mitigate the distorted waveforms is covered in Section 8.2. It has also been reported in the literature that hexagonal shaped coils have more uniform fields than that of circular or square coils [Modi et al, 2016].

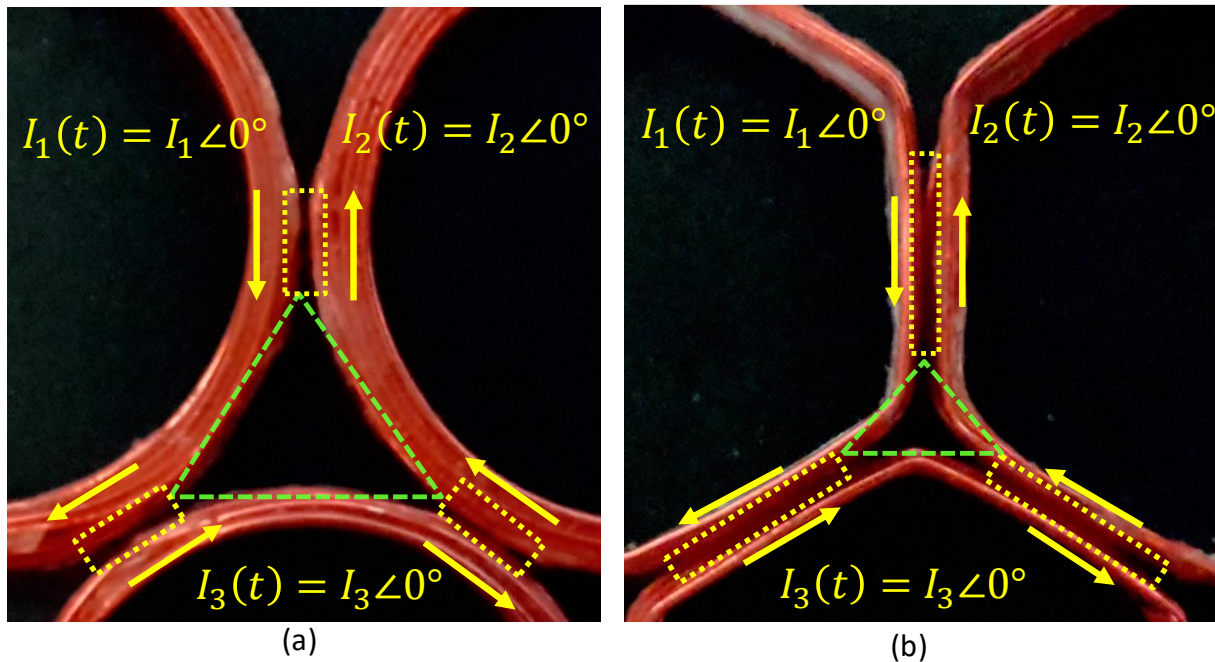


Figure 4.11. Hexagonal coil geometry improves mutual coupling for enhanced current phase cancellation due to decreased number of gaps and increased distance of physical proximity. (a) circular coil photograph and (b) hexagonal coil photograph.

FEM maps surface currents on each coil in Fig. 4.12 which reinforces the argument that the increase in coupling of coil-to-coil surface currents on adjacent hexagonal coils is greater than that of circular coils resulting in more complete cancellation of opposing currents.

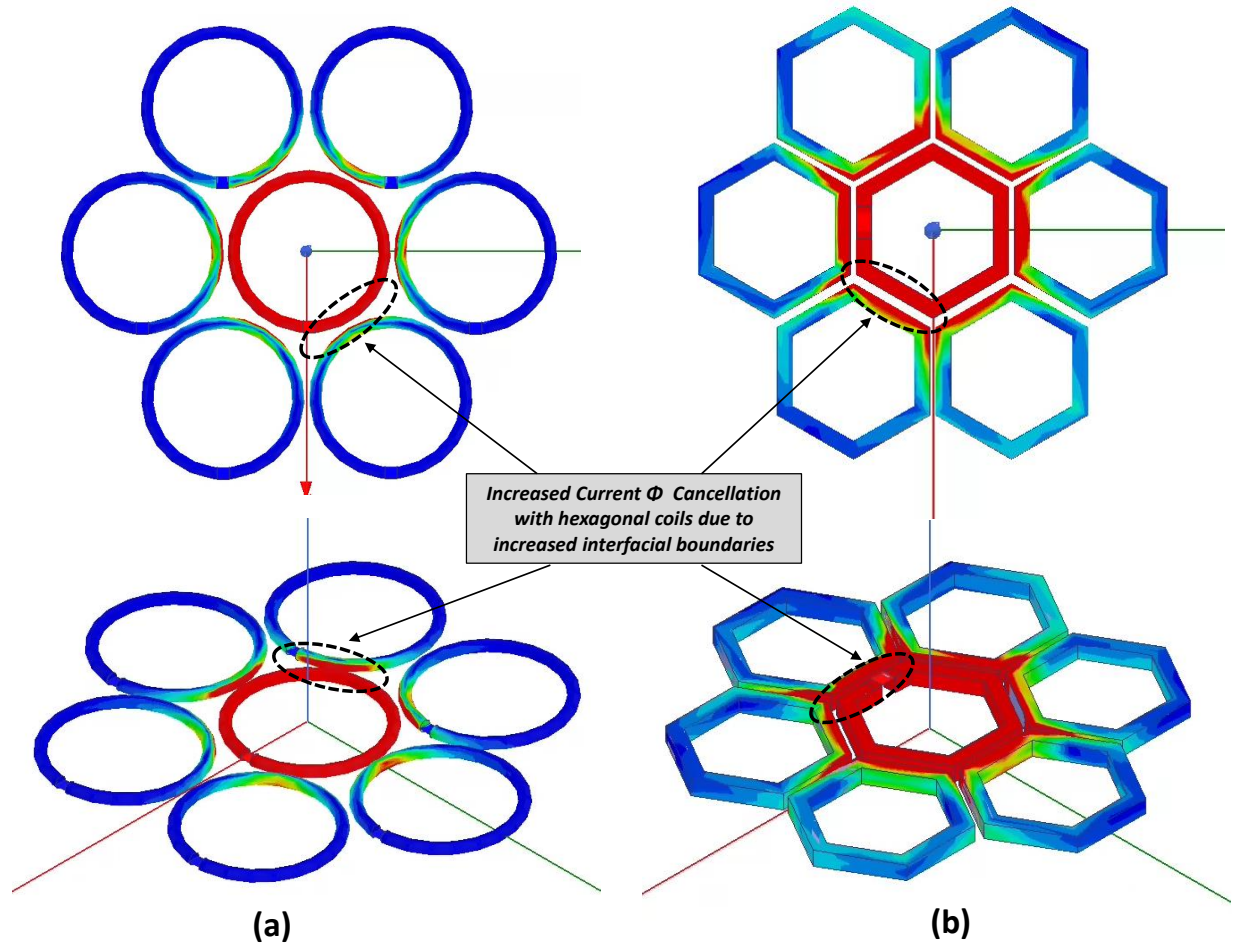


Figure 4.12: Simulation of coupled currents on adjacent coils of hexagonal coil geometry improves current phase cancellation over that of circular coils will limited coupling area, due to decreased number of gaps and increased interfacial boundaries; (a) circular coil – localized surface currents and (b) hexagonal coil – increase in localized coupled currents.

To further investigate the seven-coil cancellation effect, we measured additional geometric topologies using the 24mm diameter circular and hexagonal coils. The measurements in Fig. 4.13 of three circular coils (identical current and phase direction) versus three hexagonal coils further demonstrate that the synthesized increase in size or equivalent diameter (although triangular in shape) results in an increased penetration depth. Notably, there is a performance difference for the three-coil topology when compared with the seven-coil array decay profiles in Fig(s). 4.13 through 4.15. The intersection locus or center of the three coils in contrast to the center coil of the seven-

coil array allows for a different phase cancellation characteristic when the search probe travels within 0 to 5mm (z-axis) of the locus. Therefore, it follows that the cancellation of current phases at the intersection point the decay curves for the three-coil case are very similar to the theoretical and measured B-field plots previously seen in Fig. 4.2 (analytical) and Fig. 4.6 (measurement) for small versus large diameter coils.

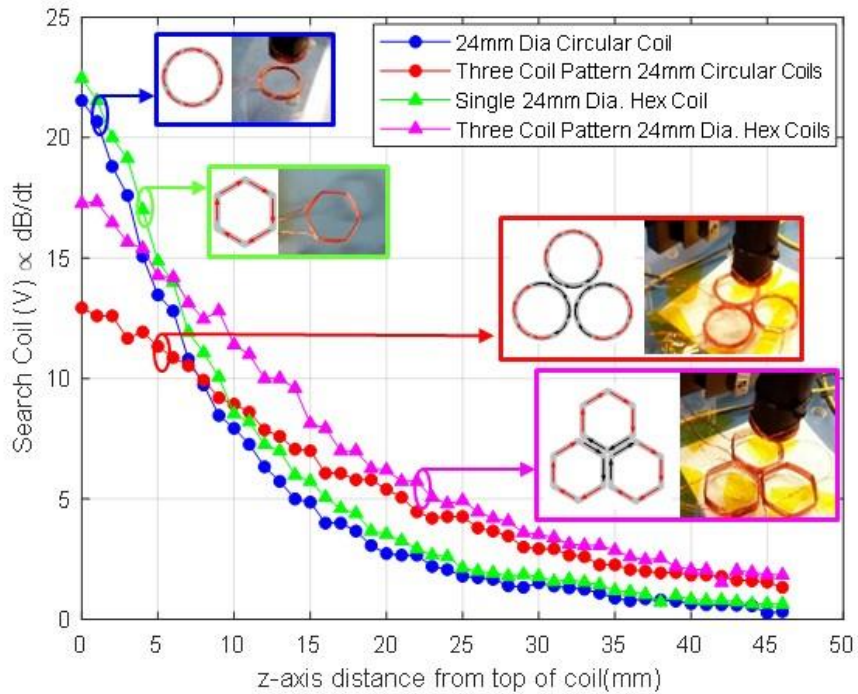


Figure 4.13: B-field decay profiles demonstrate improved depth of penetration for three coil patterns hexagonal coils over circular of the same equivalent diameter in the three-coil planar topology.

In a similar manner, the measurements in Fig. 4.14 of four circular coils (identical current and phase direction) versus four hexagonal coils demonstrate that the synthesized increase in size or equivalent diameter, although elliptical in shape, results in an increased penetration depth (Fig. 4.14).

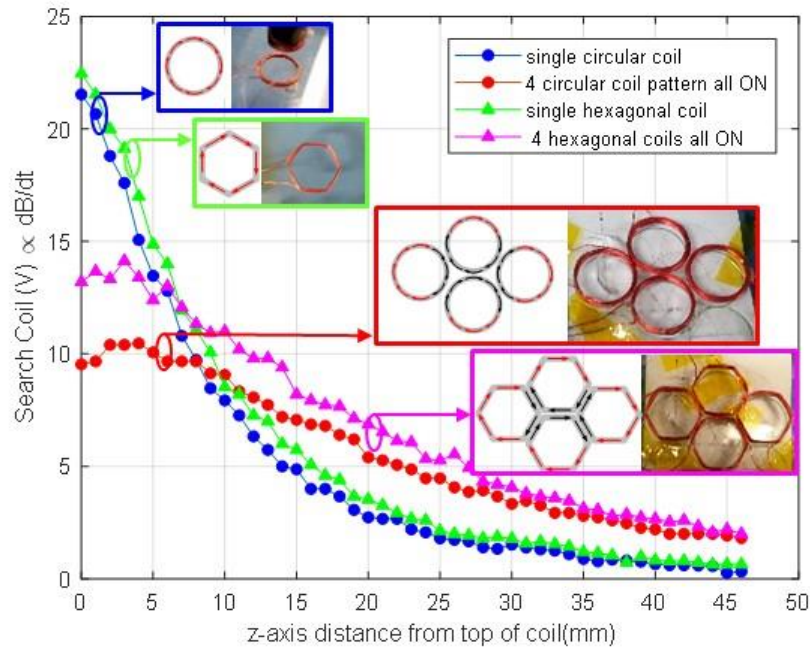


Figure 4.14: B-field decay profiles demonstrate improved depth of penetration for four coil patterns hexagonal coils over circular of the same equivalent diameter in the four-coil planar topology.

The six-coil offset stack case of circular coils (3 x 3) seen in Fig. 4.15 demonstrates increased depth of penetration by creating a synthesized diameter to behave like a larger 45mm coil. The same premise holds as in the previous two cases of the three and four coil topologies. The cancellation of current phases at the intersection point locus for this topology also follow the theoretical trend lines seen in Fig 4.2 and measurements in Fig. 4.6.

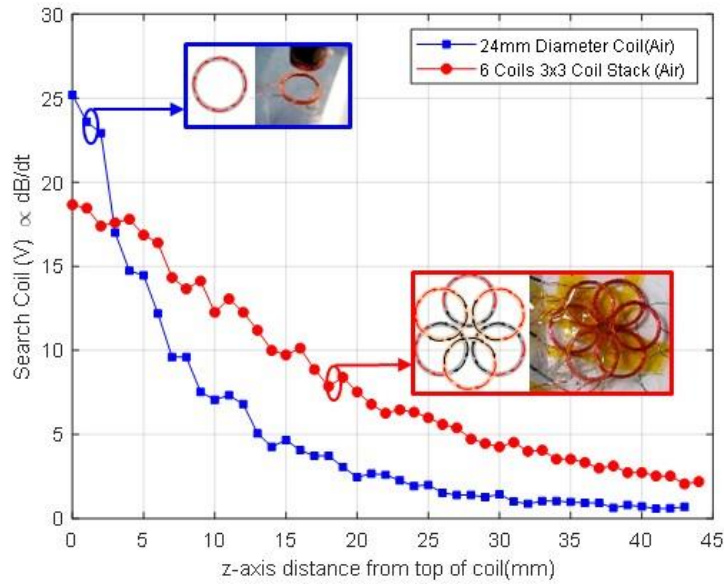


Figure 4.15: Six-coil planar array using circular coils results in improved decay profile of larger synthesized coil diameter of 45mm.

In summary, we report that various array topologies (three, four and seven coils), composed of hexagonal coils, have improved depth of penetration over that of the same topologies composed of circular coils as seen in Fig. 4.10 to Fig 4.15. An examination of the decay curves at the same reference locus allowed for an equitable comparison for the three and four coil cases. The reference locus was selected to be just beyond the scalp-skull boundary (1.5cm) at penetration depths from 2.0 cm to 4.5 cm (Fig. 4.10 to Fig. 4.15). All power supplies were held constant at 24V and 8A. As the number of coils (8 A /coil) increased in each case so did the penetration depth but at the price of higher energy consumption.

A comparison of the absolute value using reference locus method on the decay curve for the case of the single 75mm coils versus the seven-coil arrays was prohibitive. This was due to limitations in our fixed power supplies and the availability of large wattage rheostats. Nonetheless, an equitable method that eliminated the variables of voltage and current was selected for this case. Penetration depth performance was assessed by examining the B-field decay profile coefficients

of each type of seven-coil topology (synthesized diameter of 75mm) as compared to that of the 75mm diameter coil.

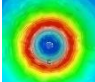

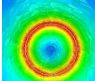
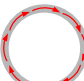
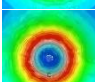

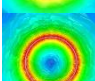

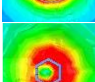

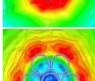

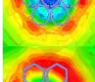
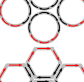
In general, B-fields attenuate with the inverse square of the distance from a “point of current” or current segment. Curve fitting to a rational polynomial form (p^0/x^2) with an inverse square relationship yields the lowest Root Mean Square Error (RMSE) using Matlab 2019A. However, first order exponential functions ($f(x) = ae^{-bx}$) also exhibit adequate curve fit estimates with comparable RMSE. Therefore, the use of this simple exponential function was used as a Figure of Merit (FOM) to compare rates of decay. This FOM provided adequate knowledge of the decay profile and solved the issue by leaving the variable or relative differences of power consumption out of the comparison.

In Table 4.1, the first column contains the induced E-field pattern via FEM, the second column the topology, the third the diameter (physical or synthesized) of the coil topology and the fourth the decay coefficients. The decay coefficients with the highest numerical value is indicative of a more rapid degradation of the B-field, as in the case of the smaller diameter coils. In contrast, the lowest numerical value decay coefficients are representative of a gradual attenuation of the B-field representative of larger coils or larger synthesized diameters.

Examination of the first five rows of Table 4.1 validate that the decay coefficients taken from our measurements are in good agreement between measured coils (24mm and 75mm) and theory (Biot-Savart law). The comparison between the seven coil multi-coil array topology, composed of hexagonal coils, has improved depth of penetration over that of the same multi-coil topology composed of circular coils. The decay coefficient for the larger single 75mm coil shows the most gradual decay coefficient. This implies that the multi-coil approach even when using the

enhanced cancellation of hexagonal coils will not surpass the large diameter coil in penetration depth when voltages and current are held constant.

Table 4.1: Comparison of B-field decay coefficients for various coil topologies.

MAGNETIC FIELD DECAY COEFFICIENTS				
E-Field pattern	Topology	Dia.(mm)	Data source	B – Field $f(x) = ae^{-bx}$
		24	<i>measured</i>	$b = 0.1012$
		75	<i>measured</i>	$b = 0.0322$
		24 ^a	<i>theory</i>	$b = 0.1025$
		75	<i>theory</i>	$b = 0.0302$
		24 ^a	<i>measured</i>	$b = 0.0932$
		75 ^b	<i>measured</i>	$b = 0.0589$
		75 ^b	<i>measured</i>	$b = 0.0434$

a - equivalent diameter (flat to flat for hexagonal shapes)
b - total equivalent diameter of array

The central question in this study is not to supplant the large diameter in practice but to show that a multifunction coil could behave as a larger diameter coil for the purposes of multifunctionality. It is highly unlikely that if the current could be held equal for the 75mm case vs. the seven-coil array that the seven-coil case would show better performance. At best, though equal performance (including equal power consumption) between the two cases is possible by improving cancellation in the array, as in the case of our hexagonal coils. However, our design strives to offer the other advantages for the seven-coil case (resident in an array) to be rapidly

reconfigured on a pulse-to-pulse basis from one function (enhanced focality) to another (enhanced depth of penetration).

To assess future trends in noninvasive neuromodulation, we report the design, fabrication and demonstration of a multifunction multi-coil or dense array system that validates reconfigurable and variable depth of penetration. We also report, a seven-coil array topology (a subarray of our stacked layer, composed of hexagonal coils, that has improved depth of penetration over that of the same multi-coil topology composed of circular coils (Fig. 4.10 to Fig. 4.15). Measurements confirm that the depth of penetration of the B-field can be reconfigured (only simulated in the literature [Yang et al, 2010; Wei et al, 2017; Ho et al, 2009] by varying current magnitude and phase of the smaller coil diameters in the array to achieve the same decay profile performance of a larger diameter coil. To the best of our knowledge these are the first reported measurements in the literature. Hexagonal coils used in multi-coil arrays, also show promise as they are best applied in high packing density head-worn or conformal multi-coil arrays.

A scalable testbed has been established as a flexible tool to examine future applications of neuromodulation techniques using multichannel dense coil arrays. From an engineering perspective, our central question; to determine if the multi-coil approach is technically tractable remains and will continue through a series of subsequent papers. These papers will examine user-specified excitation patterns over multiple sites (simultaneously or sequenced), reduced extraneous excitation, proximity effects due to coil-to-coil interaction and more power efficient waveforms. The goal of these studies is to provide a clear technical roadmap addressing the key challenges and potential benefits of this approach.

This chapter is based on Matthew C. Smith, Aobo Li and Daniel. F. Sievenpiper, "A Multifunction Dense Array System with Reconfigurable Depth of Penetration," *IEEE Journal of Electromagnetics, RF and Microwaves in Medicine and Biology*, vol. 5, no. 1, pp. 35-45, March 2021. The dissertation author was the primary researcher and author of this paper.

CHAPTER 5 REDUCED EXTRANEEOUS EXCITATION

5.1 INTRODUCTION

A major goal of brain stimulating devices is to localize the stimulation of neuronal targets leaving nearby brain regions unaffected [Wagner et al, 2009] to minimize unintended effects. Techniques such as ferromagnetic or ferrimagnetic materials [Goetz and Deng, 2017], and active shields [Hernandez-Garcia et al, 2010] to enhance E-field localization or focality have been reported in the literature. A ferromagnetic or ferrimagnetic material when interfaced at the back of a figure-of-eight coil can concentrate the B-field flux lines closer to the conductors, so that the field energy is smaller for the same or even larger field strength in the target area [Goetz and Deng, 2017]. Ideally, a steel backplane can shunt up to half of the field to reduce the energy content of the stray flux. A limitation of this approach in high field magnetic stimulation is strong field amplification in the target demands a high magnetic permeability. Ferromagnetic materials such as iron or silicon steel provide both high saturation levels of up to 2 T and high relative magnetic permeability but are electrically conductive and require lamination to reduce eddy-current loss [Goetz and Deng, 2017]. Research continues in high field magnetic stimulation with shield using both ferromagnetic and ferrimagnetic materials but to date appears to exist primarily in the academic realm due to its design complexity. As an alternative, ferrites have been considered but as they are not electrically conductive and, therefore, present low loss, but saturate early at 500mT and offer lower relative permeabilities of 1000 [Gutfleisch et al., 2011]. Thus, in the case of high field magnetic stimulation (1-2T) low saturation levels remove ferrites from the trade space. However, ferrites may be a viable candidate for improving localization or focality of fields in low field magnetic stimulation which is typically $< 500\text{mT}$. Similarly in the realm of high field magnetic stimulations the research on the use of active shields [Hernandez-Garcia et al, 2010] is

also limited by the induction of Lorentz forces between the primary and the shielding coils. Similarly active shields may be a viable candidate for improving localization or focality of fields in low field magnetic stimulation which is typically $< 500\text{mT}$. Therefore, it is reasonable to conclude now that ferrimagnetic, ferromagnetic and ferrites should be considered in low field magnetic stimulations if the improved focality or reduced extraneous excitation is beneficial to neuroscience or other applications.

Our proposed approach uses the 3-layers of the multi-coil dense array to reduce extraneous excitation around a given pattern and is also more applicable to low field magnetic stimulation at this point in development specifically due to proximity effects (e.g., mutual coupling and Lorentz forces) as reported by earlier [Hernandez-Garcia et al, 2010; Han et al, 2004].

When eddy currents are generated in a conductive solution (e.g., cortical tissue), they must form continuous paths, i.e., they generate return currents, as required by Kirchhoff's laws and the continuity equation. Any stimulated region thus causes additional stimulation in the surrounding tissues.

The advantage of our proposed approach is that it provides complete control over the current profile on the entire surface of the brain, allowing us to manipulate the spatial extent of the return currents. By spreading them out over a large area we can reduce their density, as illustrated in Fig. 5.1, until it is far below the stimulation threshold.

This is not possible with other coil array geometries which do not provide control over current direction and magnitude over the full array. A single layer array and many existing multi-layer array designs can only generate eddy currents in one direction in each region. Our approach allows the direction and magnitude of current in every pixel to be independently controlled, within the limits of Maxwell's equations and the continuity equation.

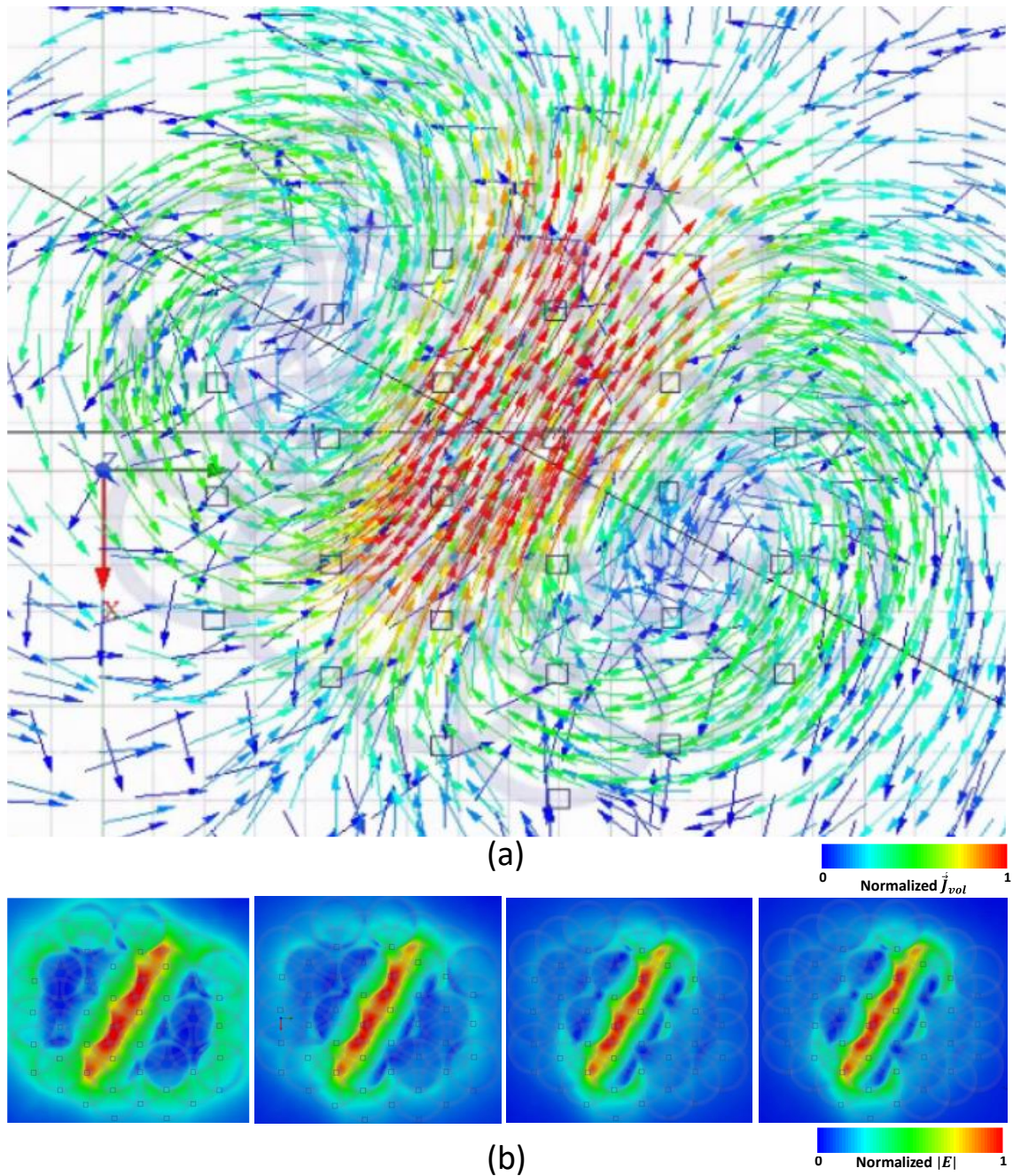


Figure 5.1: Eddy currents in a conductive media. (a) eddy currents form continuous paths in a conductive media. (b) simulation of diffused eddy currents in a conductive media using our method.

5.2 PRINCIPLES OF OPERATION

Reduced excitation around a unilinear excitation locus generated by an array of 35 coils (zones 1, 2, 3) is demonstrated by spreading or diffusing eddy currents out over a large area. This reduces their density, as illustrated in Fig. 5.2, until it is far below the stimulation threshold (high field) and minimized to improve localization for low field applications. This is accomplished by tapering coil current weighting which suppresses $\vec{E}_{max}/2$ by $\sim 18\%$ around the periphery of the unilinear excitation pattern.

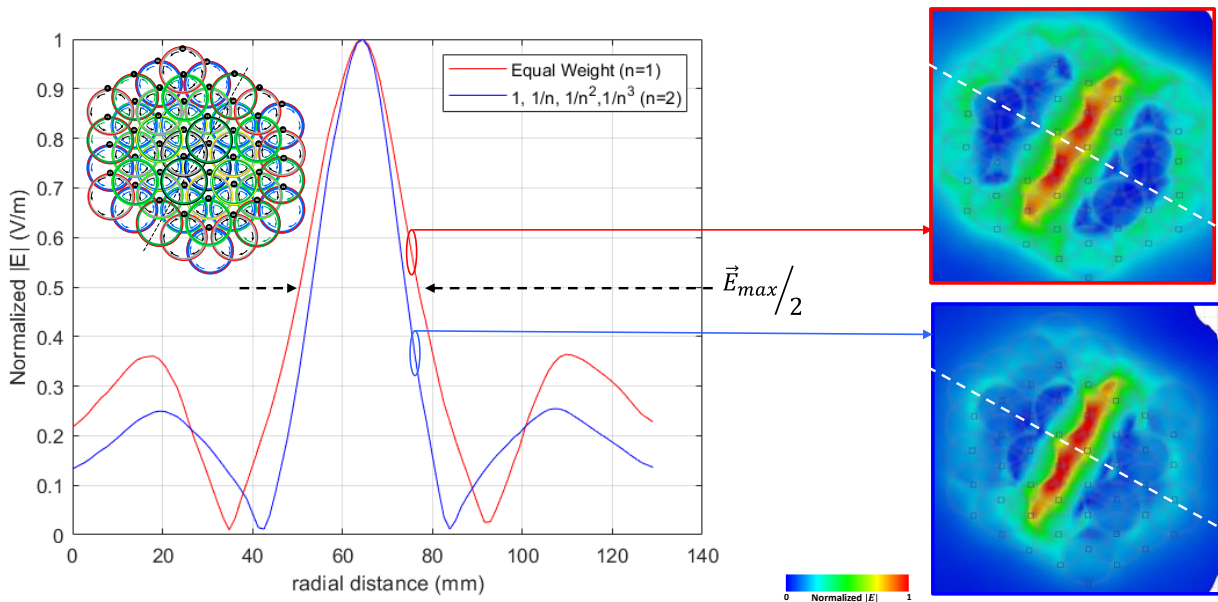


Figure 5.2: Tapering coil current weighting using zones 1,2,3,4 (43 coils) suppresses $\vec{E}_{max}/2$ by $\sim 18\%$ around periphery of excitation locus (note: evaluation line depth in conductive media = 6mm).

To demonstrate, a simple example of coil current amplitude tapering is given in Table 5.1 whereby the amplitudes are progressively decreased as determined by a simple function (e.g., $1/n^k, 1/n^{k+1}, \dots$). As a result, the eddy currents move out from the excitation locus and diffuse farther out and away from the points of excitation as the zones are increased as seen in Fig. 5.3.

Table 5.1: Example - Tapered coil weights for zones 1 ,2, 3 and 4 (43 coil array)

Zone/Coil #	Taper	4000W → 796W			
		Equal Weight	n=2	n=3	n=4
Zone 1 (4 coils): 13, 17, 22, 25		1 (100W)	1 (100W)	1 (100W)	1 (100W)
Zone 2 (6 coils): 9, 12, 21 (L) 18, 26, 29 (R)		1 (100W)	$1/n = 1/2$ (50W)	$1/n = 1/3$ (33.3W)	$1/n = 1/4$ (25W)
Zone 3 (14 coils): 2, 5, 8, 16, 24, 28, 32 (L) 6, 10, 14, 23, 30, 33, 35 (R)		1 (100W)	$1/n^2 = 1/2^2$ (25W)	$1/n^2 = 1/3^2$ (11.1W)	$1/n^2 = 1/4^2$ (6.25W)
Zone 4 (21 coils): 44, 39, 1, 4, 11, 20, 27, 31, 34, 37 (L) 40, 3, 7, 41, 19, 42, 43, 36, 38, 45 (R)		1 (100W)	$1/n^3 = 1/2^3$ (12.5W)	$1/n^3 = 1/3^3$ (3.7W)	$1/n^3 = 1/4^3$ (1.56W)

Note: (a) Coil #: 13 , 25, 34, 3 (OFF) (b) Coil #: 28 , 17, 6 (L) 32, 22, 10 (R) (Constant)

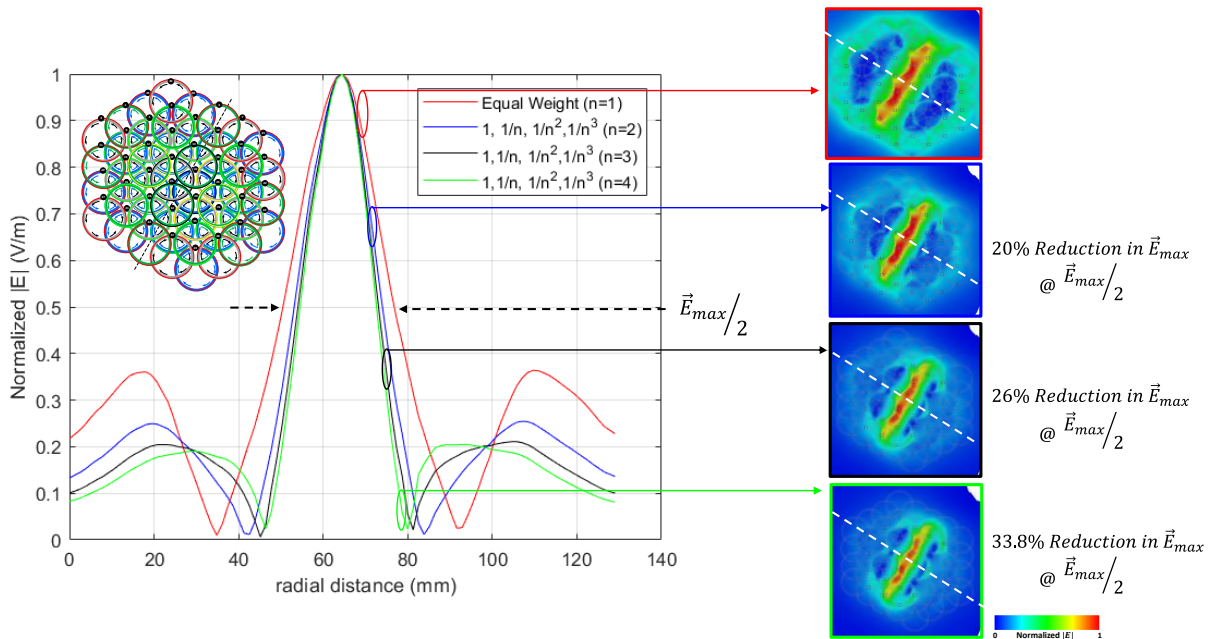


Figure 5.3: Reduced extraneous excitation around a unilinear pattern using the weighting values in Table 5.1. Tapering coil current weighting suppresses at $\frac{\vec{E}_{max}}{2}$ by 20% - 33.8% around periphery of excitation locus.

The concept and the definition of the template array, first introduced earlier in Section 2.4, can be further expanded from four coils in zone 1(4 coils) to zone 6 (103 coils) as illustrated in Figures 5.4 and 5.5.

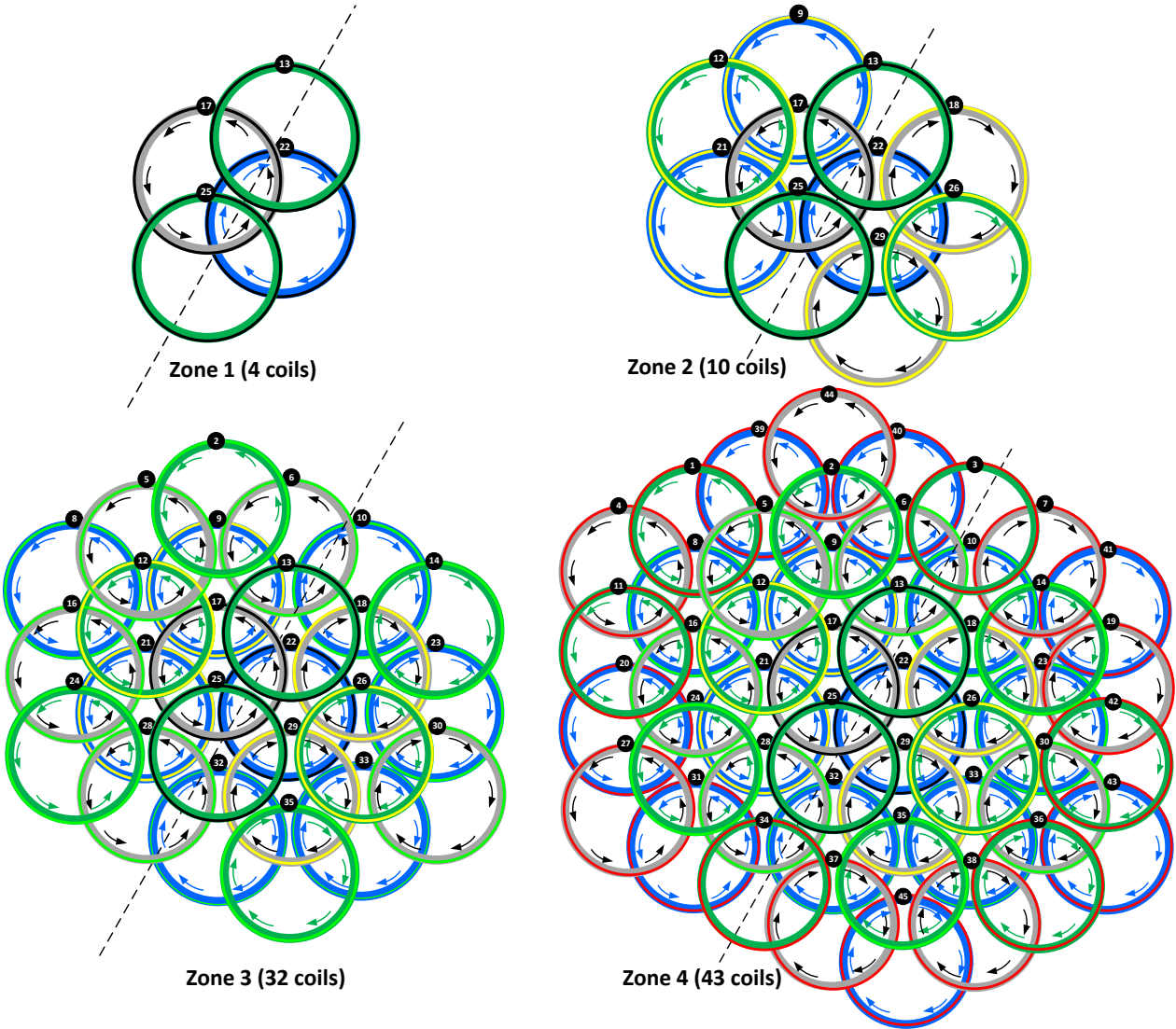


Figure 5.4: Definitions of zone 1(4 coils) through zone 4(43 coils) for used for reduced extraneous excitation.

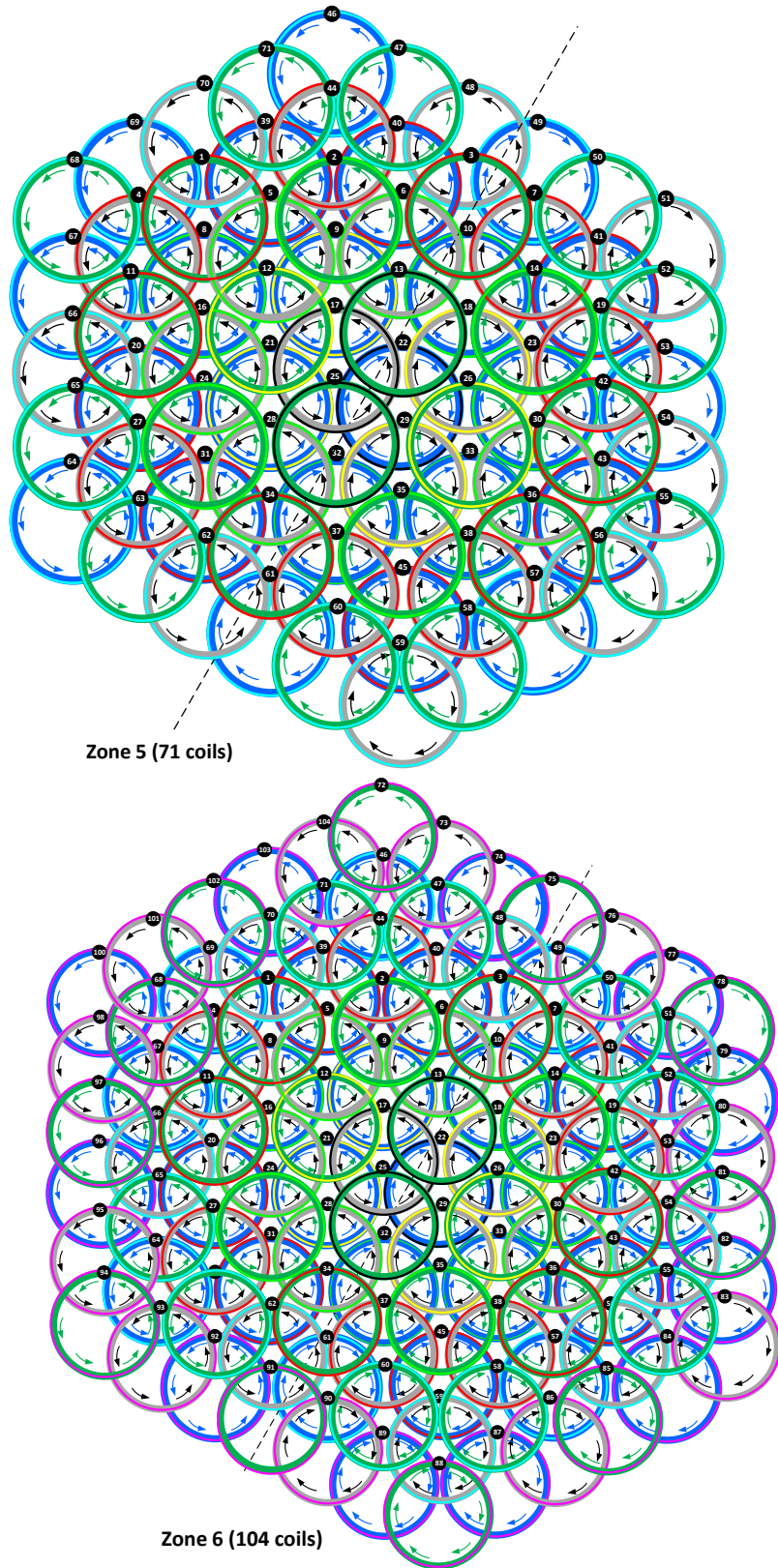


Figure 5.5: Definition of zone 5(71 coils) and zone 6(103 coils) for used for reduced extraneous excitation.

Using the same tapering function (e.g., $1/n^k, 1/n^{k+1}, \dots$) and the addition of zone 5 (73 coils) suppresses $\vec{E}_{max}/2$ by $\sim 22.7\%$ around periphery of excitation locus which is an improvement in the suppression of the unwanted E-fields by 3%. As a result, the eddy currents move out from the excitation locus and diffuse farther out and away from the points of excitation as the zones are increased as seen in Fig. 5.6.

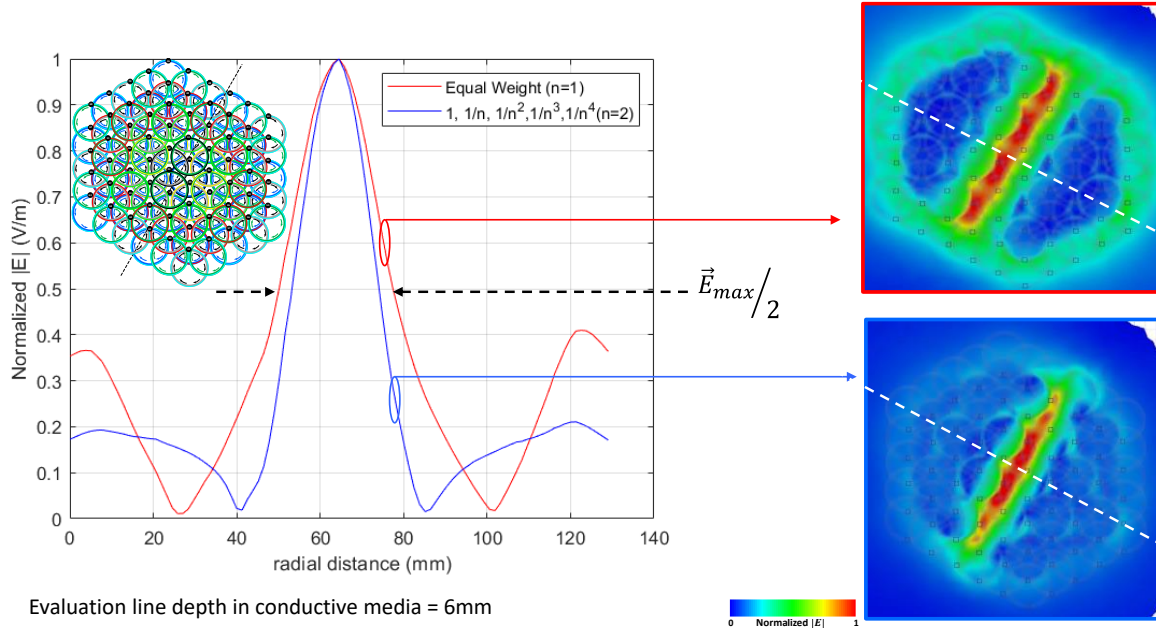


Figure 5.6: Tapering coil current weighting with zone 5 (71 coils) suppresses $\vec{E}_{max}/2$ by $\sim 22.7\%$ around periphery of excitation locus (note: evaluation line depth in conductive media = 6mm).

Repeating the same process, we use the same tapering function (e.g., $1/n^k, 1/n^{k+1}, \dots$) with the addition of zone 6 (103 coils) suppresses $\vec{E}_{max}/2$ by ~ 23.5 to 35.3% around periphery of excitation locus. As a result, the eddy currents move out from the excitation locus and diffuse farther out and away from the points of excitation as the zones are increased as seen in Fig. 5.7 (a). A bounding limit on how much suppression is possible based on the number of zones becomes more evident on both the upper and lower bounds. From the perspective of the lower bound Fig. 5.7 (b) indicates that there is little or negligible suppression when using zones 1 and 2 (10 coils only) and that when moving to zones 1,2,3,4,5,6 we see a increased suppression of 23.5 to 35.3%.

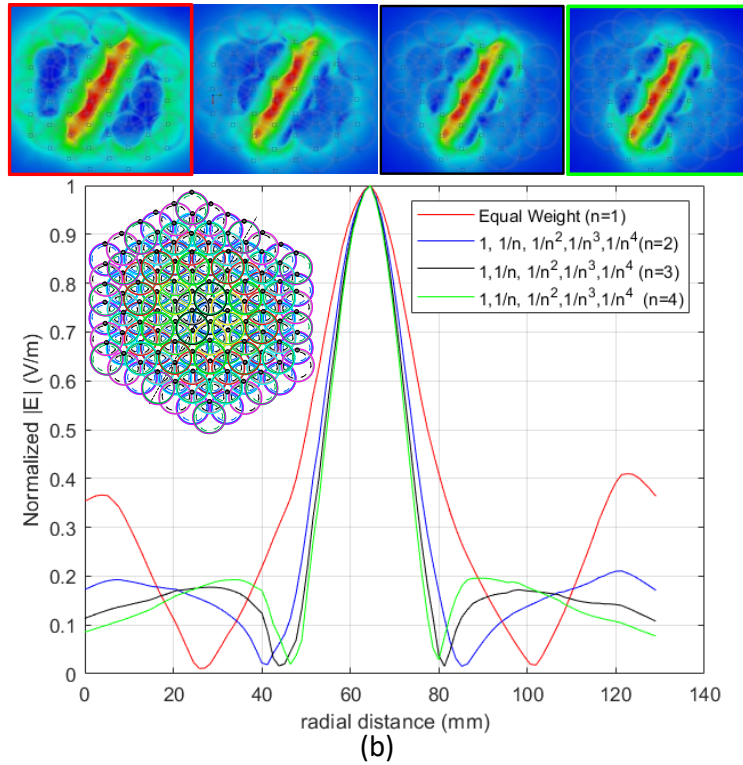
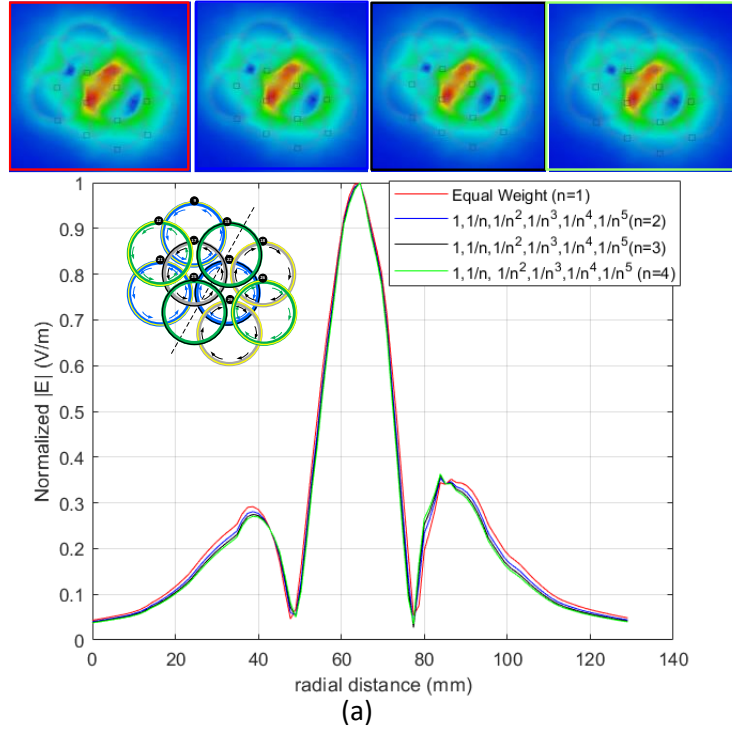


Figure 5.7: Lower and upper limits based on number of zones size on reduced extraneous excitation. (a) no significant reduction in reduced extraneous excitation with zone 2 (10 coils), (b) significant reduction when increasing to zone 1,2,3,4,5,6 of 23.5 to 35.3%.

In summary, the lower bound in Table 5.2 and Fig. 5.8 indicates that there is negligible suppression when using zones 1 and 2 (10 coils only) and that when moving to zones 1,2,3,4,5,6 an increased suppression of 23.5 to 35.3% is observed.

Table 5.2: Extraneous reduction (%) increases as number of zones and are increased.

Weighting	% Reduction (4 coils)	% Reduction (10 coils)	% Reduction (35 coils)	% Reduction (43 coils)	% Reduction (71 coils)	% Reduction (103 coils)
1	0	2.1	11.76	20	22.7	23.5
2	-	6.6	16.78	26	27.4	30.1
3	-	-	21.34	33.8	34.8	35.3

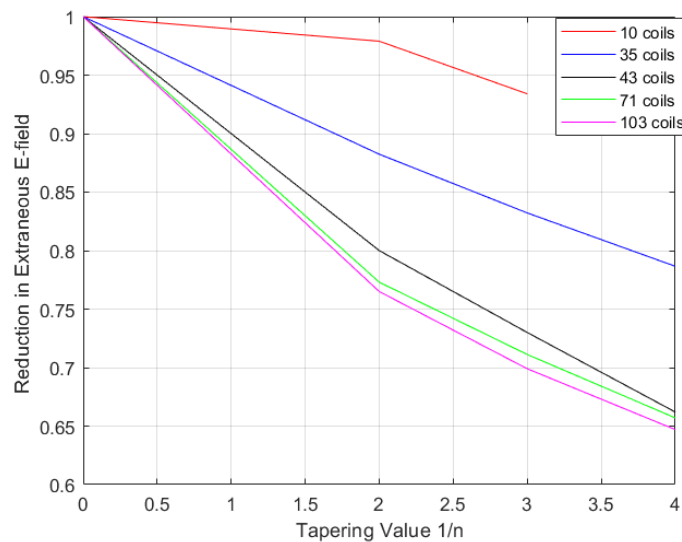


Figure 5.8: Lower and upper limits based on number of zones, tapering values vs. reduction in extraneous excitation.

This chapter is based on Matthew Smith and Daniel Sievenpiper, “A New Synthesis Method and Magnetic Instrument for Complex Electric Field Patterning with Enhanced Localization”, *IEEE Magnetic Letters*, vol. n, no. 2022, pp. (5 pages), *In preparation*. The dissertation author was the primary researcher and author of this material.

CHAPTER 6 SYSTEM ARCHITECTURE

Our system overview in Fig. 6.1 of the scalable multichannel system composed of three 3U chassis that stimulate various test array topologies using monophasic and biphasic waveforms. The main components in the system block diagram in Fig. 1 (a) are the dual insulated-gate bipolar transistor (IGBT) switch/energy storage assembly of which there are four switches and eight capacitors per 3U rack. Six pairs of external power supplies provide the positive channel voltages (+24 to +40 V) and negative channel voltages (-24 to -40 V) to each capacitor bank. A dual gate driver controls one dual IGBT per channel that switches the current (positive or negative) to the coil. Independent control of all channels (positive or negative) is in two programmable clock driver circuits (1:10) which further shapes and reduces noise in the pulse trains to the dual IGBT drivers. The coils studied range from 24mm to 75mm in diameter, all with inductances of $10\mu\text{H} \pm 1\%$, with 8A peak current pulses (10A for E-field measurements), achieving $<95\mu\text{s}$ rise time and 0.5mT peak fields. Custom coils both circular and hexagonal of various diameters were wound by modifying a traditional coil winder/turn counter and adding a tensioning reel (Fig. 6.2 (a)) and PTFE forming collars (circular or hex) in Fig. 6.2(b) for this study. A finished 12-coil 3-layer dense array is shown in Fig. 6.3 (c).

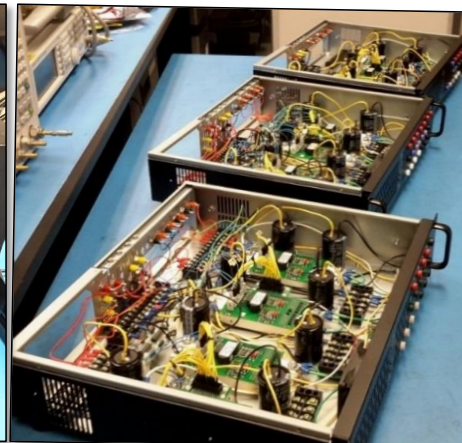
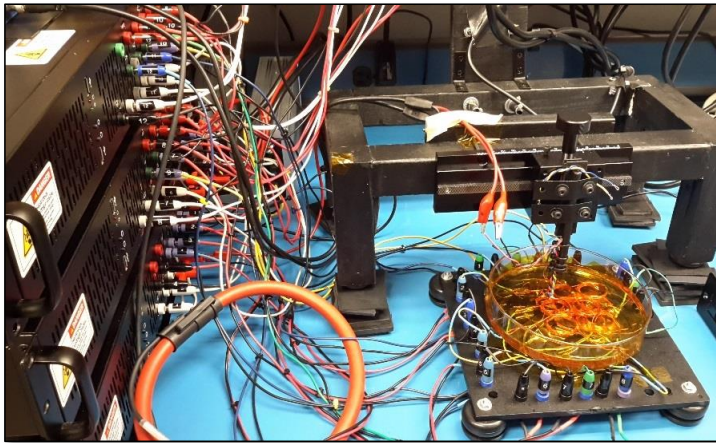
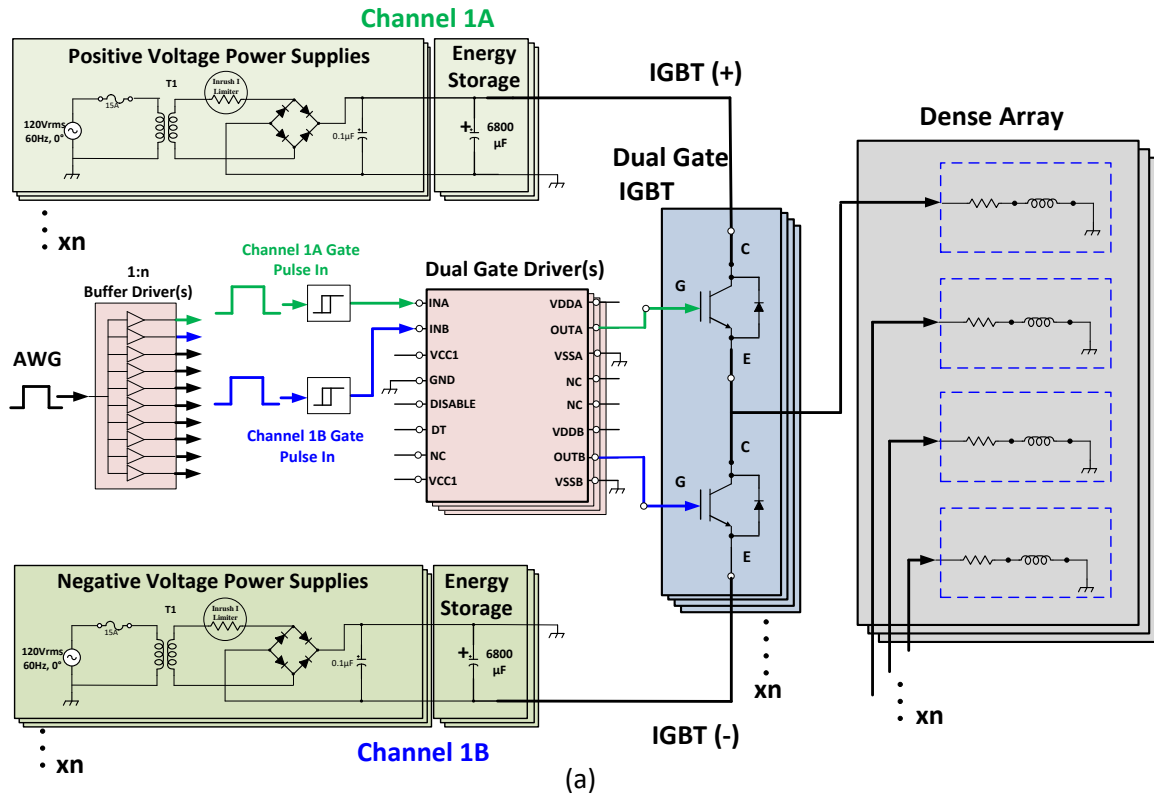


Figure 6.1: Multichannel (13 channel) dense array system. (a) system block diagram and (b) dense array in test and (c) internal photo - three 3U racks populated with IGBT switch / driver assemblies (c) coil array topologies under test, (d) custom coil fabrication fixture and (e) photo of 3-layer dense array.

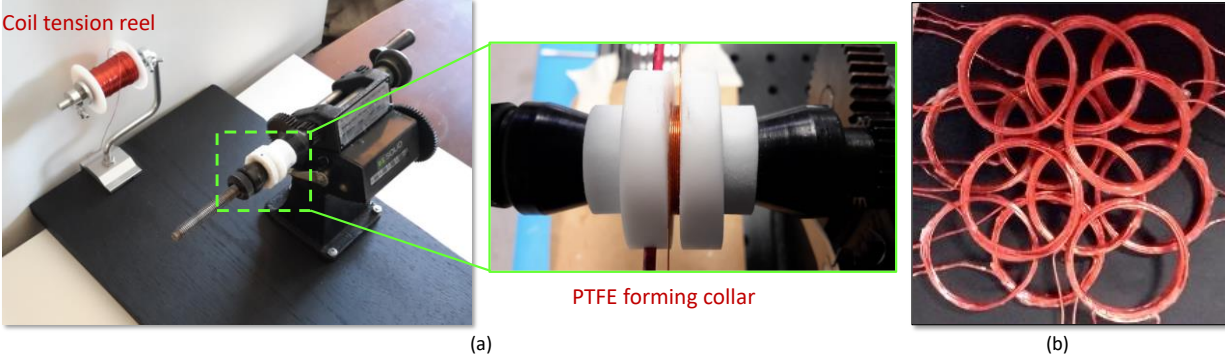


Figure 6.2: Fabrication of coils and finished dense array. (a) custom coil fabrication fixture and (b) photo of 3-layer dense array.

Table 6.1 summarizes our system parameters which enable fundamental research and exploration of new array concepts and technology in a scalable testbed. The column entitled “scalable system” is enabled by the IGBTs and drivers which are rated for higher voltages and currents of $1200V_{peak}$ and $600 I_{peak}$ respectively.

Table 6.1: System Specifications

Parameter	Current System	Scalable System
Coil $I_{waveform}$	Monophasic/ Biphasic	Monophasic/Biphasic
PRF	1-50 Hz	1-50 Hz
PW	100 μ s -1ms	100 μ s -1ms
I_{peak}	8 - 40 A	> 600 A
V_{peak}	24 - 40 V	>1200V
$\tau_{rise\ time}$	<95 μ s	<95 μ s
# Channels	12	16
Pulse Shape	reconfigurable	reconfigurable
B_{peak}	0.5 mT	> 0.35 T
Topology	Planar	Planar/Curved
Layers	Two	Three
Coils	Circular and Hex	Circular and Hex
Thermal	forced air	various ^{a,b}

a - forced air and fluid cooling manifold with acoustic dampening
b - experimentation with low cost superconducting technology

The pulse repetition frequency (*PRF*) is 10Hz with peak voltages at $24V_{peak}$, peak currents (I_{peak}) at 8 A (10 A for E-field experiments) and 250 μ sec pulse widths (*PW*) were held constant for all measurements. A subchannel circuit schematic from the power electronics software (PSIM, Ver. 11) used to simulate all circuit behavior is shown in Fig. 6.3 with four measurements of the various waveforms. Coil current waveforms can be adjusted to monophasic or biphasic with reconfigurable pulse widths and shapes (e.g., triangular) via an arbitrary waveform generator locked to a standard timing clock for all channels.

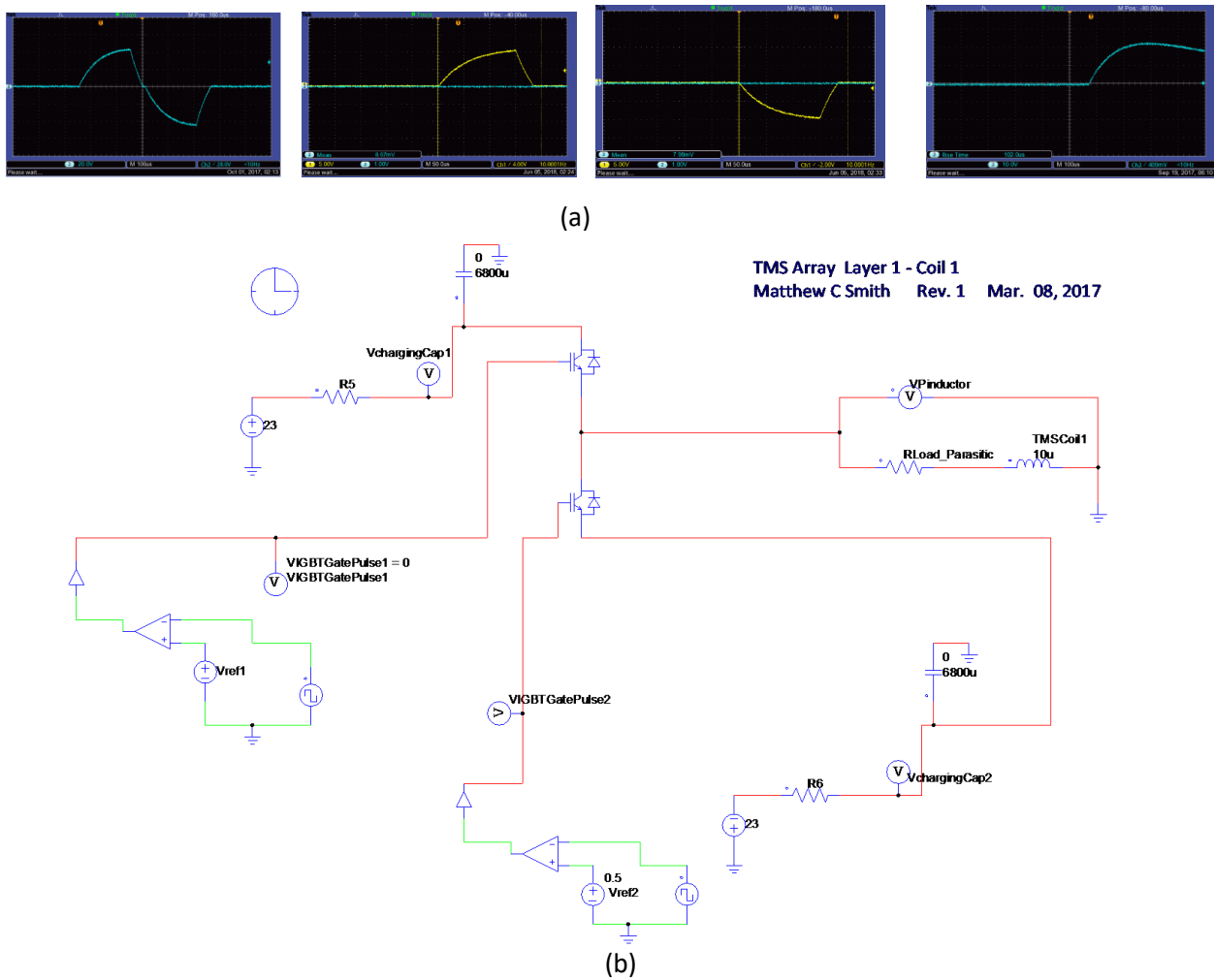


Figure 6.3: Waveform measurements simulation software schematic. (a) measurements of monophasic and biphasic waveforms and rise time and (b) schematic of subchannel (PSIM) software used for design verification.

Chapter 6 of this dissertation is based on Matthew C. Smith, Aobo Li and Daniel. F. Sievenpiper, "A Multifunction Dense Array System with Reconfigurable Depth of Penetration," *IEEE Journal of Electromagnetics, RF and Microwaves in Medicine and Biology*, vol. 5, no. 1, pp. 35-45, March 2021. The dissertation author was the primary researcher and author of this paper.

CHAPTER 7 METHODS FOR MEASUREMENT AND SIMULATIONS

7.1 E-FIELD MEASUREMENT METHODS

In terms of spatial distribution, the magnetic field that is generated by the current in the stimulation coil is almost independent from the specific head anatomy, whereas the induced E-fields in the biological media are not [Grehl et al, 2016; Esselle and Stuchly, 1992]. As such, we developed a rotating dual - dipole probe in Fig. 7.1 [Glover et al, 2007; Hart et al, 1991] that when immersed in polyvinylpyrrolidone solution (PVP) [Ianniello et al, 2018], measures the potential difference between the two probes tips (10mm separation) as it moved through the solution. The probe was positioned at a depth of 4mm from the bottom of the petri dish (2.5 mm thick) in the solution. All the coils were coated with urethane [CRC Seal Coat®, Warminster, PA] and were in “slight” contact with each other in the various topologies. There was an air gap of 2mm between the top coil layer and the bottom of the petri dish (a total of 8.5mm from probe to top coil layer (Fig. 7.1). A low noise differential amplifier [AlphaLab Inc., Oscilloscope preamplifier LNA10], in Fig. 7.1 was used to amplify and filter the resulting voltage waveform. Measured data was recorded on an oscilloscope and stored in memory for post-processing using Matlab19A [Mathworks, Natick, MA]. The relationship for the measured voltage is $V_{meas} = \Delta V / G$ where ΔV is the potential difference at the dipole tips and G is the gain of differential amplifier.

A custom near field scanner and a precision z-axis translation stage [Edmund Optics, 125mm translation stage] with 1.0 mm steps mounted on a custom stabilization fixture in Fig. 7.1 (c) were both used for E-field radial and contour measurements. A Rogowski coil [Fluke Corp., i2000] shown in the Fig. 7.1 system photograph, was used to measure the time-varying drive current delivered to each coil in the array which was at a pulse repetition frequency (*PRF*) of 10Hz

with peak voltages at $\pm 24V$, and peak currents at $\pm 10A$. Monophasic and biphasic waveforms were used with $300\mu\text{sec}$ pulse widths, $95\mu\text{s}$ rise times, and 0.5mT peak B-fields. The custom 30mm diameter coils were designed and measured as $L = 10\mu\text{H} \pm 1\%$, $R_{\text{series}} = 0.6\Omega$. Two coats ($>2\text{mm}$) of clear high temperature (121.1°C max.) urethane were applied to each coil [CRC Seal Coat®, Warminster, PA].

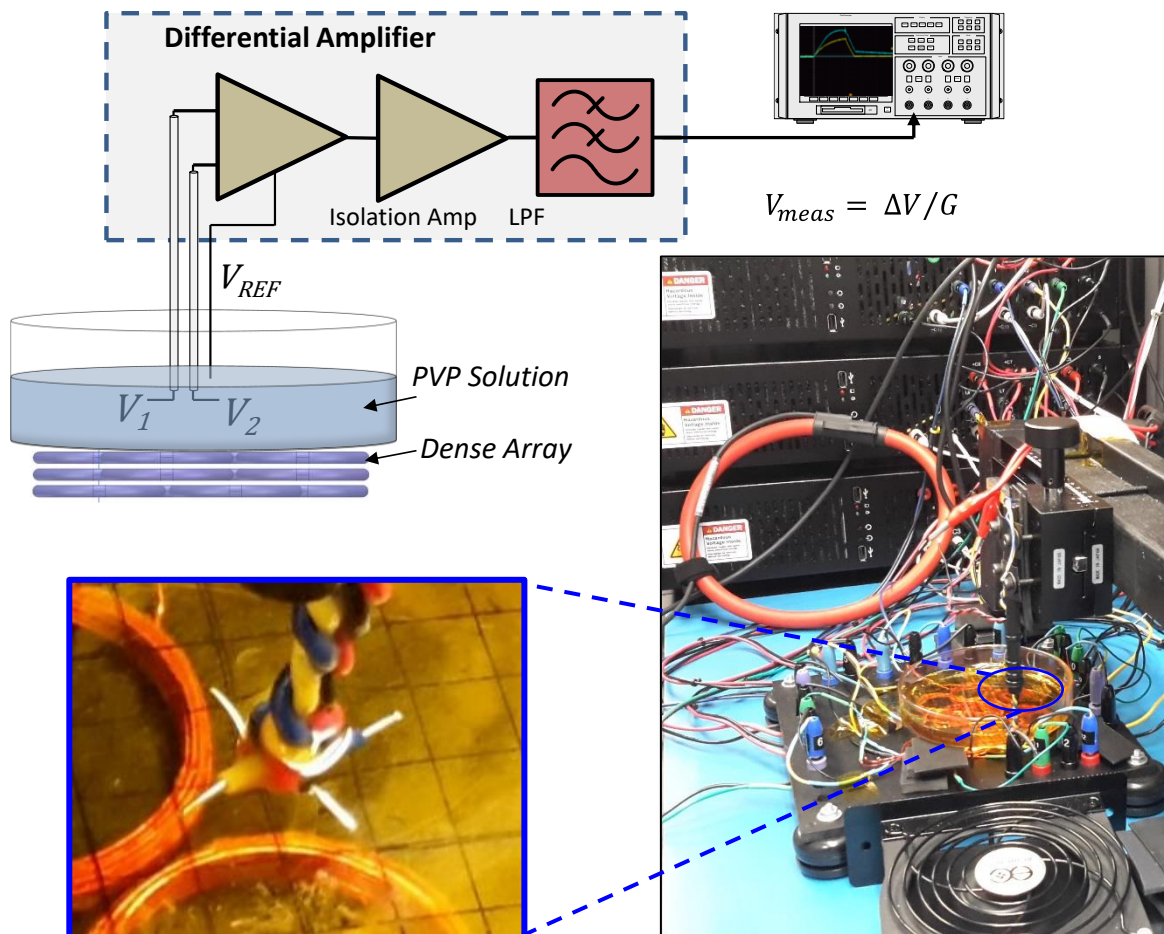


Figure 7.1: E-field and eddy-current measurement in PVP solution includes a block diagram of measurement method, a photograph of dual dipole rotary probe immersed in PVP solution over the dense array, and photograph of the system with a 13-coil dense array under test in the PVP solution.

A custom near field scanner (Fig. 7.4) and a precision z-axis translation stage [Edmund optics] with 1.0mm steps mounted on a custom stabilization fixture in Fig. 7.1 were both used for

E-field radial and contour measurements. A Rogowski coil (Fluke) shown in the Fig. 7.1 system photograph, was used to measure the time-varying drive current delivered to each coil in the array which was at a pulse repetition frequency (*PRF*) of 10Hz with peak voltages at $\pm 24V$, and peak currents at $\pm 10A$. Monophasic and biphasic waveforms were used with 300 μ sec pulse widths, 95 μ s rise times, and 0.5mT peak B-fields. The custom 30mm diameter coils were designed and measured as $L = 10\mu H \pm 1\%$, $R_{series} = 0.6\Omega$. Two coats ($>2mm$) of clear high temperature (121.1 $^{\circ}C$ max.) urethane (CRC Seal Coat $^{\circ}$) were applied to each coil.

An alternate method of measuring the contour patterns of the induced E-field was investigated using a thermal imager (Seek thermal). The method was not satisfactory due to the narrow time window for making the measurement. It was very short on the order of 1-2 seconds before thermal conduction in magnetic absorber [MAGRAM] smeared the image. An example, of a successful measurement was made for a traditional figure 8 coil topology in figure Fig. 7.2.

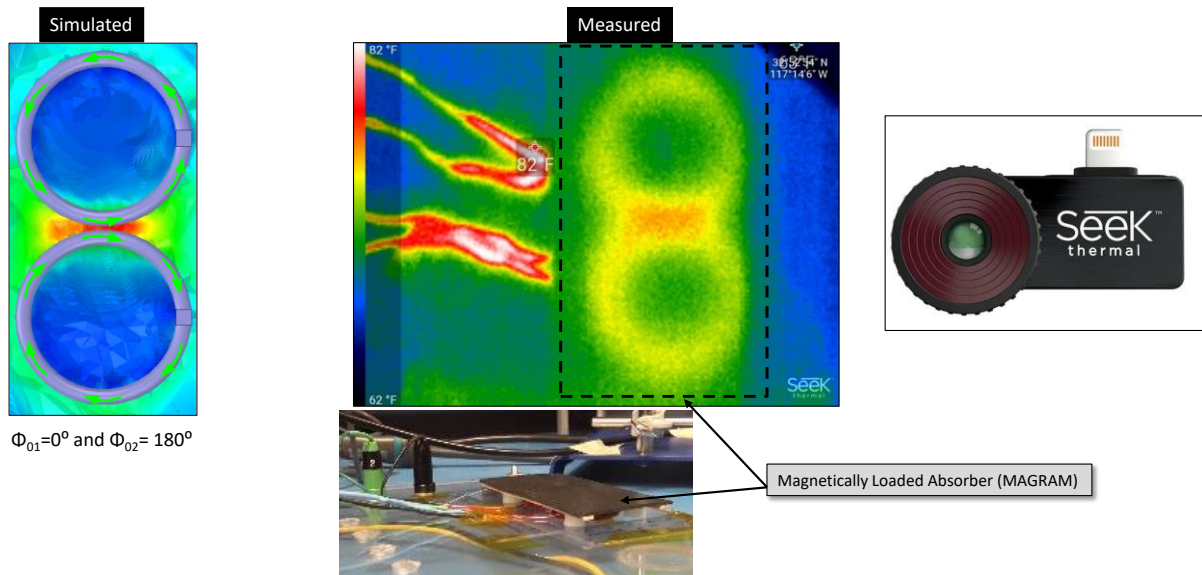


Figure 7.2: Thermal imager measurement ΔT° rise/pattern due to eddy currents.

7.2 B-FIELD MEASUREMENT METHODS

The various methods used to measure the magnitude of the magnetic flux density are summarized in Fig. 7.3. We designed and fabricated several custom probe or search coils to measure the magnitude of the magnetic flux density in air and 1% saline solution (conductivity of 16 mS/cm). Examples include a two custom coils; (a) low-resolution high sensitivity probe (25mm diameter) and (b) high-resolution low sensitivity probe (6.5mm diameter). A precision z-axis translation stage [Edmund Optics] with 1.0 mm steps mounted on a custom stabilization fixture in Fig. 7.3(a) was used for precision decay profile measurements. A Rogowski coil [Fluke, i2000] shown in the Fig. 7.1 photograph, was used to individually measure the time varying current delivered to each coil in the array.

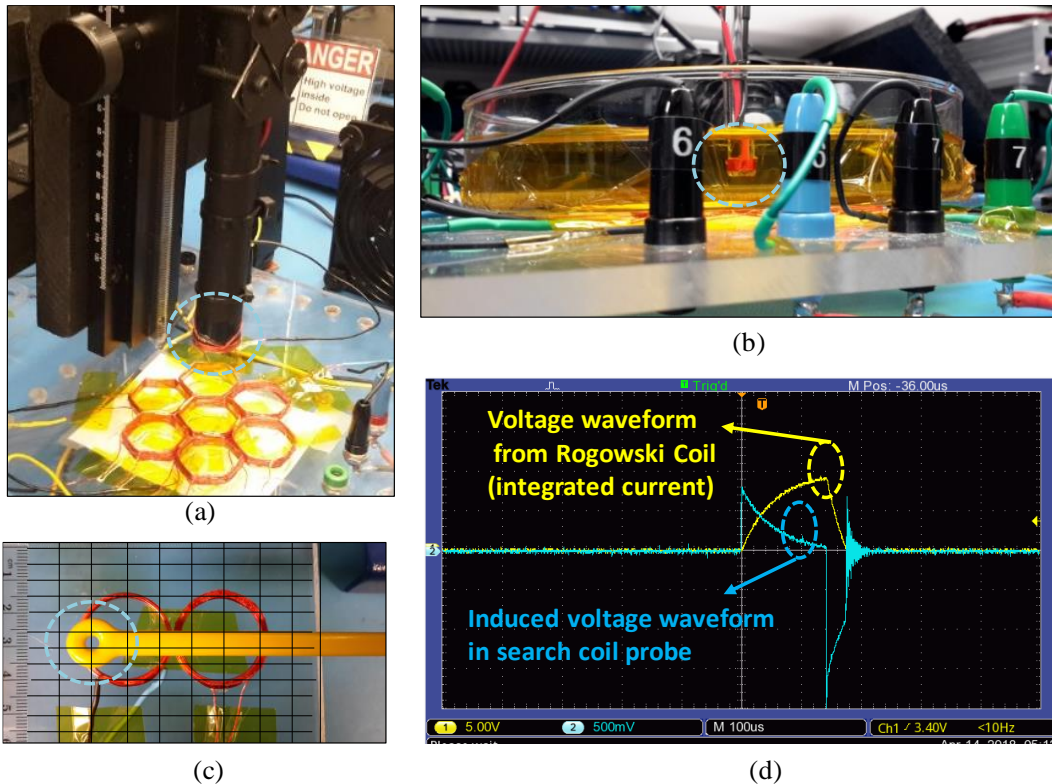


Figure 7.3: (a) Precision z-axis translator with 1.0 mm steps in air, (b) probe coil $|B|$ decay profile measurement with precision z-axis translator with 1.0 mm steps in 1% saline, (c) near field probe [Beehive electronics], and (d) measured monophasic pulsed current waveform using Rogowski coil [Fluke].

As the B-field varies with time, a voltage is induced in the inductive probe via electromagnetic induction. The instantaneous induced voltage is proportional to the time rate of change in magnetic field intensity as seen on the oscilloscope display in Fig 7.3(d). This induced voltage in the search coil shows the magnetic field component parallel to the winding axis of the search coil. Therefore, the B-field measured in the search coil is a good estimation and is expressed as

$$B = \frac{1}{\pi N a^2} \int_0^t V(t) dt \quad (1)$$

$$V = \pi N a^2 \frac{dB}{dt} \quad (2)$$

where B is the magnetic flux density, A is the area of loop, N is the number of turns in the search coil and $V(t)$ is the voltage induced in the search coil [Ueno, 2016].

Our custom near field scanner (Fig. 7.4) was used to image the magnitude of the z-component of the B-field using a search coil held constant in the z-axis positioned 1 to 2 mm above the top of the coil array. A commercial probe [Beehive electronics] was used on the near field scanner shown in Fig. 7.4.

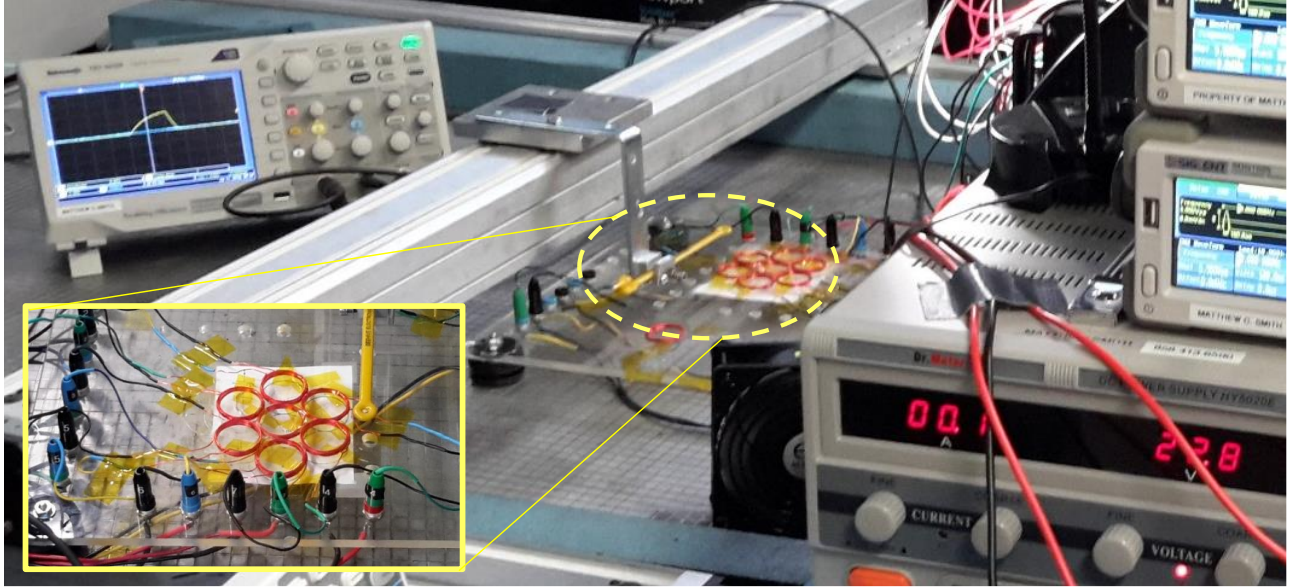


Figure 7.4: Near-field scanner measurement system for B-field imaging (x-y translation stages, z-axis held constant with 1.0 mm steps).

7.3 FINITE ELEMENT MODELING METHODS AND METRICS

The E-field plots are simulated using HFSS21R1 [Ansys HFSSR21, finite element simulation software] and are intended to show the general contours of the patterns qualitatively. However, a simple metric was used to indicate how the induced E-field was modulated at depth in the conductive media by looking at the ratio of $|E_{max}/E_{min}|$ in Fig. 7.5 at depths of 1.0, 4.0 and 6.0mm which yielded metrics of 100, 60 and 50 respectively. This is representative of all the simulated patterns in this paper with the goal of showing that the E-field patterns are present at depth and not only present on the surface of the solution. The exponentially decaying E-fields are relatively weak due to the low current amplitudes of $\pm 10A$ used in this work. The more rapid exponential decay is also indicative of the smaller diameter (30mm) coils used. The fundamental physical constraint is that a 3D focus in depth cannot be achieved (i.e., can't achieve strong E-field

deep in cortex and weak in the structures above) [Heller and Van Hulsteyn, 1992]. Although not the goal of this study the depth of penetration can be increased with larger diameter coils, or the technique reported by the authors [Smith et al, 2021].

The HFSS simulations when analyzed at 350kHz had good agreement with the traditional E-field patterns in the literature [Deng et al, 2013] for figure-8 and circular coils in Fig. 7.1 and Fig. 7.2. Notably HFSS field discrepancies are introduced at low frequencies (e.g., 1Hz to 100kHz in the quasi-static range) but it was also verified experimentally that HFSS21A (Fig. 3.1) was adequate for this proof-of-concept research. The 3-layer array used a spacing of 0.5mm of air between the layers of the coils a 5mm gap between the conductive solution or brain and bottom layer of the array.

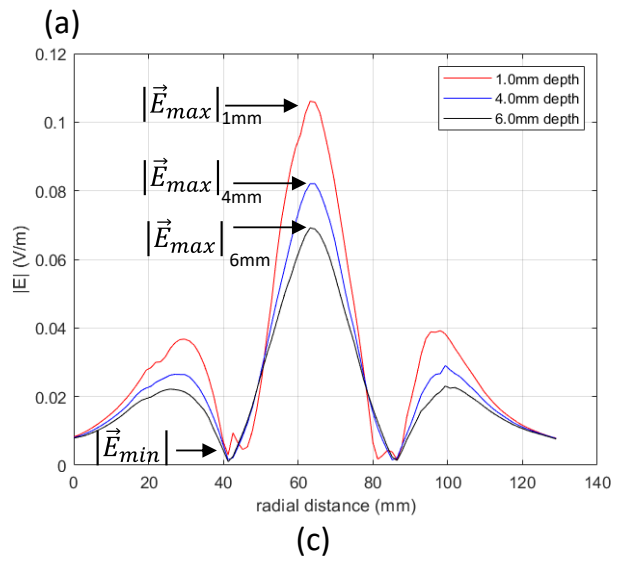
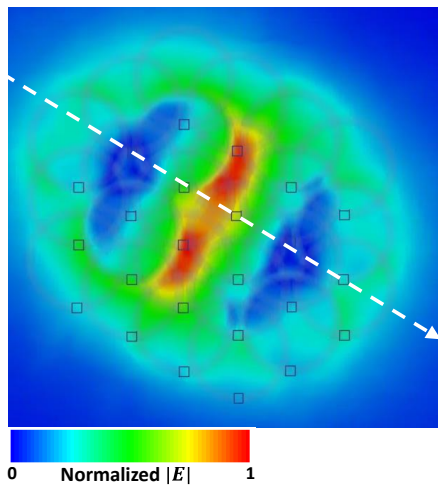
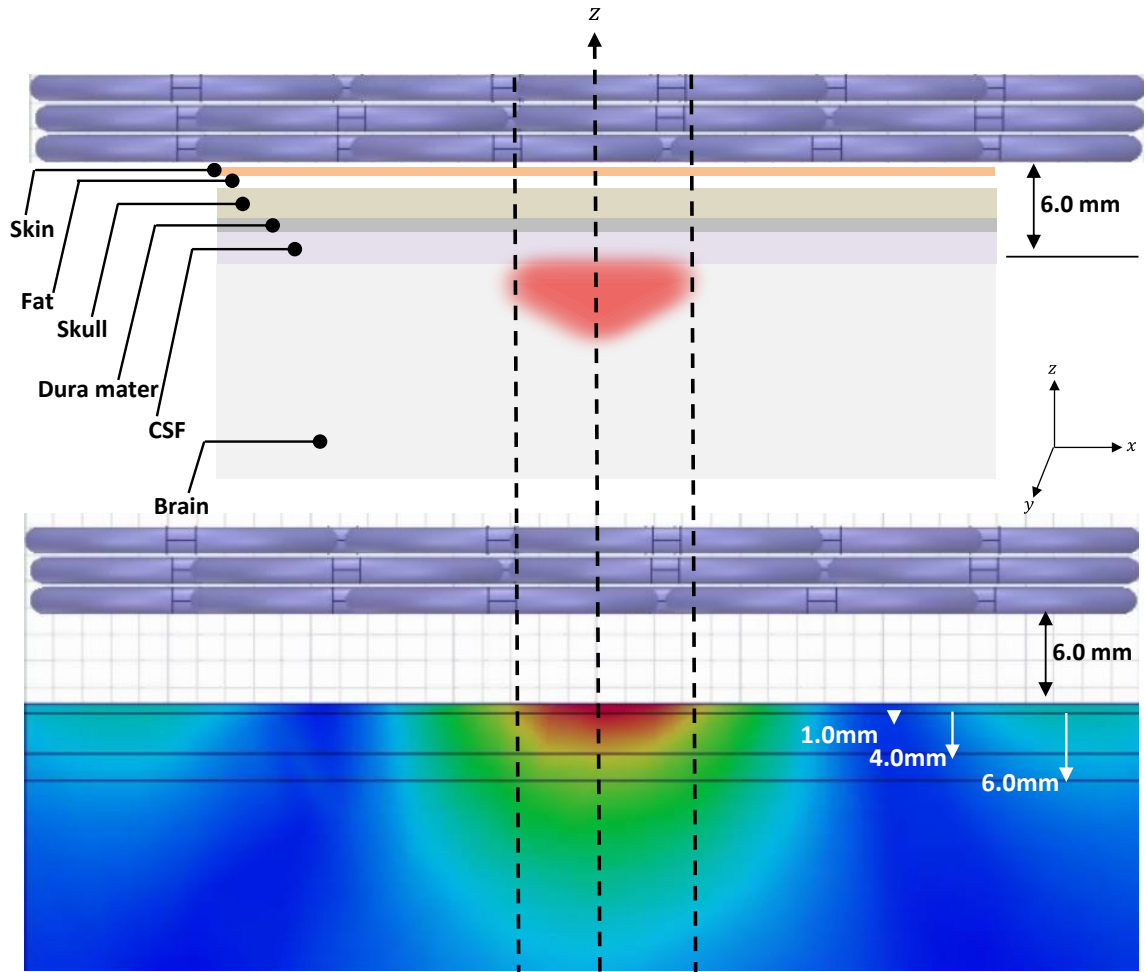


Figure 7.5: Metric for E-field penetration of $|E_{max}/E_{min}|$, (a) z-axis cut in solution at three depths, (b) trajectory of evaluation line (white dashed line), (c) plots of the E-field z-axis cut values for $|E_{max}/E_{min}|$.

This chapter is based on two papers. Sections 7.1 and 7.3 are based on Matthew C. Smith and Daniel F. Sievenpiper, "A New Synthesis Method for Complex Electric Field Patterning using a Multichannel Dense Array System with Applications in Low-Intensity Noninvasive Neuromodulation", *Bioelectromagnetics*, vol. n, no. 2022, pp. (14 pages), *In editorial review*. The dissertation author was the primary investigator and author of this paper. Section 7.2 is based on Matthew C. Smith, Aobo Li and Daniel. F. Sievenpiper, "A Multifunction Dense Array System with Reconfigurable Depth of Penetration," *IEEE Journal of Electromagnetics, RF and Microwaves in Medicine and Biology*, vol. 5, no. 1, pp. 35-45, March 2021. The dissertation author was the primary researcher and author of this paper.

CHAPTER 8 IMPLEMENTATION CHALLENGES

8.1 INTRODUCTION

Despite the many benefits offered by our multichannel 3-layer array system many challenges lay ahead to assess whether it is a tractable implementation for high current applications like high field TMS. Although not the focus of this paper, we identify two key examples of these challenges: coil-to-coil mutual coupling effects and increased power consumption due to the increased number of energized coils. We briefly assess the reduction of mutual coupling effects, by experimentally assessing a technique, proposed by Han [Han et al, 2004]. Reducing power consumption, is not discussed herein however we are investigating several techniques to reduce it: power efficient waveforms [Peterchev et al, 2008; Asbeck et al, 2021], optimized coil current amplitude tapering and advanced thermal management.

8.2 PROXIMITY EFFECTS | MUTUAL COUPLING

As the number of layers are increased in multichannel arrays the proximity effects due to mutual coupling have been shown to distort current waveforms [Han et al, 2004]. This is due to the B-field of a neighboring coil in the array when in a certain spatial orientation in relation another coil in the array. This in turn results in the distortion in the current waveform in the coil. To confirm this waveform distortion and to postulate a mitigation technique we replicated parts of an earlier experiment conducted by a previous group. [Han et al 2004] at the lower current levels used in our study. His current levels were much higher in the 1kA range and assessed only two layers of coils. Although not the focus of this paper, this challenge, regardless of coil diameter, can degrade current waveforms so it is prudent to address and introduce this albeit briefly in this

study. To that end preliminary measurements of the voltage waveforms as affected by coil position were undertaken.

As a baseline, a worst-case condition, and an ideal case (i.e., no coupling) current waveforms were measured to evaluate coil-to-coil mutual coupling in the 12-coil dense array shown in Fig. 8.1. The worst-case waveform degradation occurs when the two coils are vertically aligned center to center along the z-axis as in Fig. 8.1 (blue coils). The ideal, isolated single coil case shown in Fig. 8.1 (red coil). A coil position in the array was selected with a typical overlap condition shown in Fig. 8.1 (green coils) for coils 1 and 5 (highlighted in yellow) in the array. The charging voltages, that gave rise to the currents were initially held constant for these two coils which resulted in a decrease in the voltage waveform in Fig. 8.1 (green waveform). This was then compensated for and brought back to the isolated case voltage level by adjusting the charging voltage by +1.3V in Fig. 8.1 (black). Thus, the mitigation of waveform degradation is feasible by adjusting the voltage on the charging capacitors for each channel as postulated in a previous study [Han et al, 2004].

Based on this simple experiment we propose that this effect could potentially be reduced by our ability to power down, ground non-energized coils and control individual coil current amplitudes by manually adjusting the charging voltages. Future implementations using programmable power supplies, controlled by the system controller, could possibly be implemented to address this issue. These techniques are reasonable but clearly numerous experiments will be required to better understand this design challenge brought on by the highly populated architecture of a three-layer array of coils. Also, extensive measurements on mutual inductance and coupling coefficients must be undertaken as well.

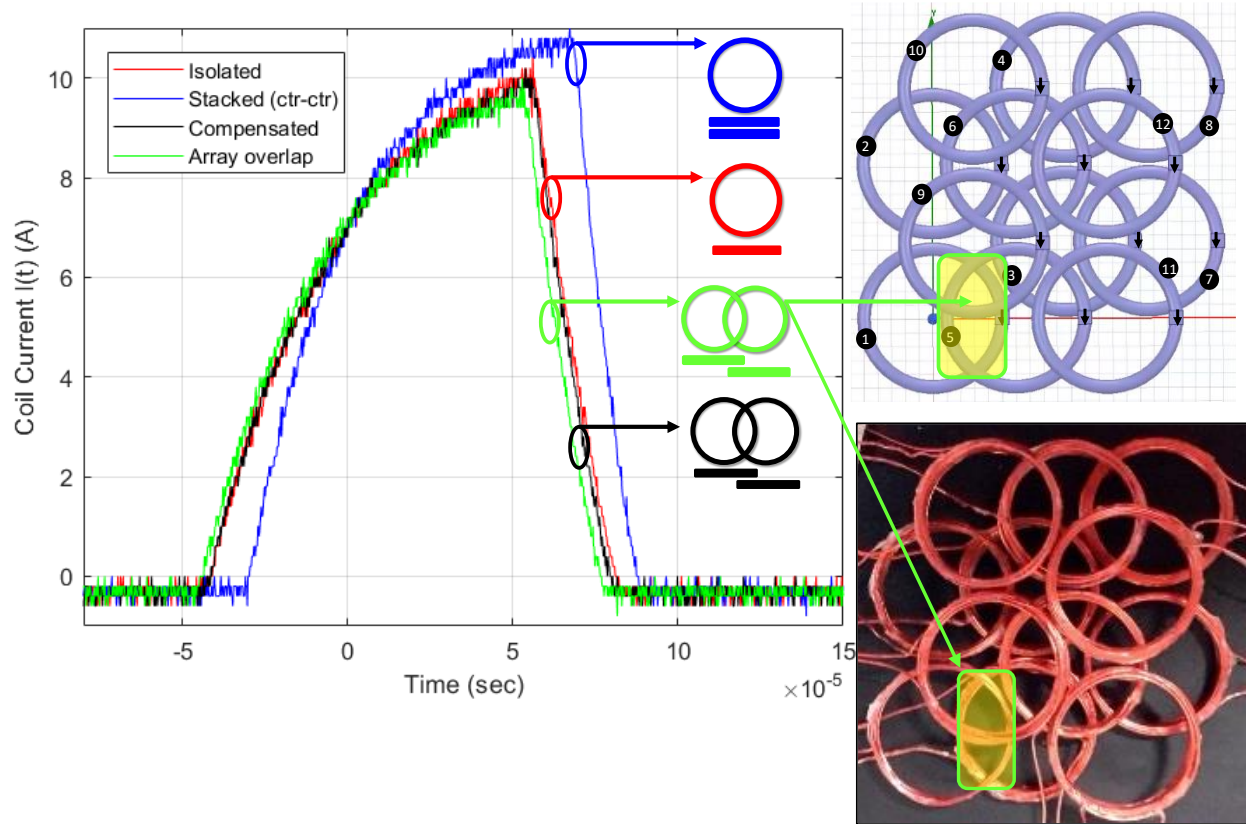


Figure 8.1: Proximity effects due to mutual coupling can be mitigated by the adjustment of charging voltages and coil currents.

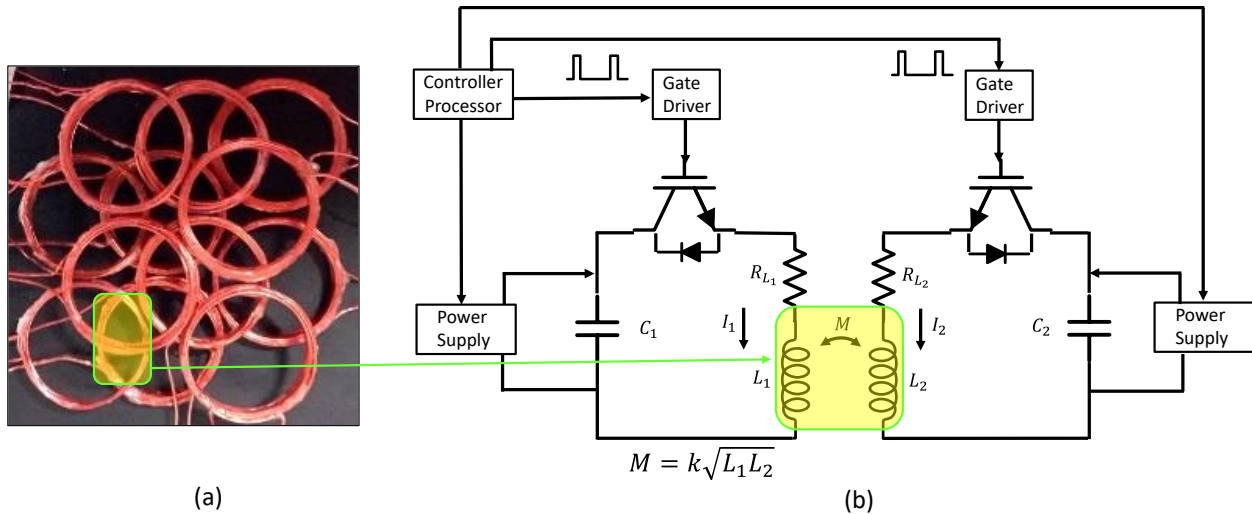


Figure 8.2: Simplified schematic Proximity effects due to mutual coupling can be mitigated by the adjustment of charging voltages and coil currents. (a) photo of 12 coil array and double pixel measured and (b) top level schematic of IGBT and coupling model.

This chapter is based on Matthew C. Smith and Daniel F. Sievenpiper, “A New Synthesis Method for Complex Electric Field Patterning using a Multichannel Dense Array System with Applications in Low-Intensity Noninvasive Neuromodulation”, *Bioelectromagnetics*, vol. n, no. 2022, pp. (14 pages), *In editorial review*. The dissertation author was the primary investigator and author of this paper.

CHAPTER 9 SUMMARY AND CONCLUSION

A unique synthesis method composed of three primary components; a *pixel cell* (basic unit of pattern formation), a *template array* (“virtual array” - code that disseminates the coil current weights to the “physical” dense array), and a hexagonal coordinate system was introduced. Simulations and experimental results verified that highly curved or irregular (e.g., zig - zag) patterns at singular and multiple sites can be efficiently formed using our proposed method. This method was enabled by a multichannel 3-layer array system previously reported by the authors [Smith et al, 2021].

The summary of patterns using our synthesis method pattern, in Fig. 9.1, demonstrates the broad categories of user-defined patterns that can be synthesized using the techniques described in this paper. The multi-locus and multi-site patterns in Fig. 9.1(a) have the potential to assist the researcher in brain connectivity studies which to date have been hampered by slow manual or robotic movement of one or two heavy stimulator coils [Reti, 2015].

Fig. 9.1(b) shows the arbitrary nature of a zig-zag pattern indicating that many different geometrically optimal angles of trajectory of excitation across a sulcus boundary at the appropriate angle are possible [Janssen et al, 2015]. The circular pattern shows that the reconfigurable diameter of a circular pattern, examined in our previous work [Smith et al, 2021], can be increased for increased depth of penetration in cortical tissue or modulated rapidly to alternate depths or sites. Sharp bends of the pattern, Fig. 9.1 (d) can be accommodated to adjust to the complex trajectories across a specific boundary of sulci in the brain unique to each patient. Unilinear patterns with the ability to form at any angle of trajectory are shown in Fig. 9.1 (e) - (f). In all these cases, the induced E-fields and current vectors of the patterns can be rapidly modified, reshaped and redirected with any number of spatiotemporal variations.

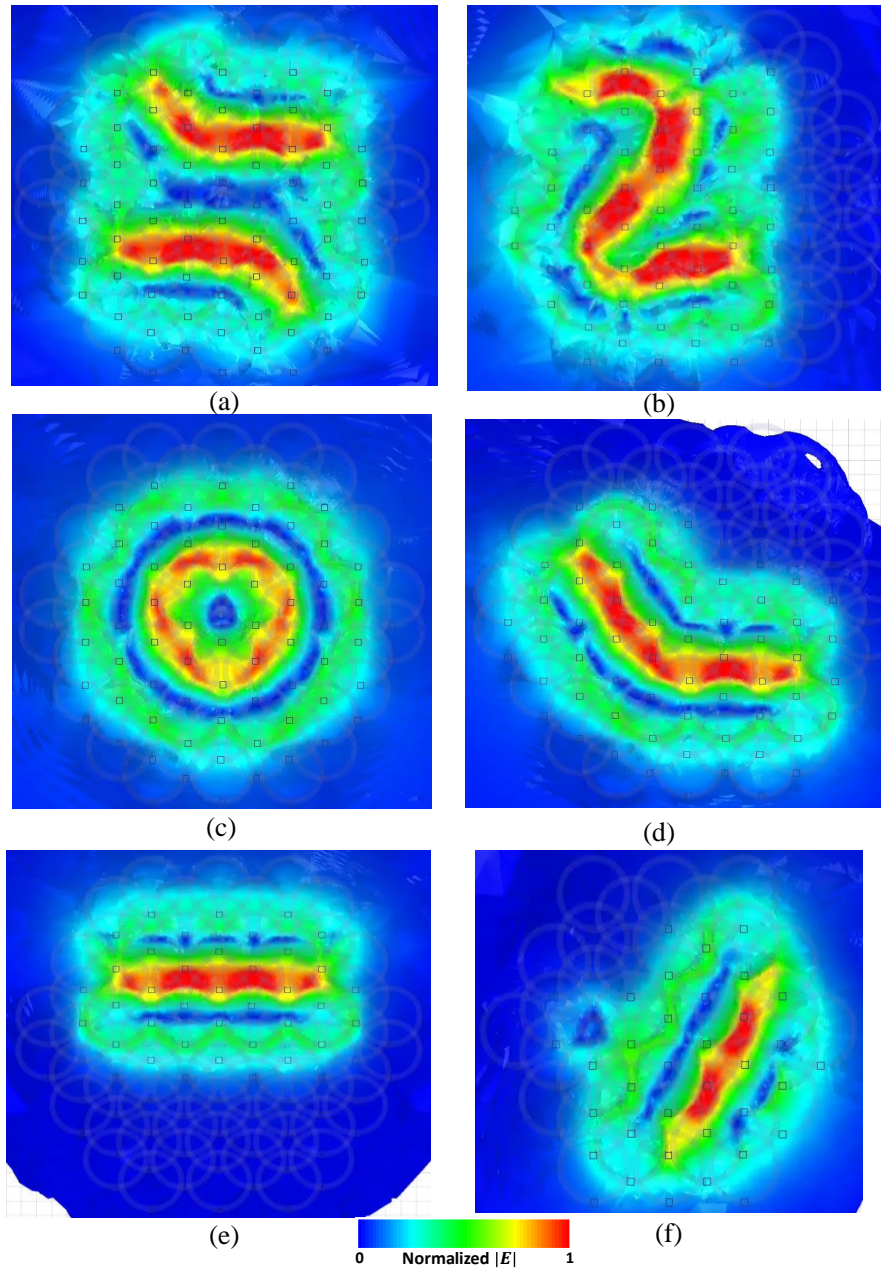


Figure 9.1: Summary of user-defined synthesized patterns. (a) multi-site/multi-loci, (b) zig – zag pattern, (c) circular for reconfigurable depth of penetration, (d) 45° bend, (e) horizontal unilinear and (f) diagonal unilinear.

The primary objective of this work was achieved by demonstrating that many other types of patterns are “possible” and perhaps useful in future biomagnetic applications using our new synthesis method. As an example, the biomagnetic application of low-intensity magnetic

stimulation was suggested as a possible beneficiary of this work in the future. We conclude that the voltage and current levels typically used in LIMS (peak B-fields: μT - mT range, induced E-fields $\leq 1\text{Vm}^{-1}$) are well within the bounds of our implementation approach as demonstrated in this research. However, further experiments will need to be undertaken to completely understand how to mitigate mutual coupling effects. Thermal management at LIMS levels is not deemed an issue with this implementation (array coil $^{\circ}\text{T} < 39^{\circ}\text{C}$ worst case) using forced air on the laboratory bench. However, each application will have to be assessed on a case-by-case basis.

Regarding our proposed approach on reduced extraneous excitation. Ferrites may be a viable candidate when integrated above the array as a shield to further concentrate fields specifically for in LIMS which is typically $< 500\text{mT}$ with the caveat that the selected ferrites concentrate fields but do not saturate. Therefore, it is reasonable to propose that ferrimagnetic, ferromagnetic and ferrites should be considered in LIMS to improve focality or reduced extraneous excitation if deemed beneficial to the neuroscience community and or other applications.

Many of the applications mentioned earlier (Fig. 1.1), as in the case of High-field TMS (peak B-field: $1\text{-}2\text{T}$, induced E-fields $\geq 100\text{Vm}^{-1}$), may benefit as well but only further research will determine that outcome. To summarize, several contributions to the growing research area of low-intensity noninvasive stimulations of this work are,

- A unique method of pattern synthesis
- Synthesized curved and irregular patterns
- Reconfigurable depth of penetration [Smith et al, 2021]
- Multichannel (13-channel) prototype system [Smith et al, 2021]
- A method for reduced extraneous excitation

BIBLIOGRAPHY

- Aldini, *Essai theorique et experimental sur le galvanisme*, 1805.
- Ansys, Inc., HFSS21R1 and Human Body Model V3 (skull/brain), Available: (www.ansys.com/about-ansys).
- Asbeck P, Alluri S, Leung V, Stambaugh M, Abbasi S, Makale M. 2021. A Compact Circuit for Boosting Electric Field Intensity in Repetitive Transcranial Magnetic Stimulation (rTMS). 2021 43rd Annual International Conference of the IEEE Engineering in Medicine & Biology Society (EMBC). 2021:6458-6464.
- Barlow HB, Kohn HL and Walsh EG, Visual sensations aroused by magnetic fields. *Am J Physiol.* 148, 372–375. 1947.
- Barker A, Jalinous R, Freeston I. 1985. Non-invasive magnetic stimulation of human motor cortex. *Lancet.* 325: 1106-1107.
- Bartholow R., Experimental investigations into the functions of the human brain. *Am J Med Sci.* 67, 305–313. 1874.
- Cheng DK. 1993. *Fundamentals of Engineering Electromagnetics*. Upper Saddle River, NJ: Prentice Hall. 186-187.
- d'Arsonval A. Dispositifs pour la mesure des courants alternatifs de toutes fréquences. *C R Soc Biol. (Paris).* 3, 450–457. 1896.
- Deng ZD, Lisanby SD, Peterchev AV. 2013. Electric field depth–focality tradeoff in transcranial magnetic stimulation: simulation comparison of 50 coil designs. *Brain Stimulation.* 6:1-13.
- Dubin MJ, Ilieva IP, Deng ZD, Thomas J, Cochran A, Kravets K, Brody BD, Christos PJ, Kocsis JH, Liston C, Gunning FM. 2019. A double-blind pilot dosing study of low field magnetic stimulation (LFMS) for treatment-resistant depression (TRD). *Journal of affective disorders.* 249:286-293.
- Dufor T, Grehl S, Tang AD, Doulazmi M, Traoré M, Debray N, Dubacq C, Deng ZD, Mariani J, Lohof, AM, Sherrard RM. 2019. Neural circuit repair by low-intensity magnetic stimulation requires cellular magnetoreceptors and specific stimulation patterns. *Science advances,* 5(10):9847
- Esselle K, Stuchly M. 1992. Neural Stimulation with Magnetic Fields: Analysis of Induced Electric Fields. *IEEE Transactions on Biomedical Engineering.* 39(7):693-700.
- Faraday M. 1914. *Experimental Research in Electricity*. London: J. M. Dent.
- Glover PM, Bowtell R. 2007. Measurement of Electric Fields due to Time-varying Magnetic field Gradients using Dipole Probes. *Phys. Med. Biol.* 52:5119-5130.

- Goetz SM, Deng ZD. 2017. The development and modelling of devices and paradigms for transcranial magnetic stimulation. *International Review of Psychiatry*. 29(2):115-145.
- Grehl S, Martina D, Goenvalle C, Deng Z, Rodger J, Sherrard R. 2016. In-Vitro Magnetic Stimulation: A Simple Stimulation Device to Deliver Defined Low Intensity Electromagnetic Fields. [online] *Frontiers in Neural Circuits*, available: www.frontiersin.org/articles/10.3389/fncir.2016.00085/full.
- Gutfleisch O, Willard MA, Brück E, Chen CH, Sankar SG, Liu JP. 2011. Magnetic materials and devices for the 21st century: stronger, lighter, and more energy efficient. *Advanced materials*. 23(7):821-842.
- Hajiaghajani A, Abdolali A. 2018. Magnetic Field Pattern Synthesis and Its Application in Targeted Drug Delivery: Design and Implementation. *Bioelectromagnetics*. 39:325-338.
- Han B, Chun IK, Lee SC, Lee SY. 2004. Multichannel Magnetic Stimulation System Design Considering Mutual Couplings Among the Stimulation Coils. *IEEE Transactions on Biomedical Engineering*. 51(5):812-817.
- Harris CR, Millman KJ, Van Der Walt SJ, et al. 2020. Array programming with NumPy. *Nature*. 585:357–362.
- Hart FX, Wood KW. 1991. Eddy Current Distributions: Their Calculations with a spreadsheet and their measurements with a dual dipole antenna probe. *Am. J. Physics*. 59(5):461-467.
- Heller L, Van Hulsteyn DB. 1992. Brain stimulation using electromagnetic sources: theoretical aspects. *Biophysical Journal*. 63:129-138.
- Hernandez-Garcia L, Hall T, Gomez L, Michielssen E. 2010. A numerically optimized active shield for improved transcranial magnetic stimulation targeting. *Brain stimulation*, 3(4): 218-225.
- Ho GX, Fu WN, Yang Q, Hou H, Yan W. 2009. Optimization of Array Magnetic Coil Design for Functional Magnetic Stimulation Based on Improved Genetic Algorithm. *IEEE Transactions on Magnetics*. 45(10):4849-52.
- Ianniello C, Zwart JAD, Duan Q, Deniz CM, Alon L, Lee JS, Lattanzi R, Brown R. 2018. Synthesized Tissue-Equivalent Dielectric Phantoms Using Salt and Polyvinylpyrrolidone Solutions. *Magnetic Resonance in Medicine*. 80:413-419.
- Janssen AM, Oostendorp TF, Stegeman DF. 2015. The coil orientation dependency of the electric field induced by TMS for M1 and other brain areas. *J NeuroEngineering Rehabil*. 12:47.
- Kellaway P. 1946. The part played by electric fish in the early history of bioelectricity and electrotherapy. *Bulletin of the History of Medicine*. 20(2):112-137.
- Koponen LM, Nieminen JO, Ilmoniemi RJ. 2018. Multi-locus transcranial magnetic stimulation – theory and implementation. *Brain Stimulation*. 11(4):849-855.

- Ma L, Soleimani M. 2017. Magnetic induction tomography methods and applications: a review. *Measurement Science and Technology*. 28.
- Minusa S, Muramatsu S, Osanai H, Tateno T. 2019. A multichannel magnetic stimulation system using submillimeter-sized coils: system development and experimental application to rodent brain in vivo. *Journal of neural engineering*. 16(6):066014.
- Modi A., Singh R, Chavan V, Kukreja K, Ghode S, Manwar K, Kazi F. 2016. Hexagonal Coil Systems for Uniform Magnetic Field Generation, *IEEE Asia-Pacific Conference on Applied Electromagnetics*. 47-51.
- Mouchawar GA, Nyenhuis JA, Bourland JD, Geddes LA. 1991. Guidelines for energy efficient coils: designed for magnetic stimulation of the heart. *Electroencephalography and Clinical Neurophysiology*. 43: 255–267.
- Navarro de Lara LI, Daneshzand M, Mascarenas A, Paulson D, Pratt K, Okada Y, Raij T, Makarov SN, Nummenmaa A. 2021. A 3-axis coil design for Multichannel TMS arrays. *NeuroImage*. 224.
- Nieminen J, Sinisalo H, Souza V, Malmi M, Uryyev M, Tervo A, Stenroos M, Milardovich DN, Korhonen J, Koponen L, Ilmoniemi RJ. 2022. Multi-locus transcranial stimulation system for electronically targeted brain stimulation. *Brain Stimulation*. 15(1):116-124.
- Optiz A, Windhoff M, Heidemann RM, Turner R, Thielscher A. 2011. How the brain shapes the electric field induced by transcranial magnetic stimulation. *NeuroImage*. 58:849-859.
- Peterchev AV, Jalinous R, Lisanby SH. 2008. A Transcranial Magnetic Stimulator Inducing Near-Rectangular Pulses with Controllable Pulse Width (cTMS). *IEEE Transactions on Biomedical Engineering*. 55(1): 257-266.
- Polson, MJR, Barker AT, Gardiner S. 1982. The effect of rapid rise-time magnetic fields on the ECG of the rat. *Clinical Physics and Physiological Measurement*, 3(3), p.231.
- Reti IM (Editor). 2015. *Brain Stimulation Methodologies and Interventions*. Irving M. Reti Editor. Hoboken, New Jersey: John Wiley & Sons, Inc.
- Rohan ML, Yamamoto RT, Ravichandran CT, Cayetano KR, Morales OG, Olson DP, Vitaliano, G, Paul SM, Cohen BM. 2014. Rapid Mood-Elevating Effects of Low Field Magnetic Stimulation in Depression. *Biological Psychiatry*. 76(3):186-193.
- Ryu SB, Paulk AC, Yang JC, Ganji M, Dayeh SA, Cash SS, Fried SI, Lee SW. 2020. Spatially confined responses of mouse visual cortex to intracortical magnetic stimulation from micro-coils. *Journal of Neural Engineering*. 17(5):056036.
- Salinas FS, et al. 2007. Detailed 3D Models of the induced electric field of transcranial stimulation coils. *Physics in Medicine and Biology*. 52:2879-2892.

- Selvaraj J, Rastogi P, Gaunker NP, Handimani RL, Mina M. 2018. Transcranial Magnetic Stimulation: Design of a Stimulator and a Focused Coil for the Application of Small Animals. *IEEE Transactions on Magnetics*. 54(11): 215–219.
- Smith MC, Li A, Sievenpiper DF. 2021. A Multifunction Dense Array System with Reconfigurable Depth of Penetration. *IEEE Journal of Electromagnetics, RF and Microwaves in Medicine and Biology*. 5(1) 35-45.
- Tang AD, Lowe AS, Garrett AR, Woodward R, Bennett W, Canty AJ, Garry MI, Hinder MR, Summers JJ, Gersner R, Rotenberg A. 2016. Construction and evaluation of rodent-specific rTMS coils. *Frontiers in neural circuits*. 10:47.
- Tang, A.D., Bennett, W., Hadrill, C., Collins, J., Fulopova, B., Wills, K., Bindoff, A., Puri, R., Garry, M.I., Hinder, M.R. and Summers, J.J., 2018. Low intensity repetitive transcranial magnetic stimulation modulates skilled motor learning in adult mice. *Scientific reports*, 8(1):1-9.
- Thielscher A, Optiz A Windoff M. 2011. Impact of the gyral geometry on the electric field induced by transcranial magnetic stimulations. *NeuroImage*. 54:234-243.
- Ueno S, Tashiro T, Harada K. 1988. Localized stimulation of neural tissues in the brain by means of a paired configuration of time-varying magnetic fields. *Journal of Appl. Phys.* 64:5862-5864.
- Vojtěch U, Gajdoš P, Jeżowicz T, Snášel V. 2016. Application of hexagonal coordinate systems for searching the K-NN in 2D space. *Innovations in Bio-Inspired Computing and Applications*. Springer, Cham. 209-220.
- Volta A. 2016. On the Electricity Excited by the Mere Contact of Conducting Substances of Different Kinds. *Philosophical Transactions of the Royal Society of London (in French)*. 90: 403–431.
- Wagner T, Rushmore J, Eden U, Valero-Cabre A. 2009. Biophysical foundations underlying TMS: setting the stage for an effective use of neurostimulation in the cognitive neurosciences. *Cortex*. 45(9):1025-1034.
- Wang B, Shen MR, Deng Z, Smith JE, Tharayil JJ, Gurrey CJ, Gomez LJ, Peterchev AV. 2018. Redesigning existing transcranial stimulation coils to reduce energy: application to low field magnetic stimulation. *Journal Neural Engineering*. 15.
- Wasserman EM, Epstein CM, Ziemann U, Walsh V, Paus T, Lisanby SH. 2008. *The Oxford Handbook of Transcranial Stimulation*. Oxford University Press New York, New York.
- Wei, YL, Lu M, Wang J, Yi G. 2017. Comprehensive Survey on Improved Focality and Penetration Depth of Transcranial Magnetic Stimulation Employing Multi-Coil Arrays. [online]. Available: <https://doi.org/10.3390/ijerph14111388>.

Weisstein EW. Reuleaux Triangle. MathWorld-A Wolfram Web Resource,
[www./mathworld.wolfram.com/ReuleauxTriangle.html](http://www.mathworld.wolfram.com/ReuleauxTriangle.html).

Yang G X, Wang YG, Yu H, Yang Q. 2010. Circular Coil Array Model for Transcranial Magnetic Stimulation. IEEE Transactions on Applied Superconductivity. 20(3):829-833.

Zangen A, Roth Y, Voller B, Hallet M. 2005. Transcranial magnetic stimulation of deep brain regions: evidence for efficacy of the H-Coil. Clinical Neurophysiology. 116(4):775-779.

Zmeykina E, Mittner M, Paulus W, Turi Z. 2020. Weak rTMS-induced electric fields produce neural entrainment in humans. Scientific Reports. 10:11994.